

# FINAL REPORT

Handheld UXO Sensor  
Improvements to Facilitate  
UXO/Clutter Discrimination  
Volume 1

SERDP Project MM-1381

NOVEMBER 2007

Dr. Thomas Bell  
SAIC

Dr. Leslie Collins  
Duke University



Strategic Environmental Research and  
Development Program

Report Documentation Page				Form Approved OMB No. 0704-0188		
Public reporting burden for the collection of information is estimated to average 1 hour per response, including the time for reviewing instructions, searching existing data sources, gathering and maintaining the data needed, and completing and reviewing the collection of information. Send comments regarding this burden estimate or any other aspect of this collection of information, including suggestions for reducing this burden, to Washington Headquarters Services, Directorate for Information Operations and Reports, 1215 Jefferson Davis Highway, Suite 1204, Arlington VA 22202-4302. Respondents should be aware that notwithstanding any other provision of law, no person shall be subject to a penalty for failing to comply with a collection of information if it does not display a currently valid OMB control number.						
1. REPORT DATE <b>01 NOV 2007</b>		2. REPORT TYPE <b>N/A</b>		3. DATES COVERED <b>-</b>		
4. TITLE AND SUBTITLE <b>Handheld UXO Sensor Improvements to Facilitate UXO/Clutter Discrimination Volume 1</b>				5a. CONTRACT NUMBER		
				5b. GRANT NUMBER		
				5c. PROGRAM ELEMENT NUMBER		
6. AUTHOR(S)				5d. PROJECT NUMBER		
				5e. TASK NUMBER		
				5f. WORK UNIT NUMBER		
7. PERFORMING ORGANIZATION NAME(S) AND ADDRESS(ES) <b>SAIC</b>				8. PERFORMING ORGANIZATION REPORT NUMBER		
9. SPONSORING/MONITORING AGENCY NAME(S) AND ADDRESS(ES)				10. SPONSOR/MONITOR'S ACRONYM(S)		
				11. SPONSOR/MONITOR'S REPORT NUMBER(S)		
12. DISTRIBUTION/AVAILABILITY STATEMENT <b>Approved for public release, distribution unlimited</b>						
13. SUPPLEMENTARY NOTES <b>The original document contains color images.</b>						
14. ABSTRACT						
15. SUBJECT TERMS						
16. SECURITY CLASSIFICATION OF:				17. LIMITATION OF ABSTRACT <b>UU</b>	18. NUMBER OF PAGES <b>118</b>	19a. NAME OF RESPONSIBLE PERSON
a. REPORT <b>unclassified</b>	b. ABSTRACT <b>unclassified</b>	c. THIS PAGE <b>unclassified</b>				

This report was prepared under contract to the Department of Defense Strategic Environmental Research and Development Program (SERDP). The publication of this report does not indicate endorsement by the Department of Defense, nor should the contents be construed as reflecting the official policy or position of the Department of Defense. Reference herein to any specific commercial product, process, or service by trade name, trademark, manufacturer, or otherwise, does not necessarily constitute or imply its endorsement, recommendation, or favoring by the Department of Defense.

## Table of Contents

<b>1. Introduction</b>	<b>1</b>
1.1. Background	1
1.2. Objective	2
1.3. Technical Approach	2
<b>2. Controlled Two-Dimensional Motions</b>	<b>5</b>
2.1. Measurement Setup	5
2.1.1. Apparatus Description	5
2.1.2. Performed Scenarios	8
2.2. Definitions and Notation	10
<b>3. Data Analysis and Signal Processing</b>	<b>13</b>
3.1. Inertial Measurement Unit	13
3.1.1. Attitude Determination	13
3.1.2. Velocity and Position Determination	19
3.1.2.1. Pure Rotational Motion	20
3.1.2.2. Uncoupled Rotational and Linear Motion	25
3.1.2.3. Coupled Rotational and Linear Motion	37
3.2. Electromagnetic Induction Sensor	45
3.2.1. Inversion Results	45
<b>4. EM61-HH Dynamic Response</b>	<b>48</b>
4.1. Dynamic Response Characteristics	48
4.2. EM61-HH Two-Dimensional Sweep Data	50
4.3. Inversion Results	52
<b>5. Arcsecond Laser-Based Positioning</b>	<b>54</b>
5.1. Test Setup	54
5.2. Test Results	56
<b>6. Three Dimensional Motion</b>	<b>63</b>
6.1. Zero Velocity Update Method	63
6.2. Test Setup	66
6.3. Processing and analysis	66
6.3.1. Determination of the Angular Rate Bias Vector	67
6.3.2. Determination of the Acceleration Bias Vector	69
6.3.3. Determination of the Orientation Angles	72
6.3.4. Integration of the Fully Compensated Acceleration Vector	78
<b>7. SAINT Tests</b>	<b>90</b>
7.1. The SAINT system	90
7.2. Test Setup	91
7.3. Trajectory Comparisons	93
7.4. Inversion Results	98
<b>8. Adaptive Processing – Joint Target/Track Estimation</b>	<b>103</b>
<b>9. Conclusions</b>	<b>106</b>
<b>10. References</b>	<b>107</b>
<b>Appendix A: The Yaw-Pitch-Roll Rotation Sequence</b>	<b>108</b>

## Figures

Figure 1: Collecting EM61-HH data on a grid over a suspected buried UXO item.....	1
Figure 2: Two views of the body consisting of a Crossbow IMU400 (with its sensitive axes expanded on the left) and a Geonics EM61-HH.....	5
Figure 3: The apparatus as viewed from an overhead video camera. The point of attachment also served as a pivot point. ....	6
Figure 4: Stickers placed on the EM61-HH sensor head for ground truth positioning purposes. ....	7
Figure 5: Data Set A - Back & Forth Linear Trajectory over a 2" Al sphere. ....	8
Figure 6: Data Set B - Back & Forth Arced Trajectory over a 2" Al sphere.....	8
Figure 7: Data Sets C1 & C2 - Two Back & Forth Sweep and Push Trajectories over a 2" Al sphere. ....	9
Figure 8: Data Set D - Back & Forth Swing Trajectory over a 2" Al sphere. ....	9
Figure 9: Data Set E - Back & Forth Swing Trajectory over a 40mm Projectile.....	10
Figure 10: Schematic diagram showing the relevant vectors and coordinate frames.....	11
Figure 12: Angles determined via the IMU angular rates for Data Set C2. The over-plotted red curve represents the yaw angle determined from the video data. ....	16
Figure 13: The computed yaw angles for other IMU data sets. The over-plotted red curves represent the yaw angle determined from the video data. ....	18
Figure 14: IMU x-component accelerometer values for Data Set B. The red curve in the top panel represents the x-component of the right hand side of equation (12), as computed via the IMU angular rates. The colored curves in the bottom panel show the respective contributions to the x-component of the acceleration. ....	22
Figure 15: IMU y-component accelerometer values for Data Set B. The red curve in the top panel represents the y-component of the right hand side of equation (12), as computed via the IMU angular rates. The colored curves in the bottom panel show the respective contributions to the y-component of the acceleration. ....	23
Figure 16: IMU z-component accelerometer values for Data Set B. The red curve in the top panel represents the z-component of the right hand side of equation (12), as computed via the IMU angular rates. The colored curves in the bottom panel show the respective contributions to the z-component of the acceleration.....	24
Figure 17: The accelerometer-derived (black) vs. the gyroscope-derived (green) velocity components for the IMU in the initial body frame for Data Set B.....	26
Figure 18: The accelerometer-derived (black) vs. the gyroscope-derived (green) IMU positions in the initial body frame for Data Set B.....	27
Figure 19: The gyroscope-derived vs. video ground truth (red) positions for sticker 4 in the video frame. ....	28
Figure 20: The mismatches between the gyroscope-derived and the video ground truth X and Y positions of Figure 19. ....	29
Figure 21: Acceleration components as measured via the IMU for Data Set C2. The over-plotted red curves represent the linear contribution based on equation (12). ....	30
Figure 22: Acceleration components as measured via the IMU for Data Set C2. The over-plotted colored curves show the respective contributions to the acceleration components. ....	31
Figure 23: The accelerometer-derived (black) vs. the gyroscope-derived (red) velocity components for the IMU in the initial body frame for Data Set C2. The gyroscope-	

derived velocity components neglect the linear contributions to velocity, as a matter of definition, but remain much more stable.....	32
Figure 24: The rms fit errors for polynomial fits of given order to the mismatch between accelerometer-derived and the gyroscope-derived velocity components for the IMU in the initial body frame for Data Set C2.....	33
Figure 25: The polynomial-corrected accelerometer-derived (green) vs. the gyroscope-derived (red) velocity components for the IMU in the initial body frame for Data Set C2. The polynomials chosen for the corrections are quadratics for all three components (choice based on Figure 24) .....	34
Figure 26: The video frame positions obtained by integrating the uncompensated accelerometer-derived velocity components (black) vs. those obtained by integrating the quadratic-corrected accelerometer-derived velocity components (green). The red curves represent the ground truth positions extracted from the video data for Data Set C2.....	35
Figure 27: The mismatches between the compensated accelerometer-derived and the video ground truth X and Y positions of Figure 26. ....	36
Figure 28: The trajectory of sticker 4 based on the ground truth positions extracted from the video data (red) vs. the trajectory obtained by integrating the quadratic-corrected accelerometer-derived velocity components (green) for Data Set C2.....	37
Figure 29: Acceleration components as measured via the IMU for Data Set E. The over-plotted red curves represent the linear contribution based on equation (12). Note that the linear contribution is not decoupled from the rotational contribution (cf. with Figure 30).....	38
Figure 30: Acceleration components as measured via the IMU for Data Set E. The over-plotted colored curves show the respective contributions to the acceleration components. ....	39
Figure 31: The accelerometer-derived (black) vs. the gyroscope-derived (red) velocity components for the IMU in the initial body frame for Data Set E. The gyroscope-derived velocity components neglect the linear contributions to velocity, as a matter of definition, but remain much more stable.....	40
Figure 32: The quadratic-corrected accelerometer-derived (green) vs. the gyroscope-derived (red) velocity components for the IMU in the initial body frame for Data Set E. Note that only the IMU data in the time interval of Data Set E (i.e. 0 – 17 s) was chosen for the correction process. ....	42
Figure 33: The video frame positions obtained by integrating the uncompensated accelerometer-derived velocity components (black) vs. those obtained by integrating the quadratic-corrected accelerometer-derived velocity components (green). The red curves represent the ground truth positions extracted from the video data for Data Set E.....	43
Figure 34: The trajectory of sticker 4 based on the ground truth positions extracted from the video data (red) vs. the trajectory obtained by fully compensating as described in the text (green) for Data Set E. ....	44
Figure 35: The mismatches between the red and green X and Y positions of Figure 34. ....	44
Figure 36: Contours of the EM61-HH data (blue curves) vs. those of the model based on the inversion target parameter results (red curves) for Data Set E with the compensated IMU-derived positions (black dots) employed. The grey dots represent the ground truth positions extracted from the video data (for reference). ....	46

Figure 37: The measured EM61-HH response to a sequence of five second on / five second off pulses. ....	49
Figure 38: The normalized EM61-HH response to a five second on / five second off signal. Data from all the pulses in Figure 20 are used. The green curve represents the best fit to the data using (13) with coefficients $\omega_n = 6.2$ and $\zeta = 0.78$ .....	49
Figure 39: New overall setup for 2D motion measurements.....	50
Figure 40:- Close up of rigid flat board .....	51
Figure 41: Automatic extraction of positioning ground truth from video frame data via intensity threshold using LEDs.....	52
Figure 42: Comparison of static and dynamic response models with measured response..	52
Figure 43: Inversion results showing $\beta$ s when the dynamic response is not taken into account (upper panel) versus when it is taken into account (lower panel).....	53
Figure 44: 2D and 3D EM61-HH sensor positioning experiments. In (a) sideview and (b) video camera view, the 2D sensor board is shown with EM61 coil, LEDs, Arcsecond sensors and Crossbow IMU. In (c) the 3D setup is shown with standard EM61-HH pole, Arcsecond sensors and IMU. ....	55
Figure 45: Sample X-Y and X-Z plots of the EM61-HH coil trajectories. In (a) and (c), the 2D coil motion on the sensor board as measured by the Arcsecond (black symbols) and the video (red curve). In (b) and (d), the 3D motion of the coil on the standard EM61-HH pole. The green symbol is the object location.....	57
Figure 46: Time rasters of EM61-HH data (black curve and symbols) fitted to model (green curve).....	58
Figure 47: Plots along X of EM61-HH data (black curve and symbols) fitted to model (green curve).....	59
Figure 48: Results of fitting EM61-HH data with model using different positioning data.	60
Figure 49: Monte Carlo simulation of inverting 40mm projectile data with randomly generated position errors. Dashed line at RMS position error of 3 mm with an average fit coherence of 0.998 and a primary b spread of 15% (0.05/0.34).....	62
Figure 50: Setup for 3D motion of just the IMU.....	67
Figure 51: The angular rate bias vector components plotted [in red] with the mean and standard deviation for each of the zero velocity updates. ....	69
Figure 52: The pitch and roll angles determined via (19), for the case of the IMU sitting still on a table top for 50 minutes. Compensated angular rates have been used and initial angles of zero assumed.....	73
Figure 53: The pitch and roll angles determined via (31) and (32), respectively, using the de-biased accelerations over assumed 5 second zero velocity updates [in red], and via (19) using the compensated angular rates during assumed 3 second segments of unknown motion between updates [in black], for the case of the IMU sitting still on a table top for 50 minutes. The bottom two panels are close ups of the first 200 seconds. ....	75
Figure 54: The pitch and roll angles of Figure 53, but with linear trends subtracted from the assumed segments of unknown motion between updates. Any discontinuities that existed between the angles at the end of these segments and those at the subsequent zero velocity updates have been removed. As before, the bottom two panels are close ups of the first 200 seconds.....	76
Figure 55: The pitch and roll angles determined via (19), for the case of back and forth 3D sweeping motion of the IMU between two well-defined fixed points [represented by the	

red and green data]. Compensated angular rates have been used and initial angles of zero assumed.....	77
Figure 56: The pitch and roll angles determined via (31) and (32), respectively, using the de-biased accelerations during the zero velocity updates [in red and green], and via (19) using the compensated angular rates between updates [in black], for the case of back and forth 3D sweeping motion of the IMU between two well-defined fixed zero velocity update points. ....	77
Figure 57: The pitch and roll angles of Figure 56, but with linear trends subtracted between zero velocity updates so as to remove any existing discontinuities.....	78
Figure 58: The yaw angle determined via (19) using the compensated angular rates and the compensated pitch and roll angles of Figure 57. The yaw angles during the initial and final zero velocity updates were assumed to be $-45^\circ$ . The bottom panel shows the compensated yaw angle, where a linear trend has been subtracted between the end of the initial, and the beginning of the final, zero velocity updates. ....	78
Figure 59: The mean and standard deviation of the compensated acceleration components over each of the assumed zero velocity updates, for the case of the IMU sitting still on a table top for 50 minutes. Due to the proximity and sheer quantity of updates, the diamonds representing the means appear to merge into continuous thick dark curves, while the error bars produce the lighter fabric that envelope the mean curves. The red curves represent residual linear trends. ....	80
Figure 60: The velocity components obtained by integrating the corresponding fully compensated acceleration components between the assumed zero velocity updates, for the case of the IMU sitting still on a table top for 50 minutes. By definition, the velocity is zero during the zero velocity updates. The fully compensated acceleration components used here have had the residual trends, shown in Figure 59, subtracted from each component, and have also been transformed from the IMU body frame to the Earth frame. ....	81
Figure 61: The velocity components of Figure 55, but with linear trends subtracted between zero velocity updates so as to remove any existing discontinuities.....	82
Figure 62: The estimated position components in the Earth frame obtained by integrating the corresponding compensated velocity components of Figure 61. The black curves represent direct integrations, with initial positions of zero being the only assumptions made; the green curves are the result of forcing the final positions to be zero as well, with linear corrections applied between both ends; and the red curves are the result of forcing every 25 <sup>th</sup> update (200 seconds) to be zero, with linear corrections applied between each of these.....	83
Figure 63: The estimated X and Y positions of Figure 62 plotted against one another, showing the deviations from the true (0,0) position. The blue circle shown has a radius of 2 cm about the true position. The same color coding used in Figure 62 is retained here. ....	84
Figure 64: The mean and standard deviation of the compensated acceleration components over the zero velocity updates, for the case of back and forth 3D sweeping motion of the IMU between two well-defined fixed points. The zero velocity updates take place at the two fixed points .....	85
Figure 65: The velocity components obtained by integrating the corresponding fully compensated acceleration components between the zero velocity updates, for the case of back and forth 3D sweeping motion of the IMU between two well-defined fixed	



points. By definition, the velocity is zero during the zero velocity updates. The fully compensated acceleration components used here have had the residual trends, shown in Figure 64, subtracted from each component, and have also been transformed from the IMU body frame to the Earth frame. ....	86
Figure 66: The velocity components of Figure 65, but with linear trends subtracted between zero velocity updates so as to remove any existing discontinuities.....	87
Figure 67: The estimated position components in the Earth frame obtained by integrating the corresponding compensated velocity components of Figure 61. The black curves represent direct integrations, with initial positions of zero being the only assumptions made; the green curves are the result of forcing the final positions to be zero as well, with linear corrections applied between both ends; and the red curves are the result of forcing every other update position to be zero, with linear corrections applied between each of these.....	88
Figure 68: The estimated X and Y positions of Figure 67 plotted against one another, showing the deviations from the two fixed points (blue circles) about which the sweeping takes place. The blue circles shown have radii of 2 cm. The same color coding used in Figure 67 is retained here. ....	89
Figure 69: SAINT System combining EM61-HH and Honeywell HG1900 IMU. ....	90
Figure 70: Simultaneous angle rate data from Crossbow and Honeywell IMUs.....	91
Figure 71: EM61-HH coil head trajectory over A3 cell in ArcSecond coordinate system. IMU-derived trajectory is plotted in black and ArcSecond trajectory in red. ....	93
Figure 72: Different cell trajectories about zero point and relative to APG local grid. Joint ArcSecond/IMU data in red and IMU only data in black.....	94
Figure 73: Different cell trajectories from IMU only data at other Arcsecond measured zero points. Local grid coordinates. ....	95
Figure 74: Comparison of IMU (black) and ArcSecond (red) trajectories. ArcSecond coordinates.....	96
Figure 75: Second comparison of IMU (black) and ArcSecond (red) trajectories. ArcSecond coordinates. ....	97
Figure 76: Fit error comparison between EM data with IMU and ArcSecond positioning. ....	99
Figure 77: Comparison of fitted $\beta$ polarization parameters on 20 mm cells.....	101
Figure 78: $\beta$ fits of 40mm grenade data compared to 20 mm fits. ....	102
Figure 79: Plots of fit error versus EM61-HH signal-to-noise ratio. Curves indicate limits based on 0, 1, and 2 centimeter positioning errors. ....	102
Figure 80: Approach to true trajectory using downhill simplex procedure. Inset shows initial distorted trajectory in red and true trajectory in black. ....	104
Figure 82: Fit error vs. noise level. Dashed line corresponds to perfect sensor track information. ....	105

## Tables

Table 1: Biases and linear drift rates for the angular rates of four separate data sets.....	14
Table 2: Biases and linear drift rates for the determined angles for the same data sets as in Table 1 .....	14
Table 3: The target position, orientation and squared correlation inversion results, for the two cases where the IMU-derived trajectory and the video ground truth trajectory were used to position the EMI data of Data Set E.....	45
Table 4: The responses (units of $m^3$ ) that are induced when the primary field is aligned in turn along each of the three principal axes of the target, for each time gate of the EM61-HH.....	45
Table 5: Differences between ArcSecond and IMU Trajectories.....	98

## Acronyms

<b>2D</b>	<b>Two Dimensional</b>
<b>3D</b>	<b>Three Dimensional</b>
<b>EM</b>	<b>Electromagnetic</b>
<b>EMI</b>	<b>Electromagnetic Induction</b>
<b>GPS</b>	<b>Global Positioning System</b>
<b>IDL</b>	<b>Interactive Data Language</b>
<b>IMU</b>	<b>Inertial Measurement Unit</b>
<b>LED</b>	<b>Light Emitting Diode</b>
<b>MEMS</b>	<b>Micro Electromechanical Sensor</b>
<b>PC</b>	<b>Personal Computer</b>
<b>PDA</b>	<b>Personal Digital Assistant</b>
<b>RMS</b>	<b>Root Mean Square</b>
<b>UXO</b>	<b>Unexploded Ordnance</b>
<b>ZUPT</b>	<b>Zero Velocity Update</b>

# 1. Introduction

This work was a collaborative effort between Duke University and SAIC (formerly AETC Incorporated). The final report consists of two volumes. This first volume gives a complete description of the overall effort as it evolved and culminated in a successful demonstration of IMU-based positioning of a handheld EM61 sensor for data collection to support target characterization of buried UXO. Volume 2 is a complete report of the supporting activities at Duke University.

## 1.1. Background

Past studies have clearly demonstrated that commercial UXO sensors (specifically, the Geonics EM61 and EM61-HH, and the Geophex GEM-3) can be used effectively to discriminate between buried UXO and clutter *if, and only if*, the sensor position and orientation are precisely known while the data are collected ([1]–[4]). The problem is that it is not always easy to get sensor location information at the levels of accuracy needed for reliable discrimination and classification, i.e. within about a cm. A simple solution to the sensor positioning problem is to collect data on a fixed grid over the target using a template laid on the ground (see Figure 1). Although inexpensive and robust, this approach leaves much to be desired. A positioning system that is integral to the sensor and allows the operator to sweep the sensor around above the target is much preferred. This would permit use in rougher terrain and confined locations. It would also facilitate collection of a much higher density of data over the target. The grid approach provides a limited number of samples (e.g. 36 for a 6x6 grid) and requires signal to noise ratios greater than 25 or 30dB in order to get good target classification. Higher data density translates directly to improved signal to noise ratio at the processor output, and hence improved performance for



**Figure 1:** Collecting EM61-HH data on a grid over a suspected buried UXO item.

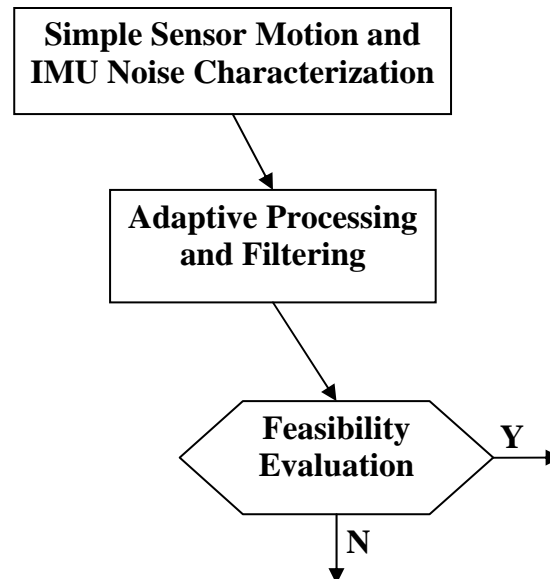
deeper targets. It is impractical to try to improve the data density with a grid template approach. However, with a freely swept system operating at 10Hz, the data density can be increased by a factor of 50-80 during the time required to carefully sample the grid using the current approach (3-5 minutes).

## **1.2. Objective**

The goal of this project was to develop an inexpensive, robust way to accurately determine the trajectory of a handheld UXO sensor as it is swept about above a suspected buried UXO item. In principle, the sensor position and orientation can be tracked using an inertial measurement unit (IMU) that measures accelerations and angular rates along three orthogonal axes. Whether a compact, inexpensive, rugged IMU based on micro-electromechanical systems (MEMS) technology is sufficient to do the job was a main focus of this project. Another point of focus was the development of processing procedures that combine the trajectory with the sensor output stream to characterize the target for discrimination between UXO and clutter

## **1.3. Technical Approach**

The approach taken early stages of this project is summarized in the block diagram below.



The first step was to characterize and develop parametric descriptions for the sensor motion and IMU errors, followed by the development of adaptive processing and filtering schemes to reduce the IMU errors. The idea here being to use the IMU errors to drive the estimation of the state of the sensor motion. Within this scheme, external aids to ensure that the IMU and position errors remain strongly correlated and converge to zero – such as the UXO sensor output or other independent references – were to be explored.

Initially, the project proceeded according to plan. Tests were conducted with the IMU and the EM61-HH in controlled laboratory-type environments. Significantly, this early work focused on constrained two-dimensional motion, and it was found that with rather straightforward processing, IMU-based positioning could be obtained with the precision required to support accurate dipole inversion of EM61-HH data. The IMU unit used in this early work was an inexpensive Crossbow IMU400CC-100. The data collections are described in §2, and the basic processing approach for integrating the IMU data is described in §3. In order to get accurate dipole inversion of the EM61-HH data, we had to incorporate a forward model that included the dynamic response characteristics of the EM61-HH, as discussed in §4.

During this period, the Duke University research effort focused on several signal processing approaches for handheld UXO sensor improvements that could be incorporated in the overall processing flow. To begin they explored system identification as a means to directly model the errors in the measured quantities (acceleration and angular rate). In this application, system identification determines the transfer function of the unknown filter from known input and output data, thus modeling the relationship between the observed IMU-derived data (output) and the ground truth (input). Because the IMU accelerometers and angular rate sensors are most accurate during different types of motion and have different limitations, adaptive error mitigation algorithms employing feedback loops to use the more accurate sensor (accelerometer or angular rate) to mitigate errors in the less accurate sensor (accelerometer or angular rate) were then developed and tested. This effort resulted in iterative integration algorithms for velocity stabilization and position calculation which were found to perform well for two-dimensionally constrained sweeping motions. A zero velocity update (ZUPT) algorithm was introduced for improved calculations of the velocities. The yaw angular rate was used to determine the zero-velocity points for nonlinear motion, and the acceleration and its integration quantity to find the zero-velocity points for linear motions. Results obtained for the two-dimensionally constrained motion tests indicated that this approach is capable of accurately positioning the handheld UXO sensor.

We used video capture for ground truth with the two-dimensionally constrained tests. That approach was not viable for unconstrained three dimensional motions. The Arcsecond laser positioning system was evaluated and found to be acceptable for ground truth for general three-dimensional motions, as discussed in §5. The tests with three dimensional motion are described and discussed in §6. The algorithms that worked well with the two-dimensionally constrained motion failed to produce accurate position information with the Crossbow IMU400CC-100 for three-dimensional motion. This was borne out by the Duke results. When applied to unconstrained three dimensional motions, estimates of the system parameters failed to converge, and plots of the measured accelerations versus the true accelerations showed no clear relationship between the measured and true accelerations. Overall, processing of unconstrained three-dimensional data produced results which do not meet the desired sensor positioning performance.

We concluded that the reason why we had good results in determining sensor location from the Crossbow IMU data for 2D motion but discouraging results for 3D motion was because of unacceptable levels of noise and drift in the Crossbow angle rate measurements. Accurate determination of the IMU's orientation is vital to getting accurate position information because even a very small error in angle can introduce erroneous gravity contributions to the X and Y accelerations, which in turn integrate up to large position errors. A higher quality Honeywell

HG1900 IMU was integrated with the EM61-HH by ENSCO under ESTCP project MM-0604. It is referred to as the Small-Area Inertial Navigation Tracking or SAINT system. We collaborated with MM-0604 to evaluate whether or not the SAINT could provide sufficiently accurate sensor position information to support reliable UXO/clutter discrimination. As discussed in §7, we were able to get discrimination quality geolocated data using the SAINT system at the Aberdeen Standardized UXO Test Site.

Finally, in §8 we summarize work demonstrating the feasibility of including sensor data in the track estimation process. The approach is based on the principle that the best model/data fit occurs when the sensor trajectory is correct. Slight errors in the trajectory degrade the fit quality. The idea is then to assume that the trajectory from the IMU is in error, and allow slight modifications of the trajectory in the EMI inversion process, iterating until the best fit to the data is achieved. Trajectory errors typically arise because of errors in estimating the IMU biases. By including the bias parameters in our EM inversion procedure, we were able to simultaneously determine the best track estimate along with the target parameters (location and principal axis polarizabilities). Simulations using this procedure showed that we can reduce 5 cm rms track errors to <5 mm rms.

## 2. Controlled Two-Dimensional Motions

The program plan called for a sequential approach using increasingly complex sensor motions:

- a) *Constrained Path* – Tightly constrained motion, with the sensor level and following a simple zigzag path above the target;
- b) *Controlled Sweep* – A natural sweeping motion back and forth over the target where the orientation of the sensor head varies in a natural fashion; and
- c) *Unconstrained Motion* – Arbitrary sensor path above the target.

This section describes the data collection process for controlled two-dimensional motions, comprising a) and b) above.

### 2.1. Measurement Setup

#### 2.1.1. Apparatus Description

The apparatus used in the data collection process is shown in Figure 2 below. A Crossbow IMU400CC-100 and a Geonics EM61-HH were secured at known fixed positions on a rigid wooden board. Collectively, the board and sensors are referred to throughout this report as *the body*. It is this body that we are interested in carefully tracking – initially through various tightly constrained maneuvers, and later by gradual easing of the constraints, as the above list details.

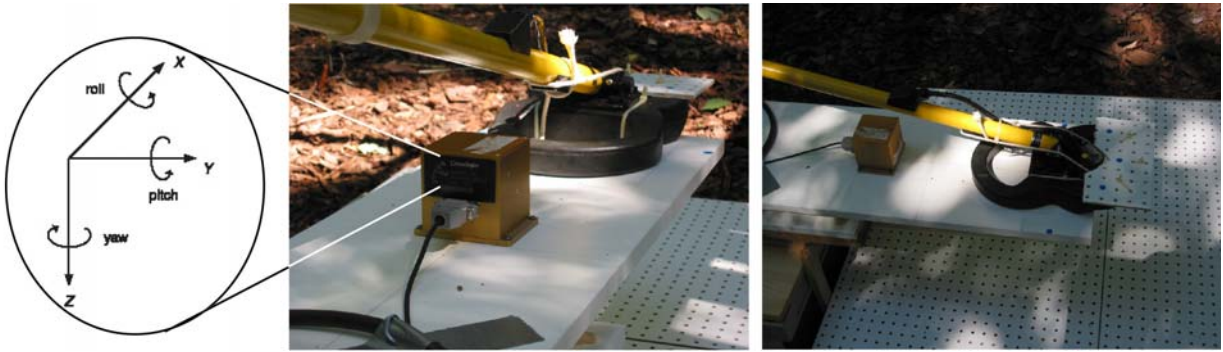


**Figure 2:** Two views of the body consisting of a Crossbow IMU400 (with its sensitive axes expanded on the left) and a Geonics EM61-HH.

The Crossbow IMU400CC-100 is a solid-state six-degree-of-freedom (6DOF) Inertial System designed for general measurement of the acceleration and angular rate vectors in dynamic environments. Its physical dimensions are 7.62 x 9.53 x 8.13 cm and it weighs less than 640 g. The three angular rate sensors are bulk micro-machined vibratory MEMS sensors that utilize the Coriolis force to measure the angular rates along each of the sensitive axes labeled in Figure 2. The three MEMS accelerometers are surface micro-machined silicon devices that use differential capacitance to independently sense the acceleration components along these same axes. When operating in the continuous update mode, the sampling rate of the IMU is just below 135 Hz.

The Geonics EM61-HH is a handheld time domain or pulsed electromagnetic induction (EMI) sensor with the transmit and receive coils offset from each other. The transmitted primary field induces eddy currents in the target, which in turn radiate a secondary field measured by the receive coil. The EM61-HH measures the secondary field at time delays of 147, 263, 414 and 613  $\mu$ s after the primary field shutoff at a sampling rate of 15 Hz.

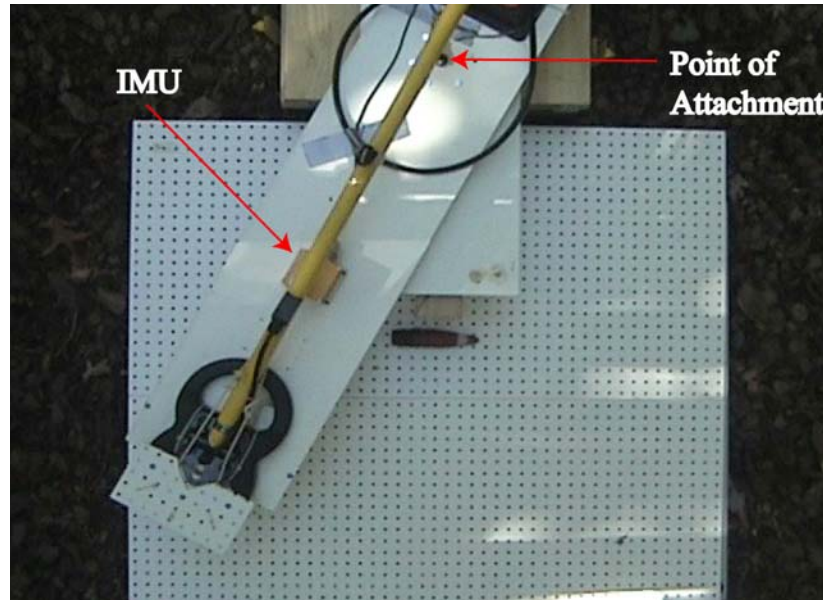


**Figure 3:** The apparatus as viewed from an overhead video camera. The point of attachment also served as a pivot point.

As is apparent from Figure 3 above, the body was laid on another rigid wooden board and attached to this at a point. The point served as a pivot point, about which the body was constrained to rotate in a purely planar trajectory. In addition, the underlying board was set on a linear rail system offering an additional translational component to the motion of the body, thereby allowing the body to move in a variety of planar patterns, including the simple zigzag paths alluded to in the list above.

A video camera was installed overhead the apparatus to provide ground truth. In fact, Figure 3 is a single frame extracted from the video data for one of several measurement scenarios undertaken. As a calibration aid for the video, a peg board with holes spaced 1" apart in a regular 2D grid pattern was used as the background. A smaller piece of the same board with 4 clearly labeled stickers was also attached to the EM61-HH sensor head (see Figure 4). These stickers were essential in tracking the body movement frame-by-frame, thereby allowing the extraction of ground truth positioning information from the video data. The extraction process was done manually, frame by frame, using a set of IDL routines to display the images and record locations of the cursor when centered over the dots.



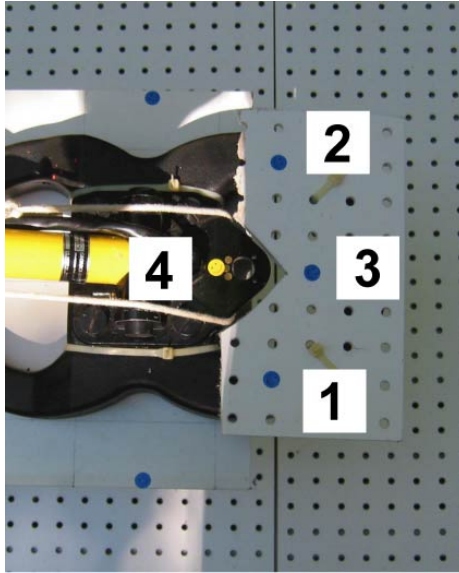


**Figure 4:** Stickers placed on the EM61-HH sensor head for ground truth positioning purposes.

### 2.1.2. Performed Scenarios

Several measurement scenarios were conducted. Figure 5 – Figure 9 below show the variety in these scenarios, spanning from a simple linear trajectory (Figure 5) to the more complicated zigzag sweeping trajectory (Figures 8 or 9). Since the mechanism of extracting ground truth positioning information from the video data via the stickers proved to be labor intensive, only a limited portion of the video data for each measurement scenario undertaken was subjected to this process. In fact, Figure 5 – Figure 9 represent all the ground truth positioning information that was extracted. Fortunately, this was more than enough data for the sensor motion characterization process.

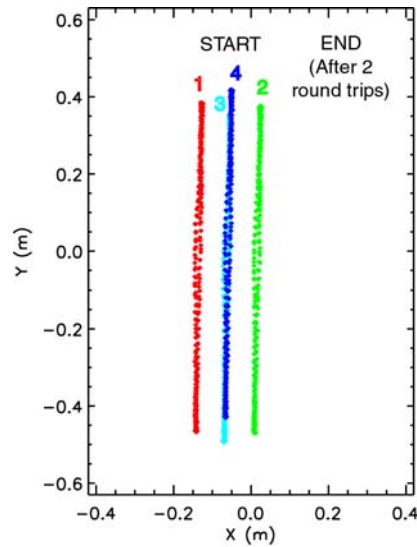


**Figure 5: Data Set A - Back & Forth Linear Trajectory over a 2'' Al sphere.**

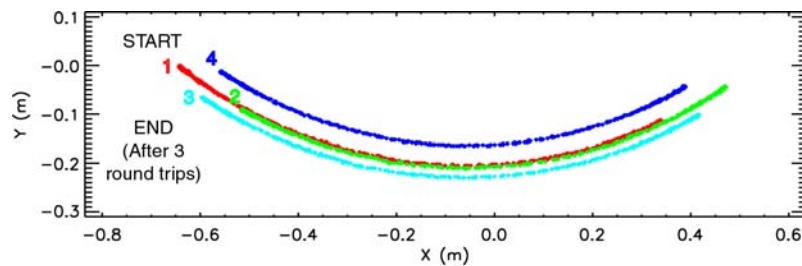


**Figure 6: Data Set B - Back & Forth Arced Trajectory over a 2'' Al sphere.**

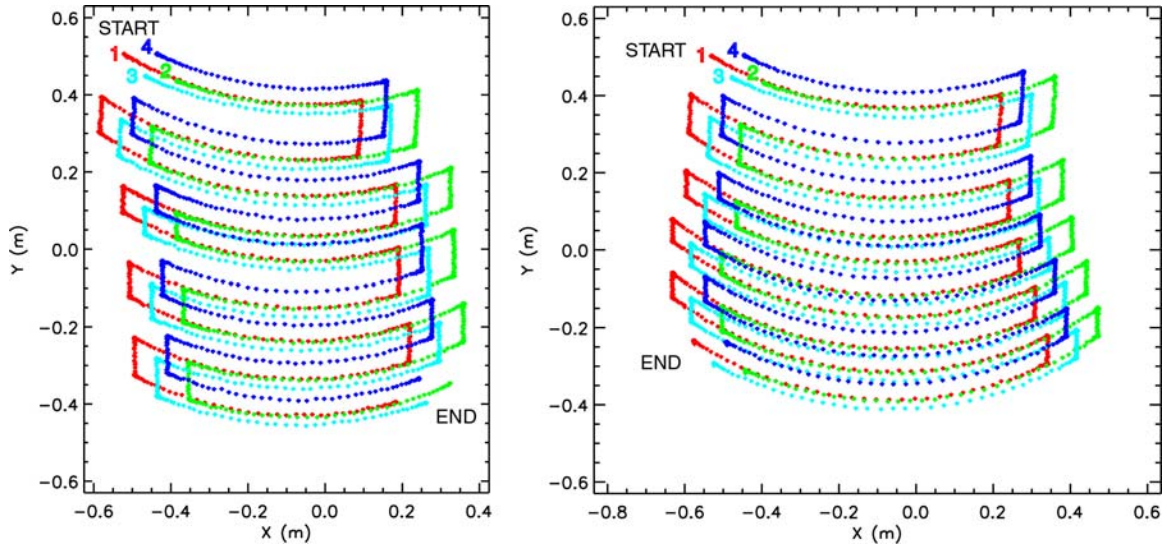


**Figure 7: Data Sets C1 & C2 - Two Back & Forth Sweep and Push Trajectories over a 2" Al sphere.**

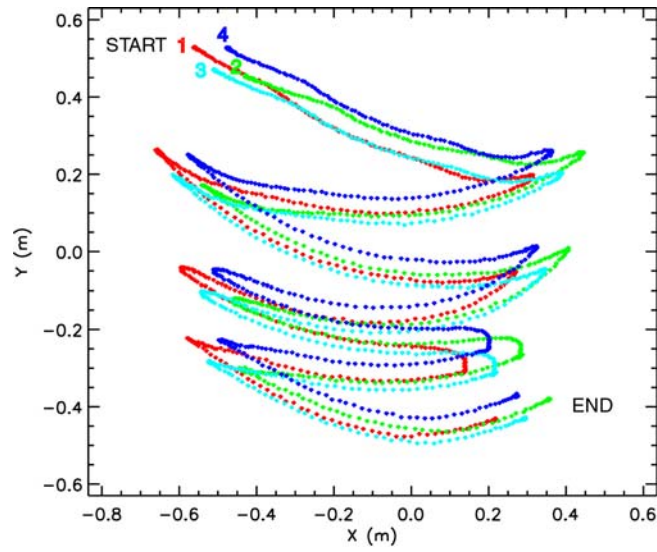


**Figure 8: Data Set D - Back & Forth Swing Trajectory over a 2" Al sphere.**

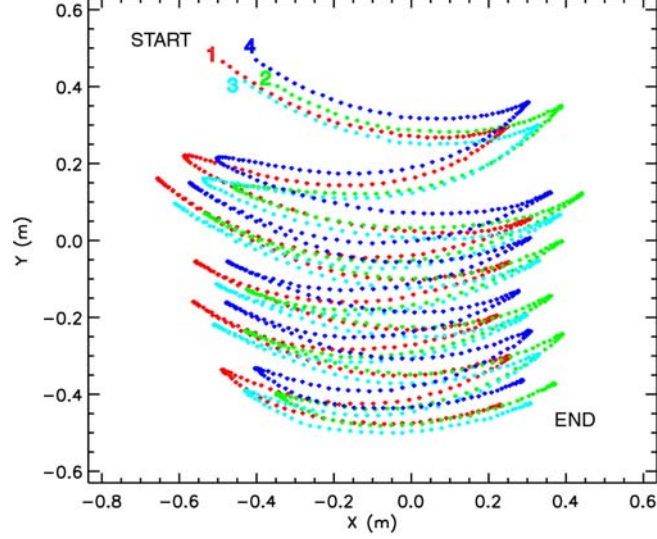


**Figure 9: Data Set E - Back & Forth Swing Trajectory over a 40mm Projectile.**

## 2.2. Definitions and Notation

This section introduces the notation used throughout this report and defines some key elements needed in comparing the IMU-derived results to the video ground truth.

Following standard practice, all vectors and matrices are represented as bold lowercase and uppercase letters, respectively. Each vector contains a superscript letter specifying the coordinate frame in which the vector is defined, as well as an optional subscript identifying an attribute of the vector (e.g.  $\mathbf{r}_{S_4}^v$  represents the position vector of sticker 4 as defined by the video coordinate frame, while  $\mathbf{a}_{IMU}^b$  represents the IMU acceleration vector as defined by the body coordinate frame).

In general, to transform a vector from one coordinate frame to another requires a combination of a translation and a rotation. The rotation can be completely defined by an orthonormal matrix representing an ordered sequence of three plane rotations involving the Euler angles - yaw, pitch and roll. An explicit representation of the rotation matrix  $\mathbf{R}_{b_0 \rightarrow b}(t)$  needed to transform a vector defined by the initial body frame at time  $t = t_0$  to the body-frame at time  $t$  is developed in Appendix A. Similar representations hold for the rotation matrix  $\mathbf{R}_{v \rightarrow b}(t)$  needed to transform a vector defined by the video frame to the body-frame at time  $t$  and the rotation matrix  $\mathbf{R}_{e \rightarrow b}(t)$  needed to transform a vector defined by the earth frame to the body-frame at time  $t$ , the difference being in the actual angle values.

Referring to Figure 10 below, it is clear that if the IMU represents the origin of the body coordinate frame  $O_b$  with the IMU sensitive axes coinciding with the body axes, then in the

video coordinate frame the position vector of the  $i$ -th sticker at time  $t$  – i.e.  $\mathbf{r}_{S_i}^v(t)$  – can be expressed in terms of the IMU position vector at time  $t$  as

$$(1) \quad \mathbf{r}_{S_i}^v(t) = \mathbf{r}_{IMU}^v(t) + \mathbf{R}_{b \rightarrow v}(t) \mathbf{d}_{S_i}^b \equiv \mathbf{r}_{IMU}^v(t) + \mathbf{R}_{b_0 \rightarrow v} \mathbf{R}_{b \rightarrow b_0}(t) \mathbf{d}_{S_i}^b$$

Here,  $\mathbf{d}_{S_i}^b$  represents the position vector of the  $i$ -th sticker as defined by the body coordinate frame, and  $\mathbf{R}_{b \rightarrow v}(t) \equiv \mathbf{R}_{b_0 \rightarrow v} \mathbf{R}_{b \rightarrow b_0}(t)$  represents the rotation matrix that transforms  $\mathbf{d}_{S_i}^b$  from the body frame to the video frame in terms of a rotation matrix that first transforms  $\mathbf{d}_{S_i}^b$  from the body frame at time  $t$  to the initial body frame at time  $t=t_0$ , followed by a time invariant rotation matrix that transforms  $\mathbf{d}_{S_i}^{b_0}$  from the initial body frame to the video frame.

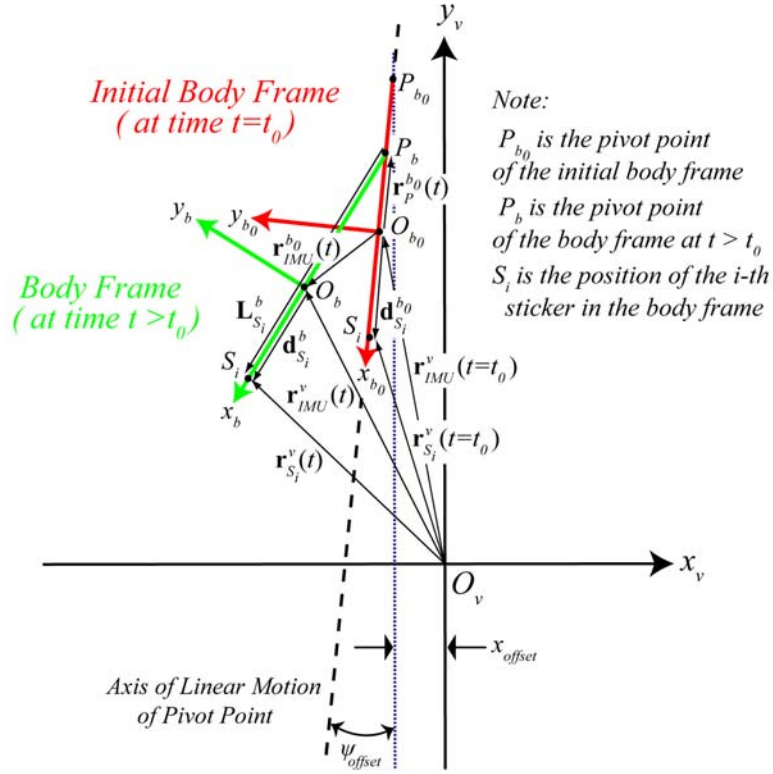


**Figure 10:** Schematic diagram showing the relevant vectors and coordinate frames.

It should also be clear from Figure 10 that

$$\mathbf{r}_{IMU}^v(t) = \mathbf{r}_{IMU}^v(t=t_0) + \mathbf{R}_{b_0 \rightarrow v} \mathbf{r}_{IMU}^{b_0}(t)$$

so that (1) can be rewritten as

$$(2) \quad \mathbf{r}_{S_i}^v(t) = \mathbf{r}_{IMU}^v(t = t_0) + \mathbf{R}_{b_0 \rightarrow v} \left( \mathbf{r}_{IMU}^{b_0}(t) + \mathbf{R}_{b \rightarrow b_0}(t) \mathbf{d}_{S_i}^b \right)$$

Finally, noting that

$$\mathbf{r}_{IMU}^v(t = t_0) = \mathbf{r}_{S_i}^v(t = t_0) - \mathbf{R}_{b_0 \rightarrow v} \mathbf{d}_{S_i}^{b_0}$$

we have, upon substituting into (2),

$$(3) \quad \mathbf{r}_{S_i}^v(t) = \mathbf{r}_{S_i}^v(t = t_0) + \mathbf{R}_{b_0 \rightarrow v} \left( \mathbf{r}_{IMU}^{b_0}(t) - \mathbf{d}_{S_i}^{b_0} + \mathbf{R}_{b \rightarrow b_0}(t) \mathbf{d}_{S_i}^b \right)$$

Equation (3) is the necessary expression whereby the IMU-derived results can be compared to the video ground truth.

### 3. Data Analysis and Signal Processing

#### 3.1. Inertial Measurement Unit

##### 3.1.1. Attitude Determination

The attitude of the IMU (and thus the body) is determined from the measured angular rates  $\omega_x$ ,  $\omega_y$  and  $\omega_z$ . Based on the Euler angle rotations,  $\psi$ ,  $\theta$  and  $\phi$  (yaw, pitch and roll, respectively) described in Appendix A, we have upon referring to Figure A1,

$$\omega_x \equiv \frac{d\phi}{dt} \hat{\mathbf{x}}'', \quad \omega_y \equiv \frac{d\theta}{dt} \hat{\mathbf{y}}'', \quad \text{and} \quad \omega_z \equiv \frac{d\psi}{dt} \hat{\mathbf{z}}',$$

where  $\hat{\mathbf{x}}''$ ,  $\hat{\mathbf{y}}''$  and  $\hat{\mathbf{z}}'$  are the unit vectors about which the respective rotations take place. Transforming these vectors to the body-frame at time  $t$ , we have from (A3)

$$\hat{\mathbf{x}}'' = \begin{bmatrix} 1 \\ 0 \\ 0 \end{bmatrix}, \quad \hat{\mathbf{y}}'' = \begin{bmatrix} 0 \\ \cos \phi \\ -\sin \phi \end{bmatrix},$$

and from (A2) and (A3)

$$\hat{\mathbf{z}}' = \begin{bmatrix} 1 & 0 & 0 \\ 0 & \cos \phi & \sin \phi \\ 0 & -\sin \phi & \cos \phi \end{bmatrix} \begin{bmatrix} -\sin \theta \\ 0 \\ \cos \theta \end{bmatrix} = \begin{bmatrix} -\sin \theta \\ \cos \theta \sin \phi \\ \cos \theta \cos \phi \end{bmatrix}$$

Thus, we can write

$$\begin{bmatrix} \omega_x \\ \omega_y \\ \omega_z \end{bmatrix} \equiv \begin{bmatrix} 1 & 0 & -\sin \theta \\ 0 & \cos \phi & \cos \theta \sin \phi \\ 0 & -\sin \phi & \cos \theta \cos \phi \end{bmatrix} \begin{bmatrix} \frac{d\phi}{dt} \\ \frac{d\theta}{dt} \\ \frac{d\psi}{dt} \end{bmatrix}$$

from which we get, by inversion,

$$(4) \quad \begin{bmatrix} \frac{d\phi}{dt} \\ \frac{d\theta}{dt} \\ \frac{d\psi}{dt} \end{bmatrix} \equiv \begin{bmatrix} 1 & \sin \phi \tan \theta & \cos \phi \tan \theta \\ 0 & \cos \phi & -\sin \phi \\ 0 & \frac{\sin \phi}{\cos \theta} & \frac{\cos \phi}{\cos \theta} \end{bmatrix} \begin{bmatrix} \omega_x \\ \omega_y \\ \omega_z \end{bmatrix}$$

For a level body constrained to move in a plane,  $\theta = \phi = 0$  and so (4) results in  $\omega_x = \frac{d\phi}{dt} = 0$ ,  $\omega_y = \frac{d\theta}{dt} = 0$  and  $\omega_z = \frac{d\psi}{dt}$ . This means that the only non-zero angular rate component is along the body  $z$ -axis, as expected, and the yaw angle can be determined by a straightforward integration of  $\omega_z$ . When  $\theta \neq 0$  and/or  $\phi \neq 0$ , however, the angular rates no longer decouple and the angles now need to be determined via (4).

Although every effort in the measurement process was made to constrain the body to move in a plane, deviations from this ideal inevitably creeps in. As an example, the IMU angular rates for Data Set C2 are shown below in Figure 11. It clear from the figure that both the  $x$  and  $y$  angular rate components are non-zero. This suggests that (4) must be used if the goal is to accurately characterize the motion of the body.

All three angular rates contain biases and trends. The red lines in Figure 11 represent linear fits to the  $t < -7s$  and  $t > 50s$  data, when the body was known to be stationary and in the same general position. The respective bias and drift values of the three angular rate components are listed in Table 1 for this data set, as well as several other data sets.

Data Set	$\omega_x$ bias ( $^{\circ}/s$ )	$\omega_x$ drift ( $\times 10^{-5} ^{\circ}/s^2$ )	$\omega_y$ bias ( $^{\circ}/s$ )	$\omega_y$ drift ( $\times 10^{-5} ^{\circ}/s^2$ )	$\omega_z$ bias ( $^{\circ}/s$ )	$\omega_z$ drift ( $\times 10^{-5} ^{\circ}/s^2$ )
C1	0.1538655	13.43	0.0709080	-5.94	0.0900197	12.51
C2	0.1605218	3.25	0.0690165	15.67	0.0952184	-6.87
D	0.1657144	-19.74	0.0849374	14.80	0.0911045	20.19
E	0.1769275	18.67	0.0674774	-3.56	0.0855456	23.50

**Table1: Biases and linear drift rates for the angular rates of four separate data sets.**

The angles calculated using (4), where the angular rates have had their linear trends removed, are shown in Figure 12 for Data Set C2. The angles in Figure 12 have also had a linear trend (again obtained from the  $t < -7s$  and  $t > 50s$  data) removed from them. The respective bias and drift values of the three angles are listed in Table 2 below for the same data sets as in Table 1. The blank cells in the table represent instances where a linear trend based on before and after stationary data is either inapplicable (i.e. the before and after data may represent clearly different positions), or is inadequate to describe the drift.

Data Set	$\phi$ bias ( $\times 10^{-3} ^{\circ}$ )	$\phi$ drift ( $\times 10^{-3} ^{\circ}/s$ )	$\theta$ bias ( $\times 10^{-3} ^{\circ}$ )	$\theta$ drift ( $\times 10^{-3} ^{\circ}/s$ )	$\psi$ bias ( $\times 10^{-3} ^{\circ}$ )	$\psi$ drift ( $\times 10^{-3} ^{\circ}/s$ )
C1	13.4	1.0	17.0	3.2	80.8	7.3
C2	-18.6	-2.1	-12.8	-2.2	-10.5	-11.6
D						
E			5.8	-5.3		

**Table 2: Biases and linear drift rates for the determined angles for the same data sets as in Table 1.**



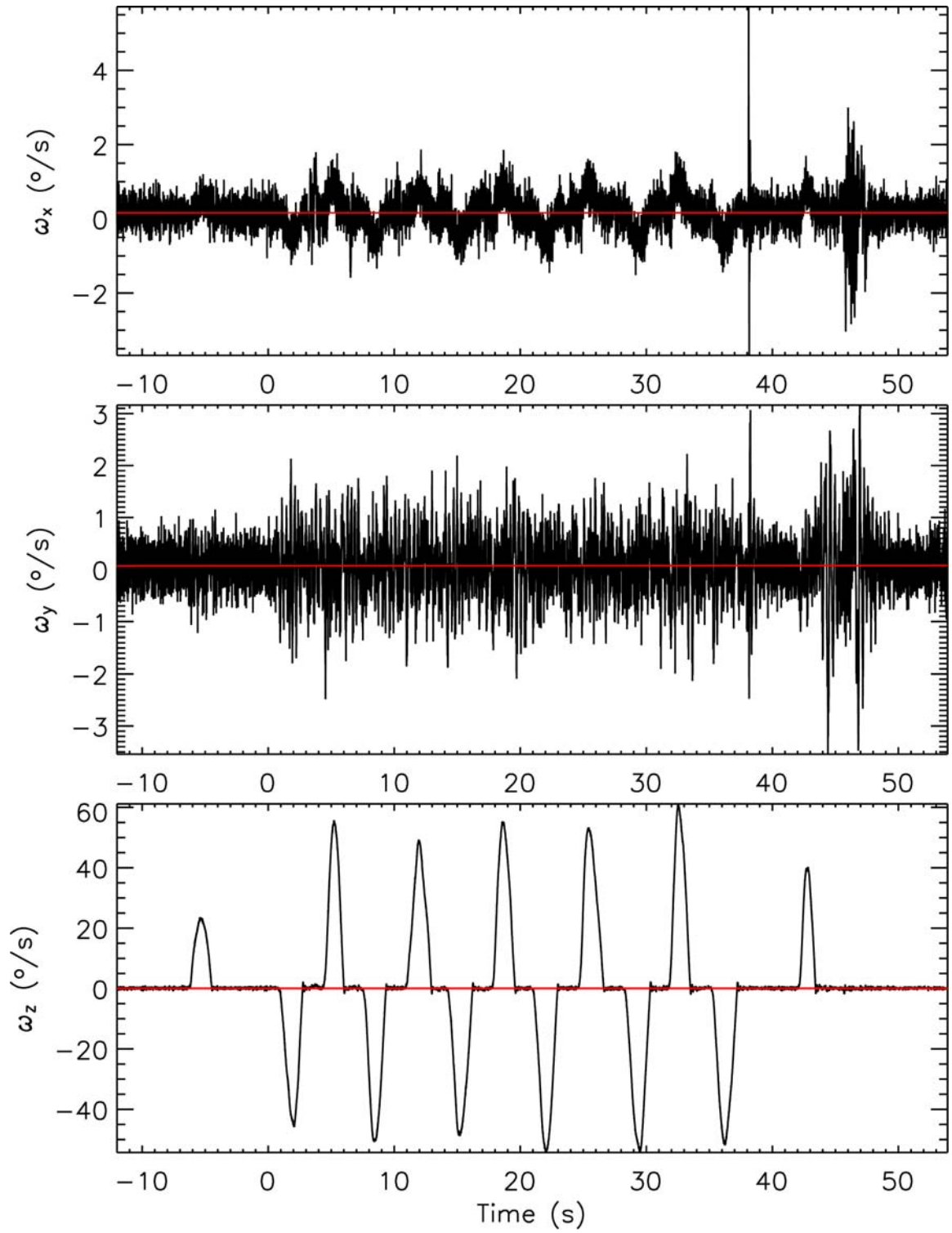


**Figure 11:** IMU angular rates for Data Set C2.

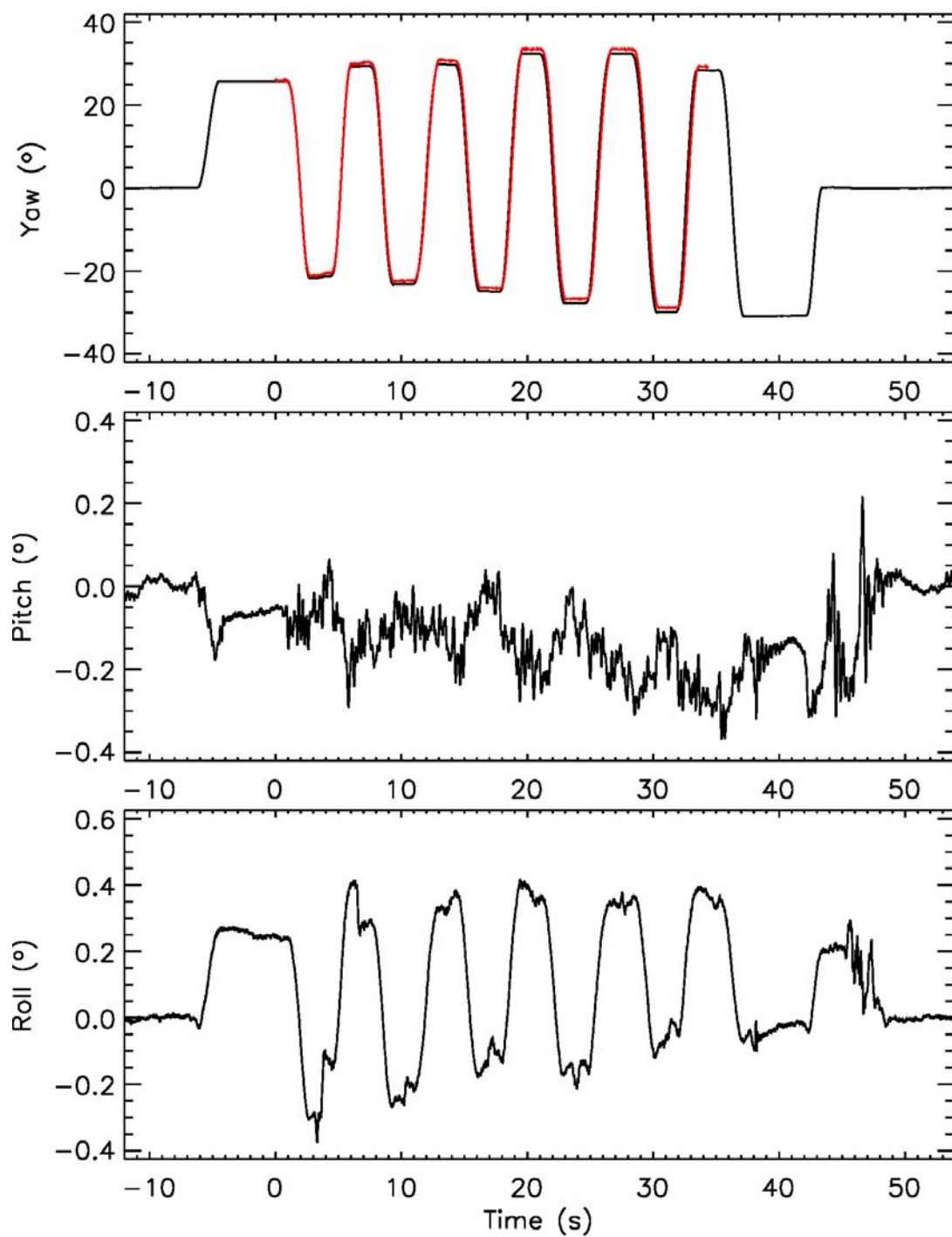


**Figure 12:** Angles determined via the IMU angular rates for Data Set C2. The over-plotted red curve represents the yaw angle determined from the video data.

The red yaw curve over-plotted in Figure 12 represents the yaw angle determined by using the video ground truth via

$$(5) \quad \psi_v(t) = \sin^{-1} \left( \frac{-(x_v(t) + x_{offset})}{|\mathbf{L}_{S_i}|} \right) - \psi_{offset}$$

where  $|\mathbf{L}_{S_i}|$  is the magnitude of the lever arm vector that points from the pivot point to the  $i$ -th sticker as shown in Figure 10;  $x_{offset}$  is the  $x$ -distance from the initial pivot point to the origin of the video coordinate frame; and  $\psi_{offset}$  is the angle between the axis of linear motion (i.e. the path the pivot point takes – see Figure 10) and the video  $y$ -axis.

In the determination of  $\psi_v(t)$ , the following assumptions were made:

- $|\mathbf{L}_{S_i}| = 0.907$  m;
- $x_{offset} = 0.032$  m;
- $\psi_{offset} = 1.11^\circ$ ; and
- the video and the IMU are perfectly synchronized

If the same above assumptions are made for the other data sets, good general agreement between the IMU determined yaw and the video determined yaw seems to hold (see Figure 13). The most obvious mismatch appears to be in the trends of the two curves, as well as the relative timing between the video and the IMU. The trend mismatches, also apparent in the yaw of Figure 12, are more than likely due to the imprecise representations of the IMU angular rate drifts as linear drifts. Fortunately, as we shall see in the next section, a possibility of refining this representation suggests itself based on enforcing consistency between what the angular rates tell us, and what the accelerations tell us, about the physics of the particular situation. The relative timing mismatches, on the other hand, are greatly minimized by simply remapping the IMU time stamps as

$$(6) \quad t_{IMU} \rightarrow (1 + \delta_t)(t_{IMU} + t_{offset})$$

where  $\delta_t$  is a scale factor and is fixed at a value of 0.005 and  $t_{offset}$  is the relative time offset between the IMU and the video, and is given in multiples of sample time intervals.

It should be noted that a linear trend was removed from the yaw of Data Set C1 (refer to Table 2 for the coefficient values), whereas no trends were removed from the yaws of Data Sets D and E. The latter was simply due to the fact that the choice of initial and final yaw values were different, making the removal of a linear trend based on the before and after stationary data inapplicable. An effort was consciously made, wherever possible, to choose the IMU data segments so that trend removal was viable. However, this criterion was usually overridden when given the option of choosing longer and quieter stationary segments of IMU data with different initial and final values.

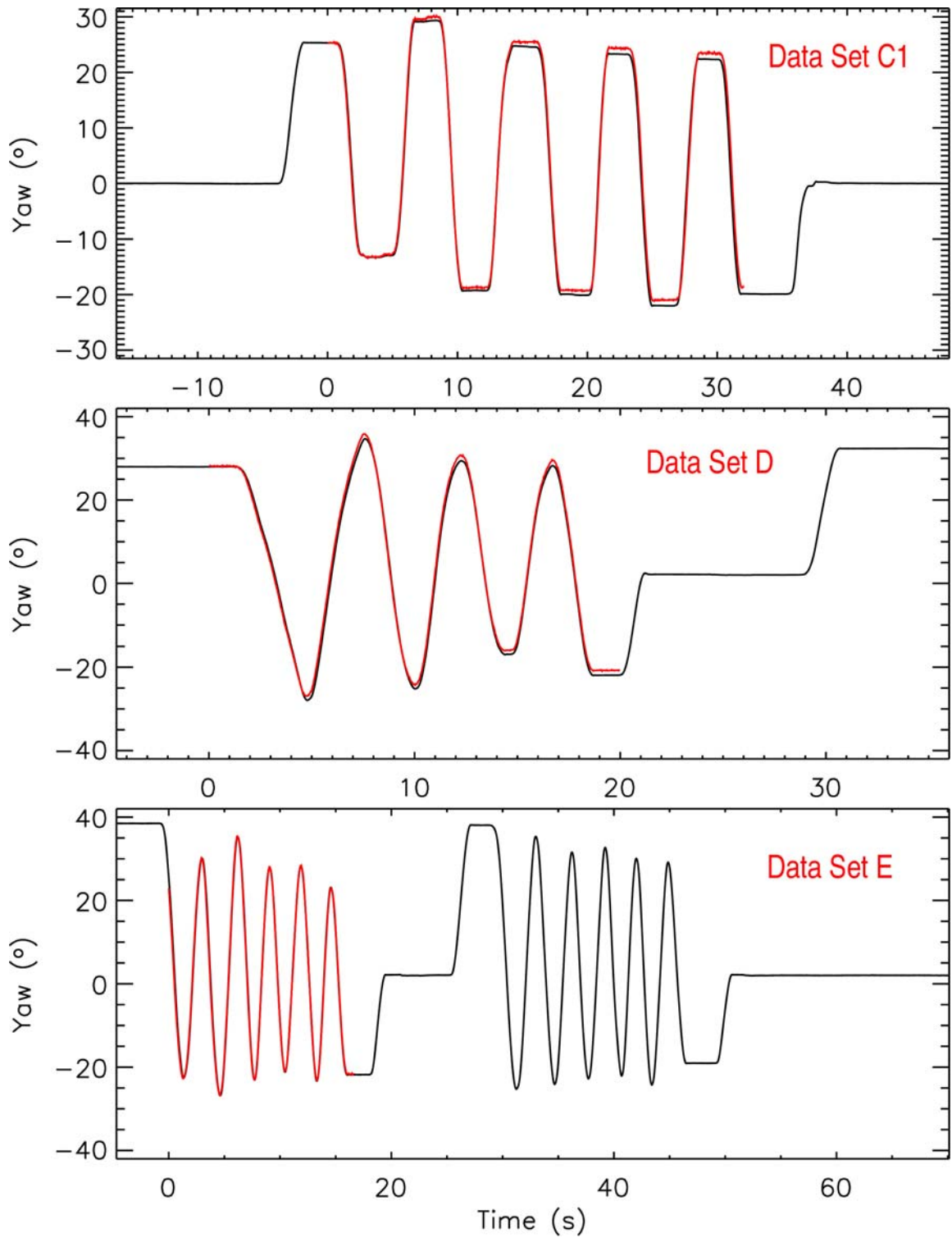


**Figure 13:** The computed yaw angles for other IMU data sets. The over-plotted red curves represent the yaw angle determined from the video data.

### 3.1.2. Velocity and Position Determination

The velocity and position vectors of the IMU (and thus the body) are determined from the measured accelerations  $a_x$ ,  $a_y$  and  $a_z$ . Since the pivot point is constrained to move along the axis of linear motion, as shown back in Figure 10, it is useful to explicitly consider this point in the analysis. In the initial body frame, we can write

$$(7) \quad \mathbf{r}_{IMU}^{b_0}(t) = \mathbf{r}_P^{b_0}(t) - \mathbf{R}_{b \rightarrow b_0}(t) (\mathbf{d}_{S_i} - \mathbf{L}_{S_i})^b = \mathbf{r}_P^{b_0}(t) - \mathbf{R}_{b \rightarrow b_0}(t) \mathbf{d}_P^b$$

where  $\mathbf{r}_P^{b_0}(t)$  represents the position vector of the pivot point at time  $t$  expressed in the initial body frame; and  $(\mathbf{d}_{S_i} - \mathbf{L}_{S_i})^b \equiv \mathbf{d}_P^b$  is the vector that points from the IMU to the pivot point and is independent of  $i$ . By definition,  $\mathbf{r}_{IMU}^{b_0}(t = t_0) \equiv 0$ .

Differentiating (7) gives the following result for the velocity of the IMU at time  $t$  expressed in the initial body frame (notation adopted from [5]):

$$(8) \quad \mathbf{v}_{IMU}^{b_0}(t) = \mathbf{v}_P^{b_0}(t) - \mathbf{R}_{b \rightarrow b_0}(t) \boldsymbol{\Omega}_{b_0b}^b(t) \mathbf{d}_P^b$$

where

$$(9) \quad \boldsymbol{\Omega}_{b_0b}^b(t) \equiv (\boldsymbol{\omega}_{b_0b}^b(t) \times) = \begin{bmatrix} 0 & -\omega_z(t) & \omega_y(t) \\ \omega_z(t) & 0 & -\omega_x(t) \\ -\omega_y(t) & \omega_x(t) & 0 \end{bmatrix}$$

is a skew-symmetric matrix that defines the cross product vector operation and  $\boldsymbol{\omega}_{b_0b}^b(t)$  reads as the rate of angular rotation vector of the body frame at time  $t$  relative to the initial body frame at time  $t = t_0$ , expressed in the body-frame at time  $t$ . Note that  $\omega_x(t)$ ,  $\omega_y(t)$  and  $\omega_z(t)$  are simply the angular rate components as measured via the IMU at time  $t$ , relative to the respective components measured at time  $t = t_0$ ,

Differentiating (8) gives the following result for the acceleration of the IMU at time  $t$  expressed in the initial body frame:

$$(10) \quad \mathbf{a}_{IMU}^{b_0}(t) = \mathbf{a}_P^{b_0}(t) - \mathbf{R}_{b \rightarrow b_0}(t) \left[ \boldsymbol{\Omega}_{b_0b}^b(t) \boldsymbol{\Omega}_{b_0b}^b(t) + \frac{d\boldsymbol{\Omega}_{b_0b}^b(t)}{dt} \right] \mathbf{d}_P^b$$

where the first term on the right hand side represents the linear acceleration of the pivot point and is directed along the axis of linear motion of Figure 10; the second term represents the centripetal acceleration and is directed towards the pivot point; and the third term is due to the angular acceleration and points in the direction of rotation, orthogonal to the centripetal vector.

Since  $\mathbf{a}_{IMU}^{b_0}(t)$  in (10) does not include the influence of the earth frame gravity vector  $\mathbf{g}$ , but the IMU accelerometer components do, we write

$$(11) \quad \mathbf{a}_{IMU}^{b_0}(t) = \mathbf{R}_{b \rightarrow b_0}(t) [\mathbf{a}_{IMU}^b(t) - \mathbf{R}_{e \rightarrow b}(t) \mathbf{g}]$$

where  $\mathbf{a}_{IMU}^b(t)$  denotes the acceleration vector at time  $t$  as measured by the IMU.

Finally, equating (10) and (11) gives

$$(12) \quad \mathbf{a}_{IMU}^b(t) = \mathbf{R}_{b_0 \rightarrow b}(t) \mathbf{a}_P^{b_0}(t) - \left[ \mathbf{\Omega}_{b_0 b}^b(t) \mathbf{\Omega}_{b_0 b}^b(t) + \frac{d\mathbf{\Omega}_{b_0 b}^b(t)}{dt} \right] \mathbf{d}_P^b + \mathbf{R}_{e \rightarrow b}(t) \mathbf{g}$$

Equation (12) explicitly represents the IMU accelerometer values in terms of the four possible contributions to the acceleration: linear, centripetal, angular and gravitational.

At this point, it is important to reflect on the significance of equation (12). Ignoring the linear contribution to the acceleration for the time being, it should first be noted that the centripetal and angular contributions are completely determined via the IMU angular rates and a known time-invariant vector (i.e.  $\mathbf{d}_P^b$ ). It should further be noted that the gravitational contribution is also determined via the IMU angular rates, albeit indirectly through the body attitude (i.e. angular) computations. However, here the use of some initial stationary accelerometer data is also necessary in order to initialize the relative alignment of the earth and body frames. All in all, the essence of what emerges from examining (12) is that independently measured quantities can be related through the physics of the particular situation, leading to opportunities for comparison and correction schemes.

In order to elaborate, we focus on three specific well-defined measurement situations: the pure rotational motion of Data Set B (Figure 6); the rotational and linear motion of Data Set C2, where the motions are uncoupled (Figure 7); and the rotational and linear motion of Data Set E, where the motions are coupled (Figure 9).

### 3.1.2.1. Pure Rotational Motion

Data Set B represents a special case where the linear contribution in (12) is non-existent. The  $x$ ,  $y$  and  $z$  IMU accelerometer values for this data set are shown in Figure 14 – Figure 16. Within each of the figures, the right hand side of (12) – as computed using the IMU angular rates – is shown in the top panel in red, while the separate centripetal, angular and gravitational contributions are displayed in the lower panel. It is clear from the figures that there is reasonable agreement between what the accelerometers tell us and what the angular rates tell us, but that there is room for improvement. This is especially evident when looking at the gravitational contribution in Figure 14 and noting the bias differences relative to the accelerometer data during stationary periods – i.e. when all the other contributions are zero. Also evident when looking at the angular acceleration contributions in Figure 15 and Figure 16, is the fact that the differentiation operation injects unwanted noise. This problem can largely be overcome by low

pass

filtering,

but

a

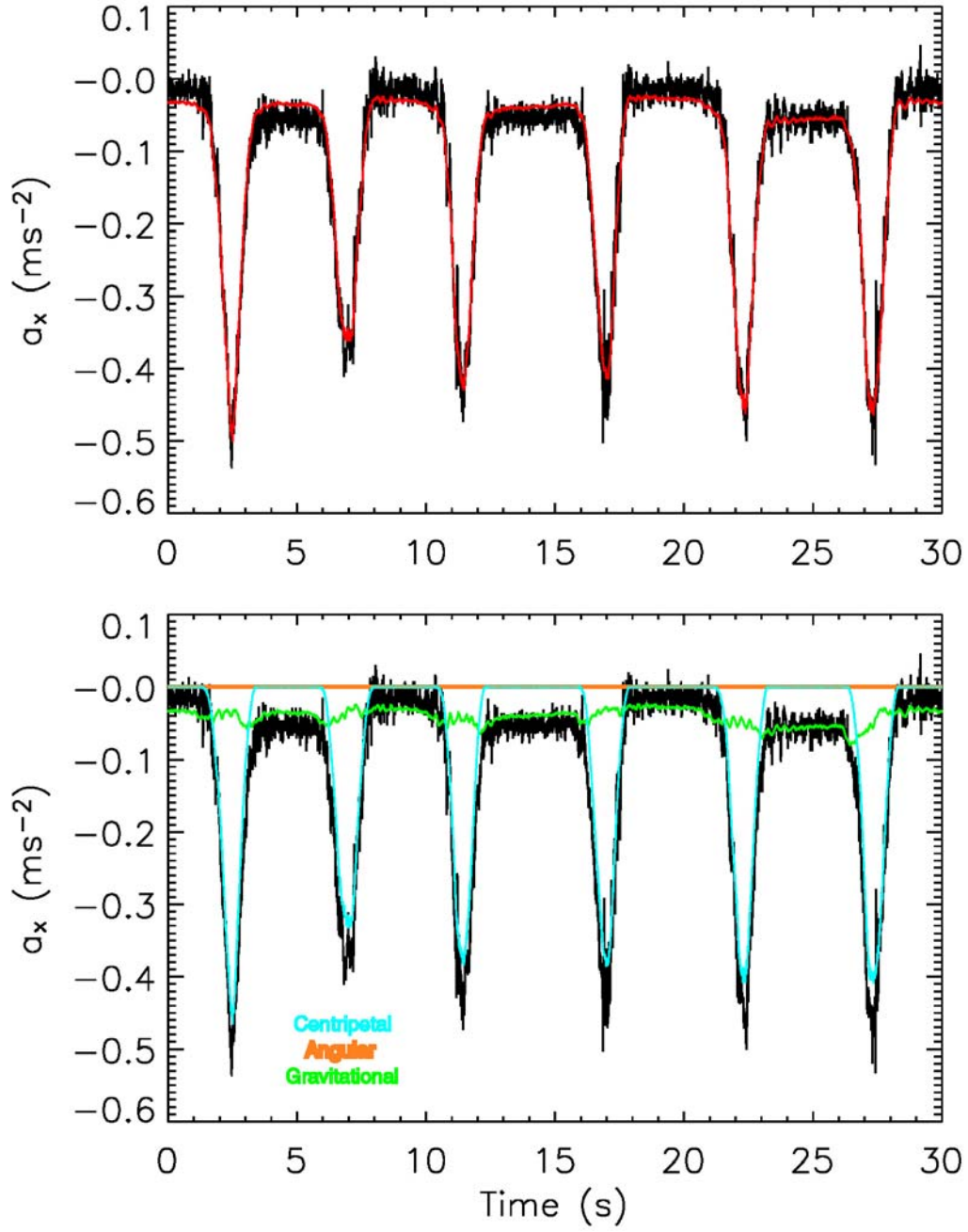


**Figure 14:** IMU x-component accelerometer values for Data Set B. The red curve in the top panel represents the x-component of the right hand side of equation (12), as computed via the IMU angular rates. The colored curves in the bottom panel show the respective contributions to the x-component of the acceleration.



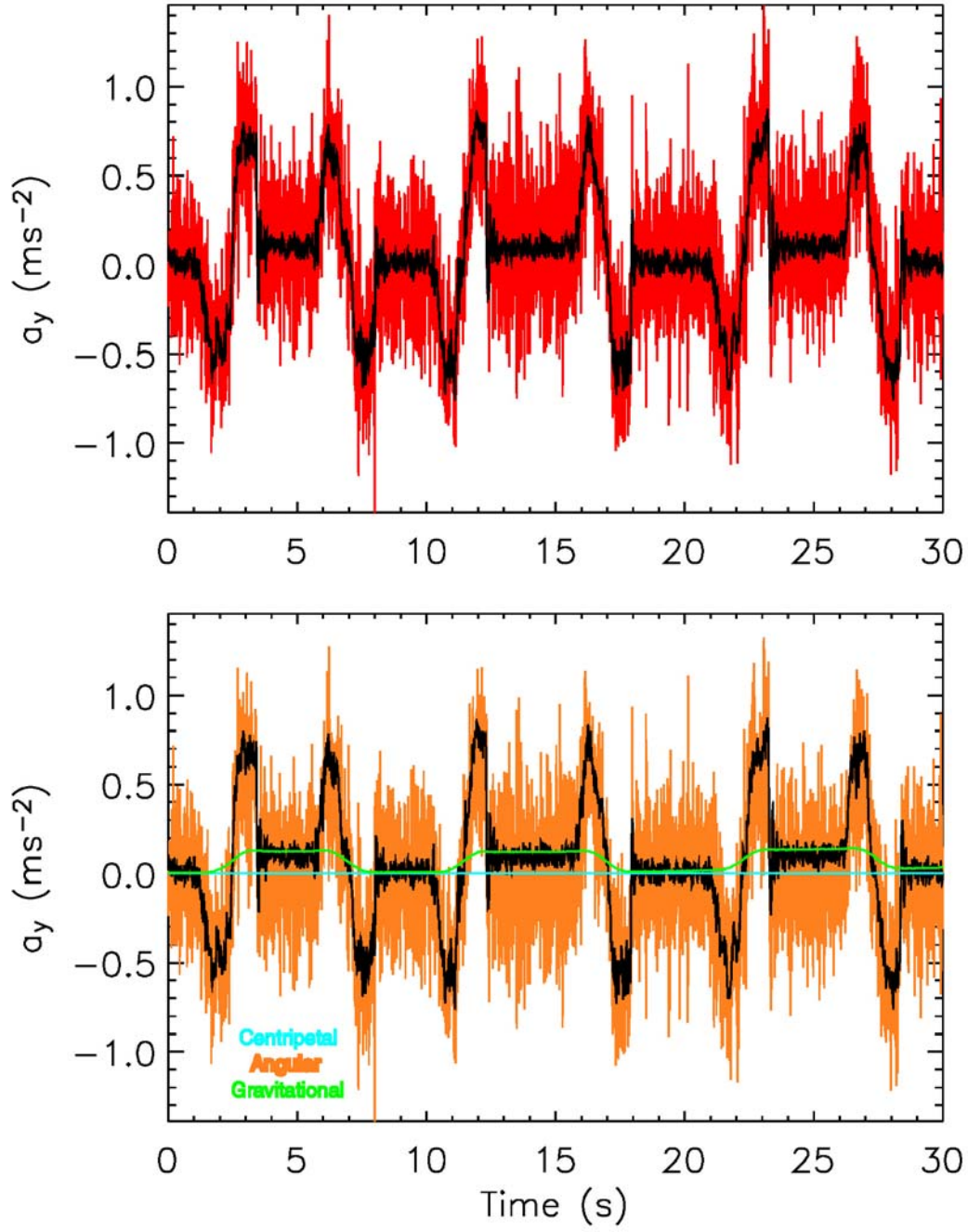


**Figure 15:** IMU y-component accelerometer values for Data Set B. The red curve in the top panel represents the y-component of the right hand side of equation (12), as computed via the IMU angular rates. The colored curves in the bottom panel show the respective contributions to the y-component of the acceleration.

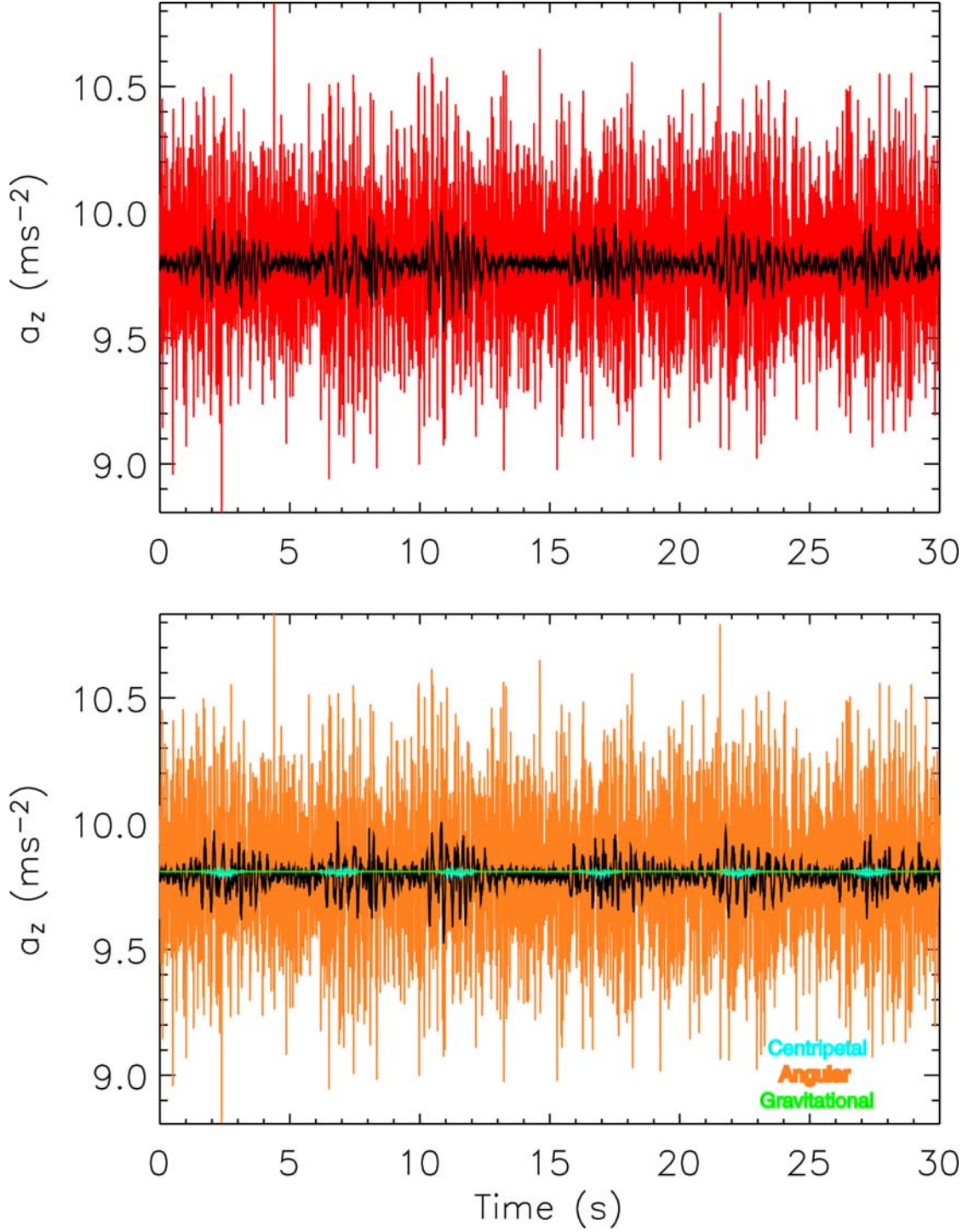


**Figure 16:** IMU z-component accelerometer values for Data Set B. The red curve in the top panel represents the z-component of the right hand side of equation (12), as computed via the IMU angular rates. The colored curves in the bottom panel show the respective contributions to the z-component of the acceleration.

more natural solution would be to ask whether it is possible to avoid using the differentiation operation altogether and still have a viable error correcting scheme.

To determine the velocity and position of the body for Data Set B, we begin by subtracting out the gravitational contribution from the three IMU accelerometer components. Figure 17 shows the result of integrating the gravitationally-compensated  $x$  and  $y$  accelerometer values to get the respective velocity components in the initial body frame (black curves). Also shown on the same plots (green curves) are the velocity components computed independently using the IMU angular rates via (8). It is obvious, upon comparison, that the use of the IMU angular rates produce much more stable results. This observation is compounded when looking at the determined IMU positions as shown in Figure 18. In this case, the black curves represent the result of integrating the black curves of Figure 17, whereas the green curves are computed directly from (7) using the IMU angular rates.

To demonstrate just how stable the IMU angular rate results are, we compare the position determination using the IMU angular rates via (7) with the ground truth positions extracted from the video data. The comparison is given in Figure 19 in the video frame (i.e. the coordinate system of Figure 6) for sticker 4, with the ground truth data over-plotted in red. Figure 20 shows details of the mismatch for both the  $x$  and  $y$  positions. Although biases remain that are likely attributable to video distortion errors, the good news seems to be that over the length of 30 seconds the linearly-compensated measured angular rates appear to be very stable.

### 3.1.2.2. Uncoupled Rotational and Linear Motion

Data Set C2 represents the case where the motion of the body is decoupled into a rotational segment followed by a linear segment, in alternating fashion. The  $x$ ,  $y$  and  $z$  IMU accelerometer values for this data set are shown in Figure 21 and Figure 22. In Figure 21, the linear contributions – as computed by (12) via both the IMU acceleration and angular rate values – are over-plotted in red. These clearly show the decoupled nature of the motion, where there is good agreement to alternating portions of the acceleration components. The three other separate contributions to the acceleration components are shown over-plotted in Figure 22. These reaffirm the notion based on Figure 21 that the motion is decoupled.

As in the case of the purely rotational motion of Data Set B, it is instructive to compare the velocity components in the initial body frame as derived by integrating the gravitationally-compensated accelerometer components to those derived using the IMU angular rates via (8). These are respectively represented as the black and red curves of Figure 23. As before, the linear contribution in (8) is neglected, not because it is non-existent, however, but because it cannot be determined from the IMU angular rates.

The fact that the linear and rotational motions are uncoupled in Data Set C2 allows us to readily correlate the black and red curves of Figure 23. This provides us with the means to completely characterize, and therefore correct for, the drift in the gravitationally-compensated accelerometer components. If we use the simple approach of characterizing the mismatch of the correlated data by a polynomial, we find that the choice of quadratics are sufficient (refer to Figure 24). It should be noted that the mismatches we are attempting to characterize here are, via (8), the velocity components of the pivot point in the initial body frame with drifts included.

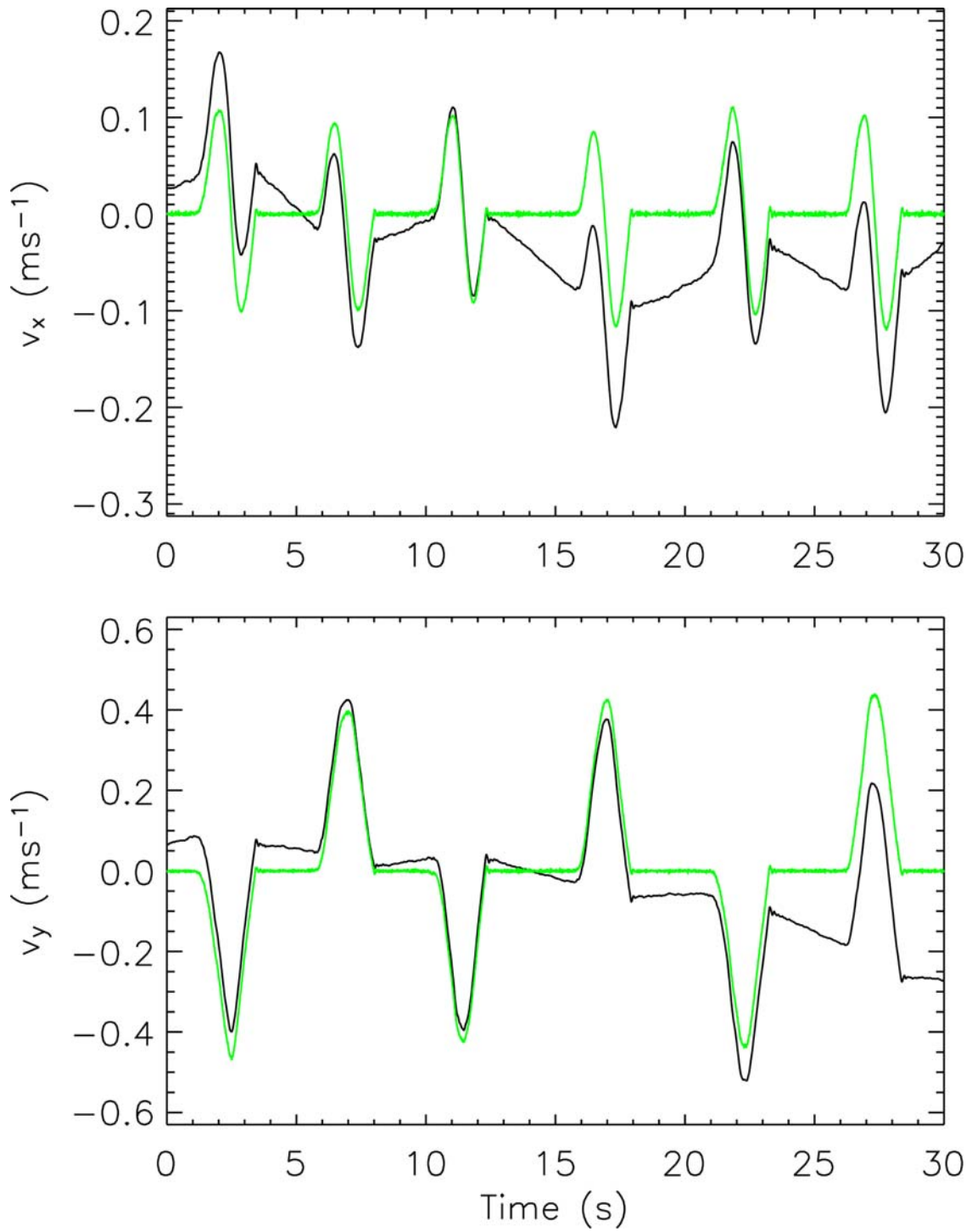


**Figure 17:** The accelerometer-derived (black) vs. the gyroscope-derived (green) velocity components for the IMU in the initial body frame for Data Set B.

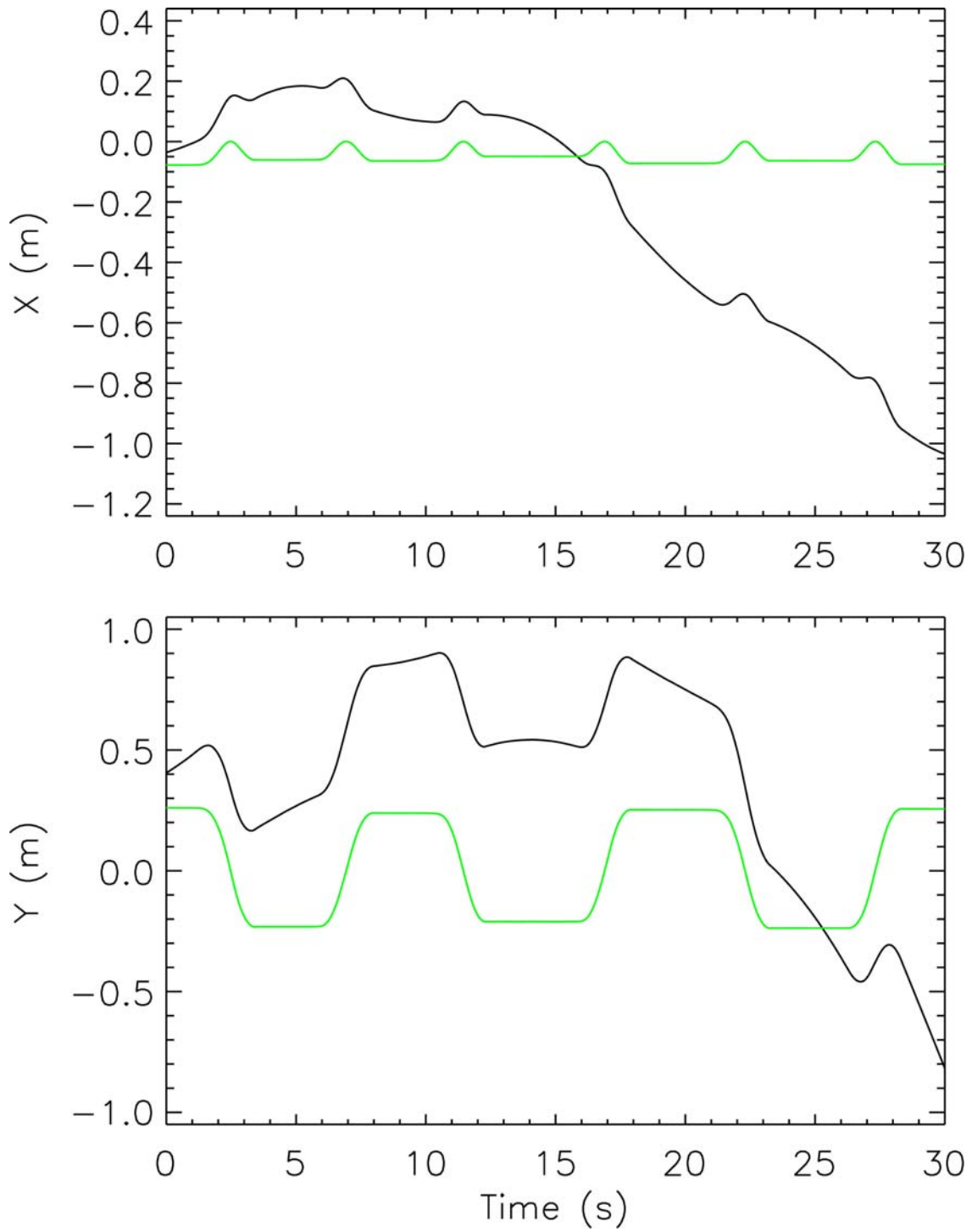


**Figure 18:** The accelerometer-derived (black) vs. the gyroscope-derived (green) IMU positions in the initial body frame for Data Set B.

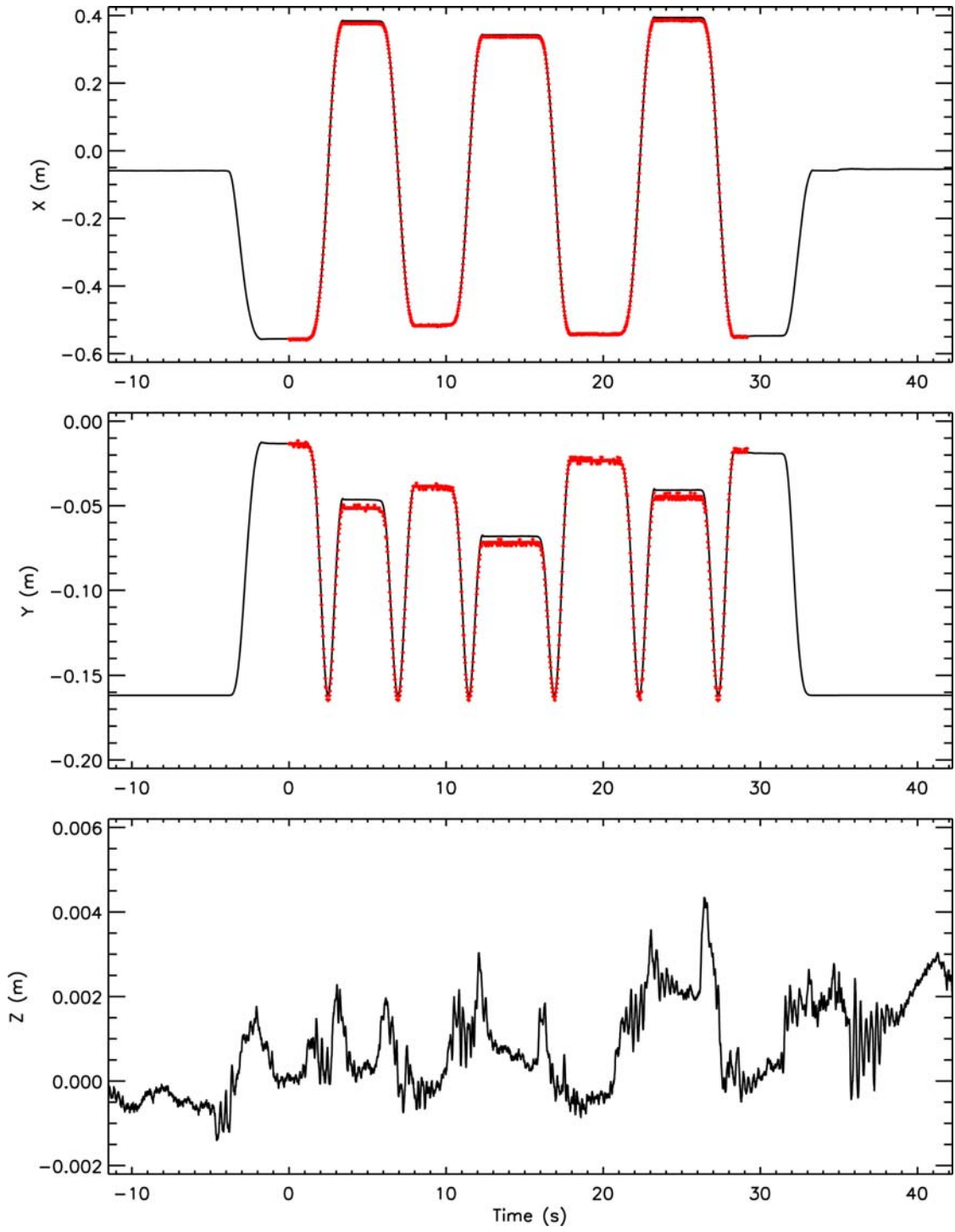


**Figure 19:** The gyroscope-derived vs. video ground truth (red) positions for sticker 4 in the video frame.



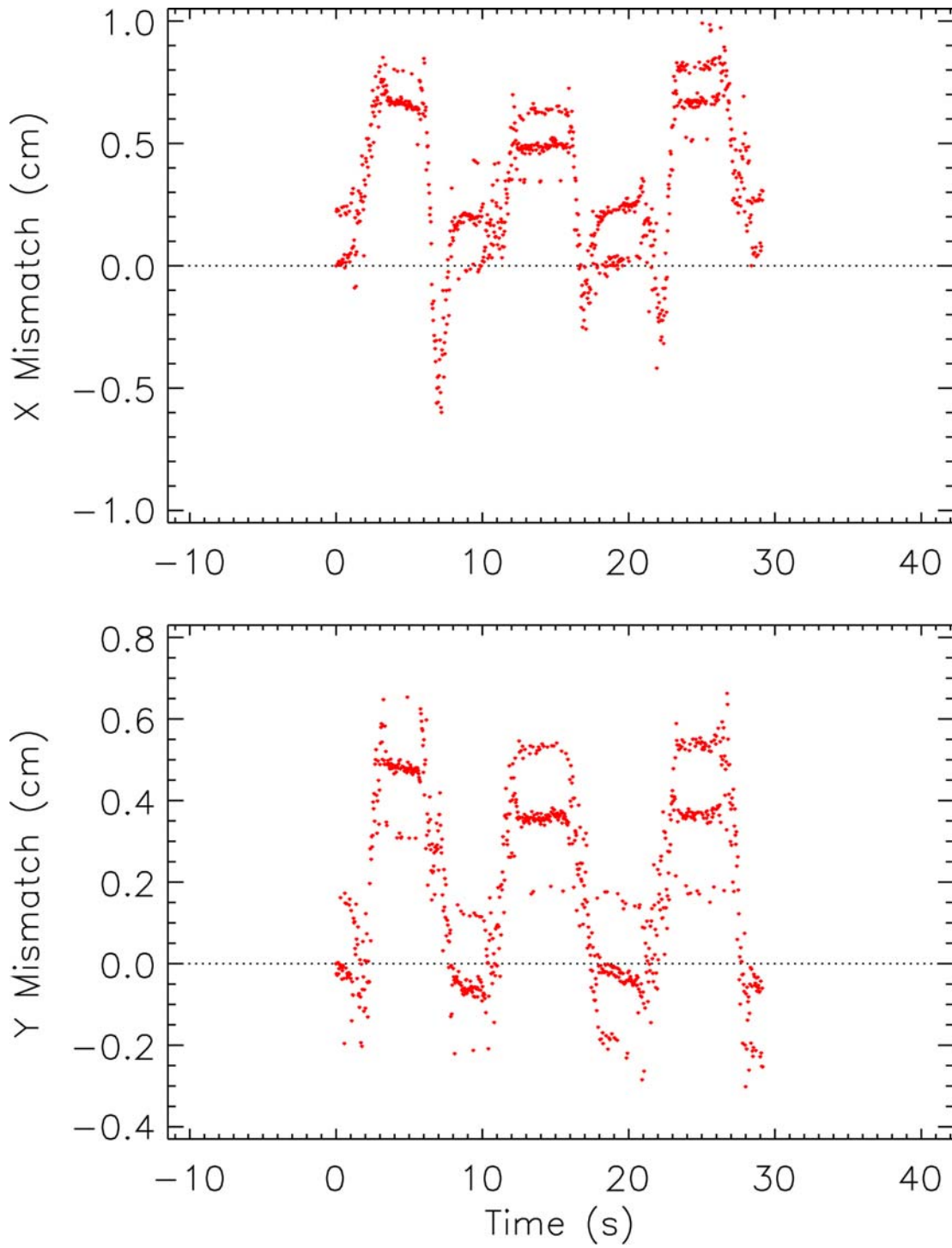


**Figure 20:** The mismatches between the gyroscope-derived and the video ground truth X and Y positions of Figure 19.

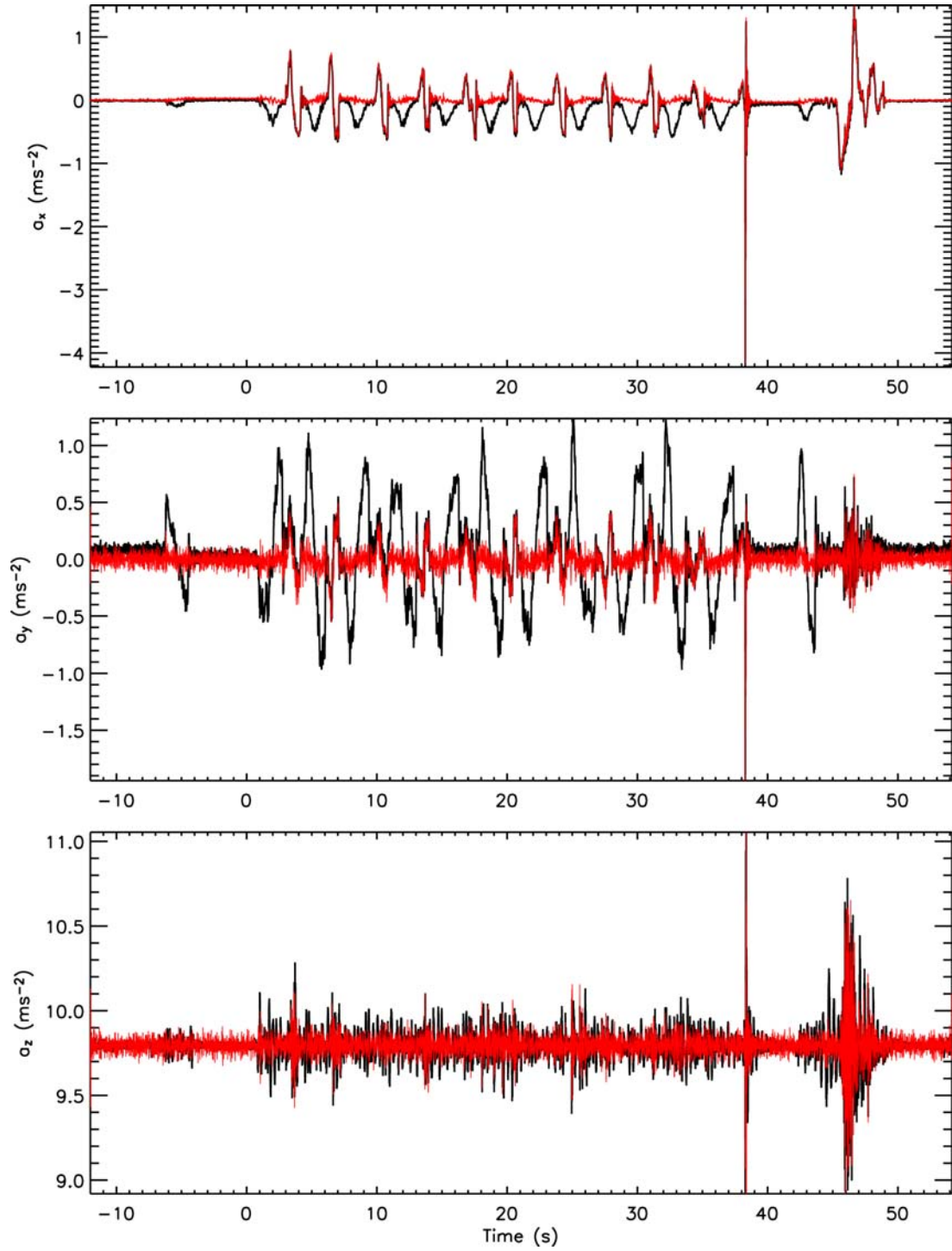


**Figure 21: Acceleration components as measured via the IMU for Data Set C2. The over-plotted red curves represent the linear contribution based on equation (12).**



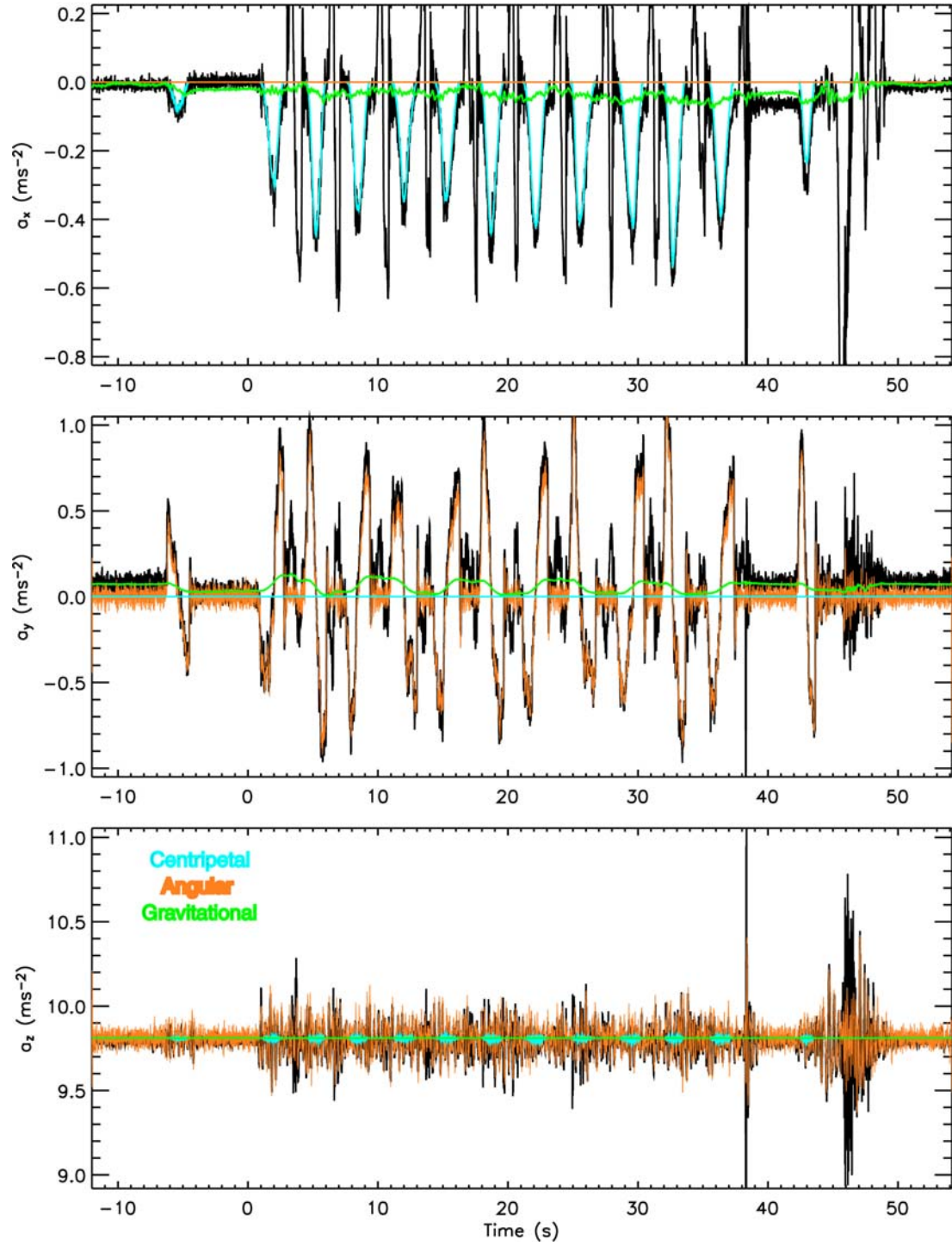


**Figure 22:** Acceleration components as measured via the IMU for Data Set C2. The over-plotted colored curves show the respective contributions to the acceleration components.

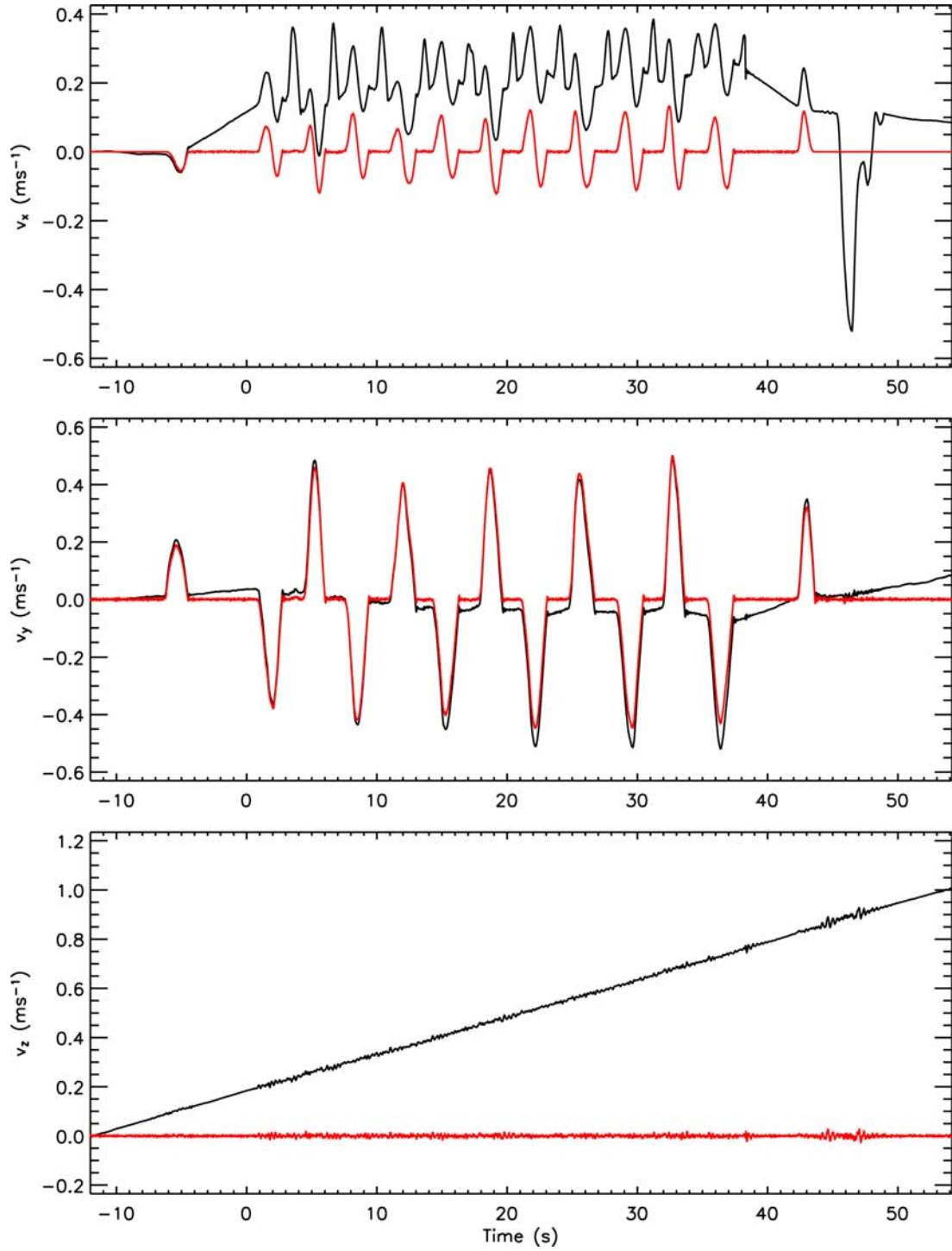


**Figure 23:** The accelerometer-derived (black) vs. the gyroscope-derived (red) velocity components for the IMU in the initial body frame for Data Set C2. The gyroscope-derived velocity components neglect the linear contributions to velocity, as a matter of definition, but remain much more stable.

The quadratic-corrected accelerometer-derived velocity components are represented in Figure 25 by the green curves. It is obvious that although the agreement with the red curves (i.e. the velocity components derived by using the IMU angular rates) has improved, the match remains far from perfect. However, judging from Figure 26, the positions obtained by integrating the quadratic-corrected accelerometer-derived velocity components (denoted by the green curves) show reasonably good agreement with the ground truth positions extracted from the video data (denoted by the red curves), especially when compared to the positions obtained by integrating the uncompensated accelerometer-derived velocity components (denoted by the black curves). In fact, as Figure 27 shows, the match is usually within a few centimeters and, as Figure 28 demonstrates, adheres generally well to the true trajectory.

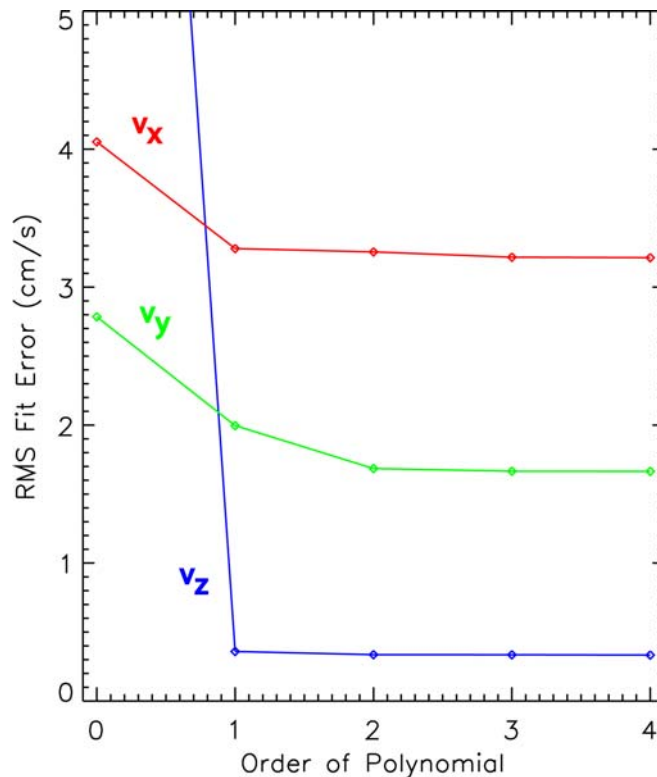


**Figure 24:** The rms fit errors for polynomial fits of given order to the mismatch between accelerometer-derived and the gyroscope-derived velocity components for the IMU in the initial body frame for Data Set C2.

As mentioned previously, the means to completely characterize, and therefore correct for, the drift in the gravitationally-compensated accelerometer components is at our disposal here. However, a simple polynomial characterization of the mismatch appears to be inadequate for the desired level of positional accuracy that we know is achievable (Figure 20). The question then becomes – what processing steps can we take to attain the highest level of positional accuracy?

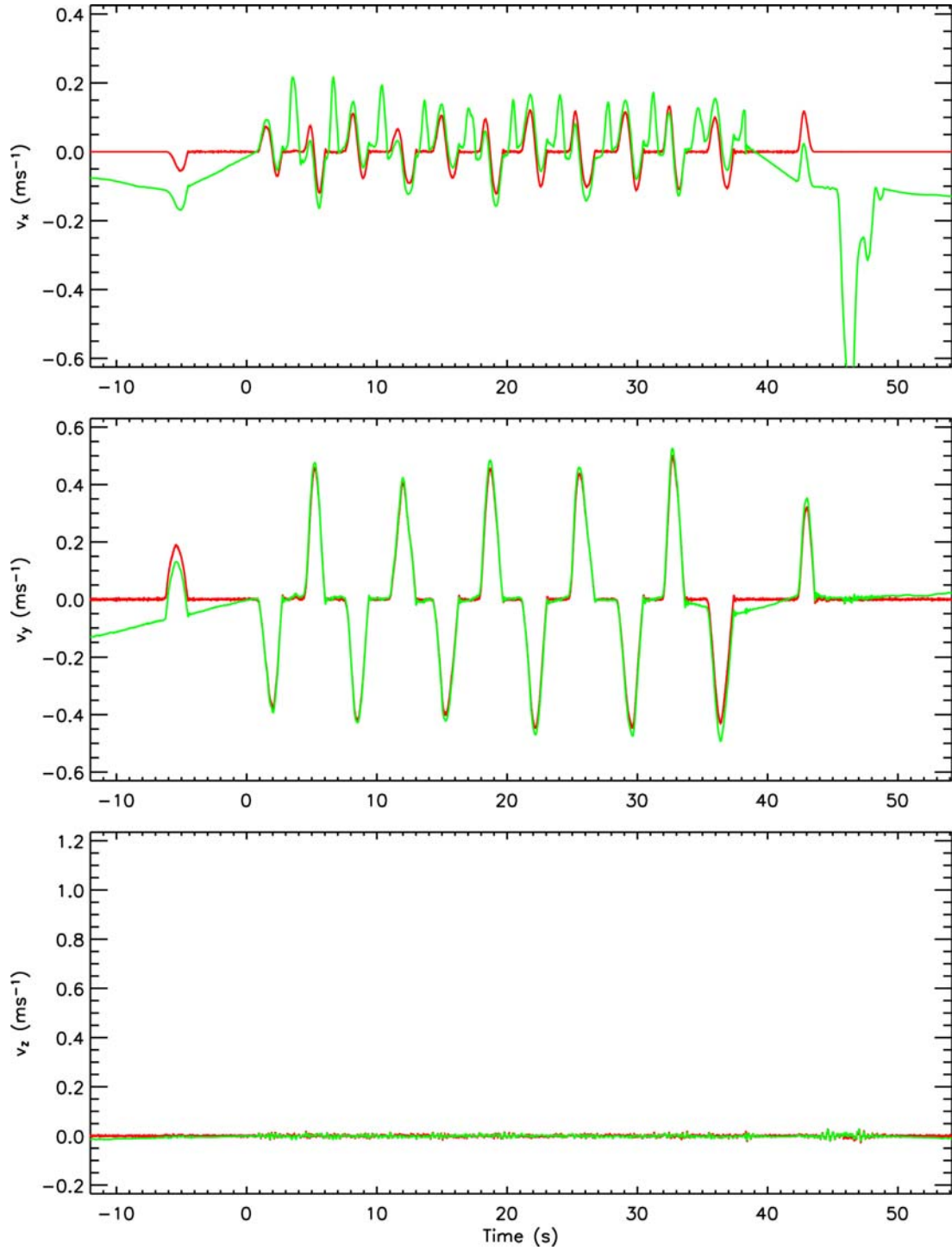


**Figure 25:** The polynomial-corrected accelerometer-derived (green) vs. the gyroscope-derived (red) velocity components for the IMU in the initial body frame for Data Set C2. The polynomials chosen for the corrections are quadratics for all three components (choice based on Figure 24)

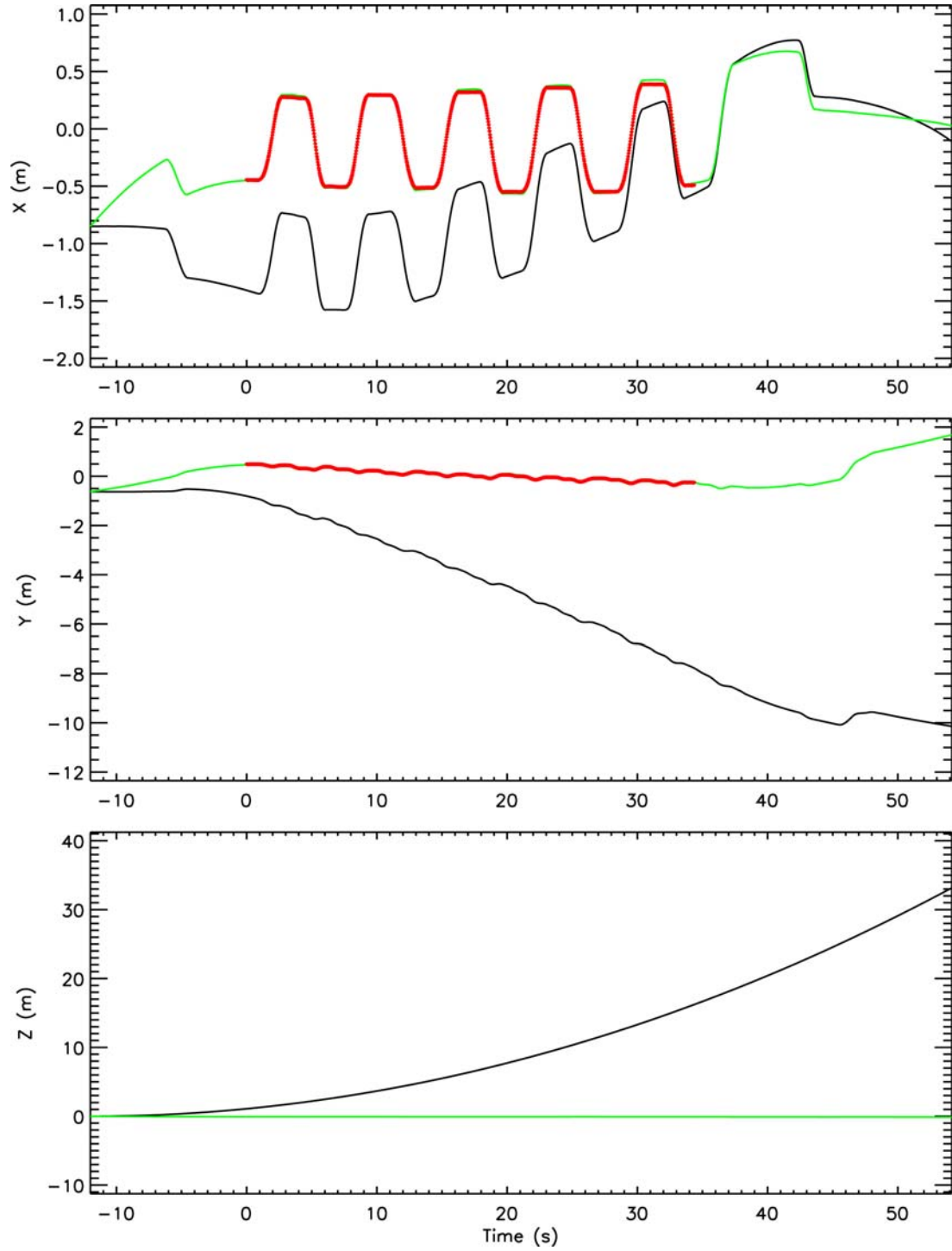


**Figure 26:** The video frame positions obtained by integrating the uncompensated accelerometer-derived velocity components (black) vs. those obtained by integrating the quadratic-corrected accelerometer-derived velocity components (green). The red curves represent the ground truth positions extracted from the video data for Data Set C2.

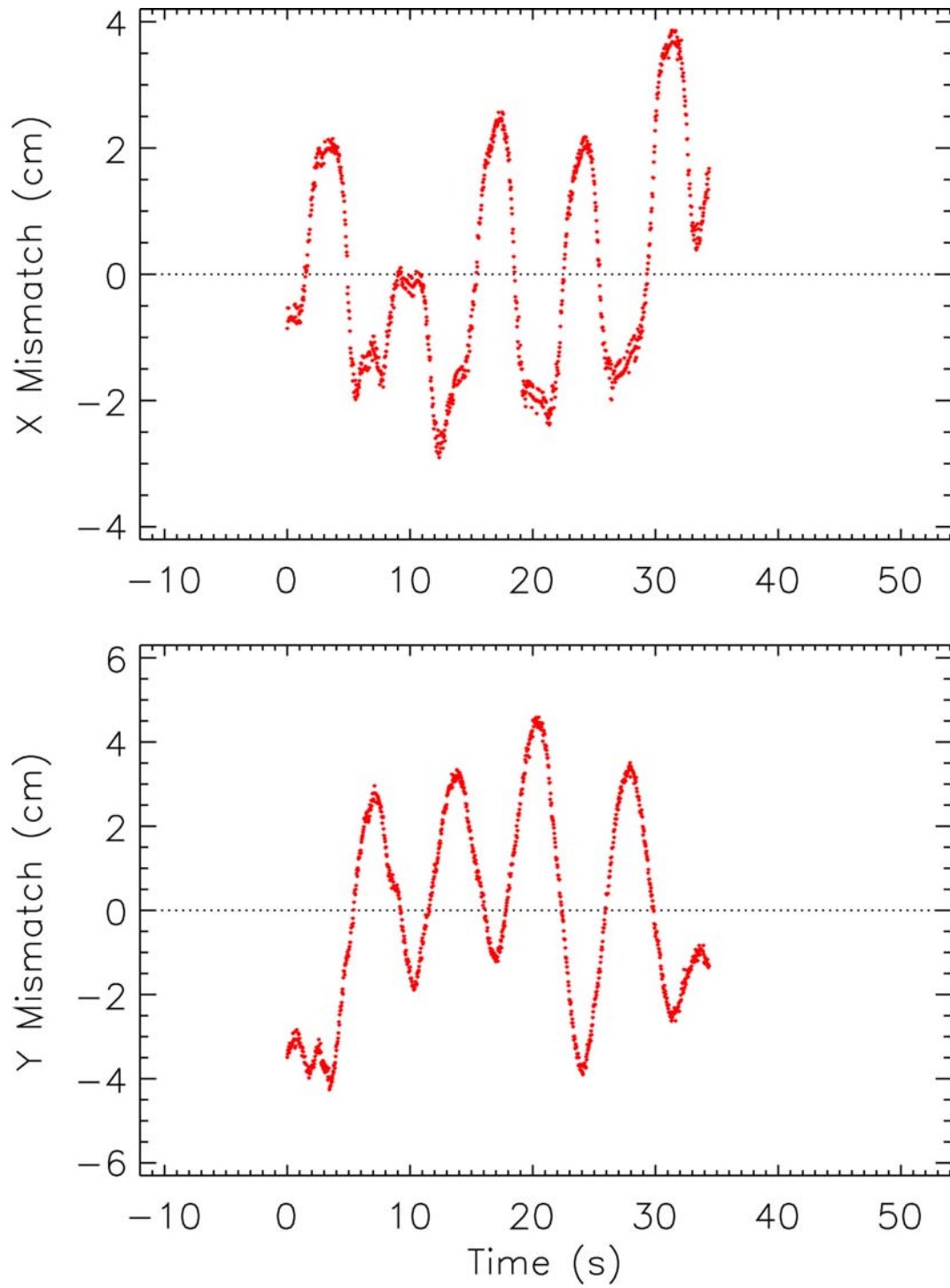


**Figure 27:** The mismatches between the compensated accelerometer-derived and the video ground truth X and Y positions of Figure 26.



### 3.1.2.3. Coupled Rotational and Linear Motion

Data Set E represents the case where the rotational and linear motions of the body are coupled. The  $x$ ,  $y$  and  $z$  IMU accelerometer values for this data set are shown in Figure 29 and Figure 30. In Figure 29, the linear contributions – as computed by (12) via both the IMU acceleration and angular rate values – are over-plotted in red. These clearly show the coupled nature of the motion, where there is now generally poor agreement between the curves. The three other separate contributions to the acceleration components are shown over-plotted in Figure 30. These reaffirm the notion based on Figure 29 that the motion is coupled.

As before, it is instructive to compare the velocity components in the initial body frame as derived by integrating the gravitationally-compensated accelerometer components to those derived using the IMU angular rates via (8). These are respectively represented as the black and red curves of Figure 31. Obviously, the fact that the linear and rotational motions are now coupled makes it much harder to correlate the two curves. However, if we ignore this fact and characterize the mismatch for data based on the previously defined criterion (i.e. the intersection of the data where the red curves of  $v_x$  and  $v_y$  exceed a threshold and are within the time interval of the collected video data) by quadratics again, we obtain the quadratic-corrected accelerometer-derived velocity components represented in Figure 32 by the green curves.

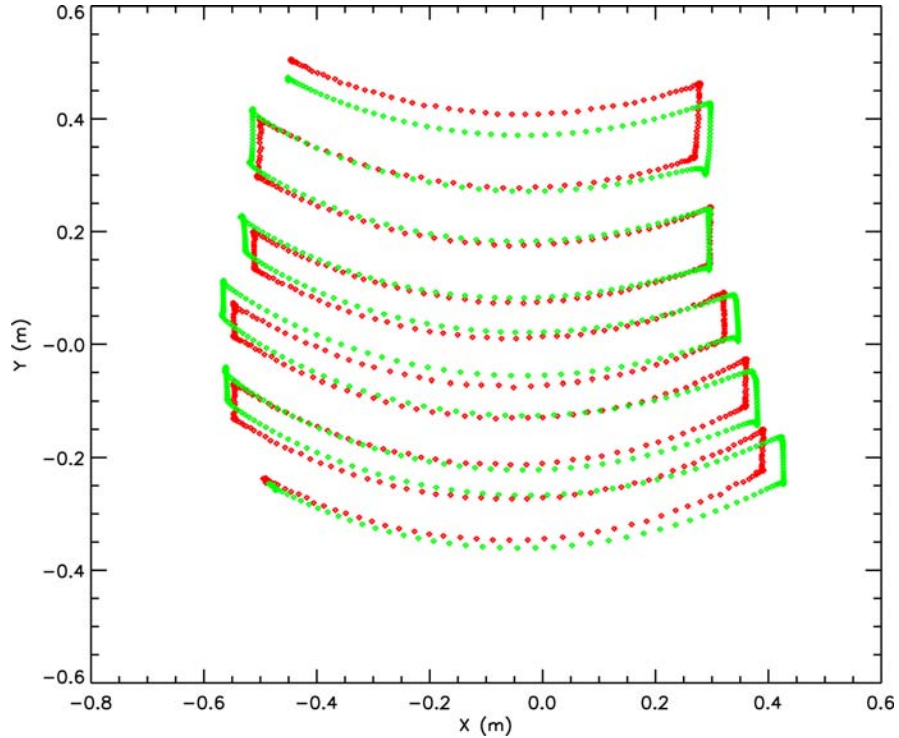


**Figure 28:** The trajectory of sticker 4 based on the ground truth positions extracted from the video data (red) vs. the trajectory obtained by integrating the quadratic-corrected accelerometer-derived velocity components (green) for Data Set C2.

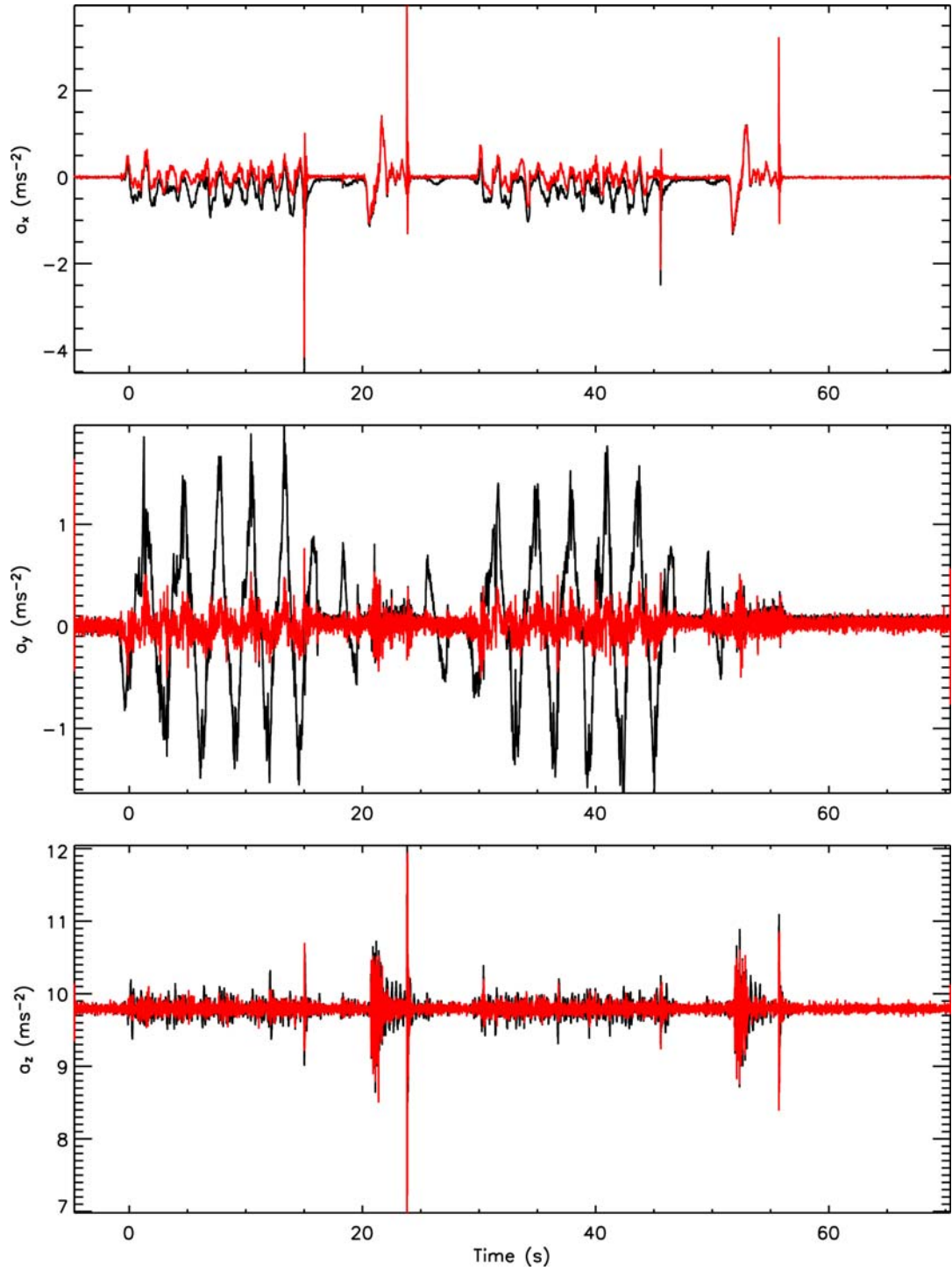


**Figure 29:** Acceleration components as measured via the IMU for Data Set E. The over-plotted red curves represent the linear contribution based on equation (12). Note that the linear contribution is not decoupled from the rotational contribution (cf. with Figure 30).



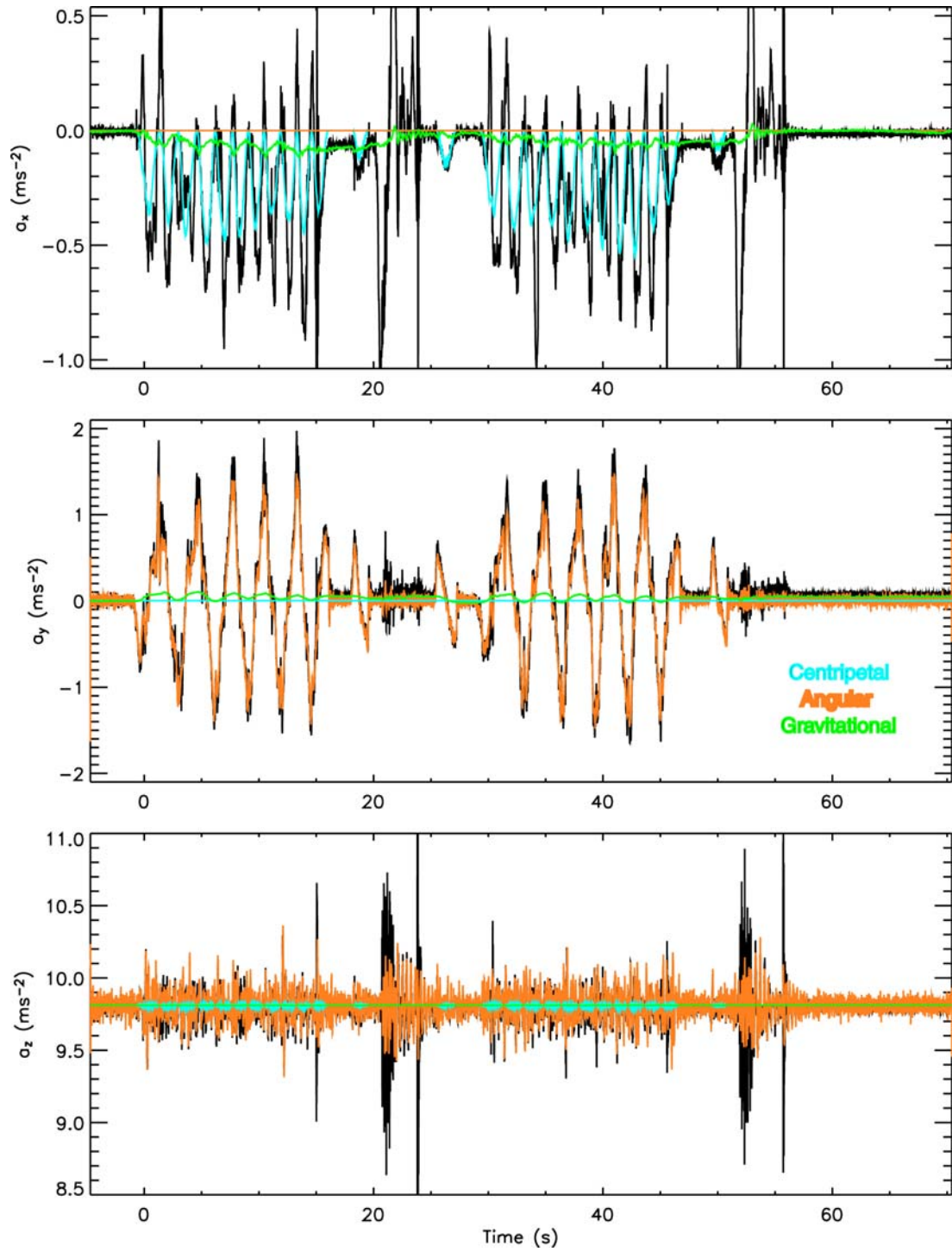


**Figure 30:** Acceleration components as measured via the IMU for Data Set E. The over-plotted colored curves show the respective contributions to the acceleration components.

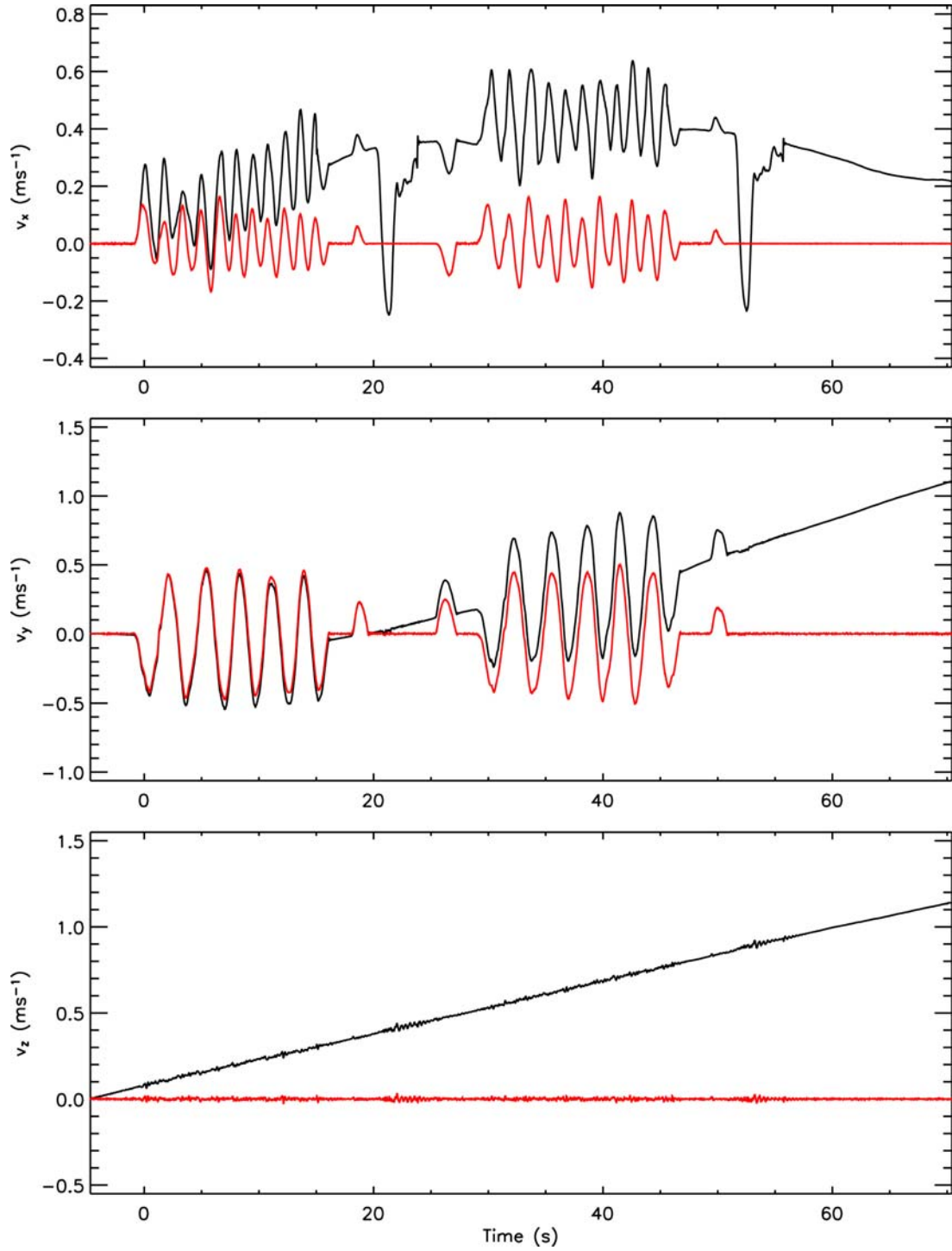


**Figure 31:** The accelerometer-derived (black) vs. the gyroscope-derived (red) velocity components for the IMU in the initial body frame for Data Set E. The gyroscope-derived velocity components neglect the linear contributions to velocity, as a matter of definition, but remain much more stable.

Integrating both the compensated accelerometer-derived velocity components (i.e. the green curves in Figure 32) and the uncompensated accelerometer-derived velocity components (i.e. the black curves in Figure 31), we obtain the results for the  $x$  and  $y$  positions in the video frame shown in Figure 33. The red curve here shows the ground truth positions extracted from the video data for Data Set E. It is obvious from the figure that there is a significant mismatch in the  $y$  position of the video coordinate system, even after the aforementioned compensation. What is interesting though is that the  $y$  position mismatch is to first order linear and is sufficiently characterized by a third order polynomial leading, after the correction process, to cm-scale agreements in positioning demonstrated by Figure 34 and Figure 35.

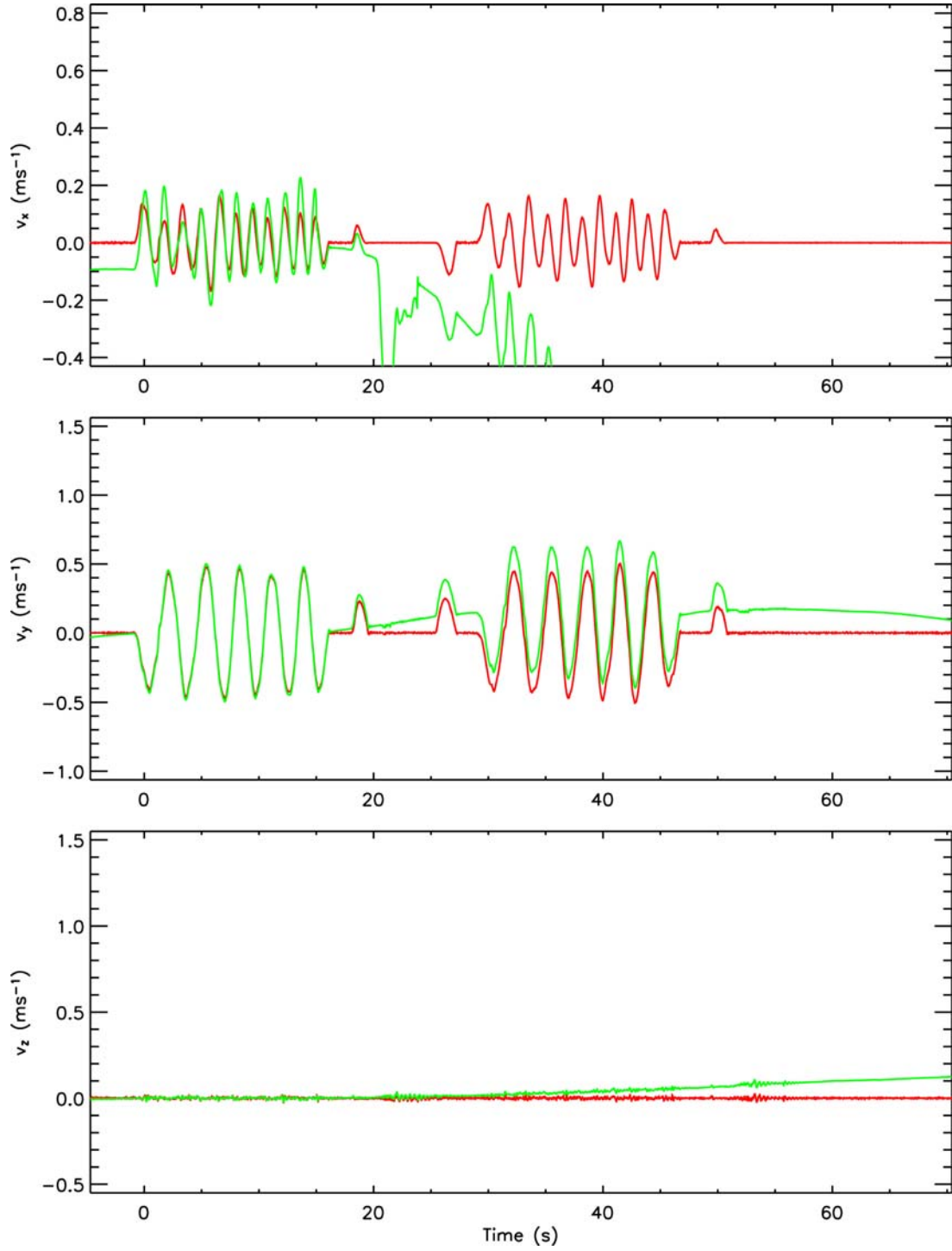


**Figure 32:** The quadratic-corrected accelerometer-derived (green) vs. the gyroscope-derived (red) velocity components for the IMU in the initial body frame for Data Set E. Note that only the IMU data in the time interval of Data Set E (i.e. 0 – 17 s) was chosen for the correction process.

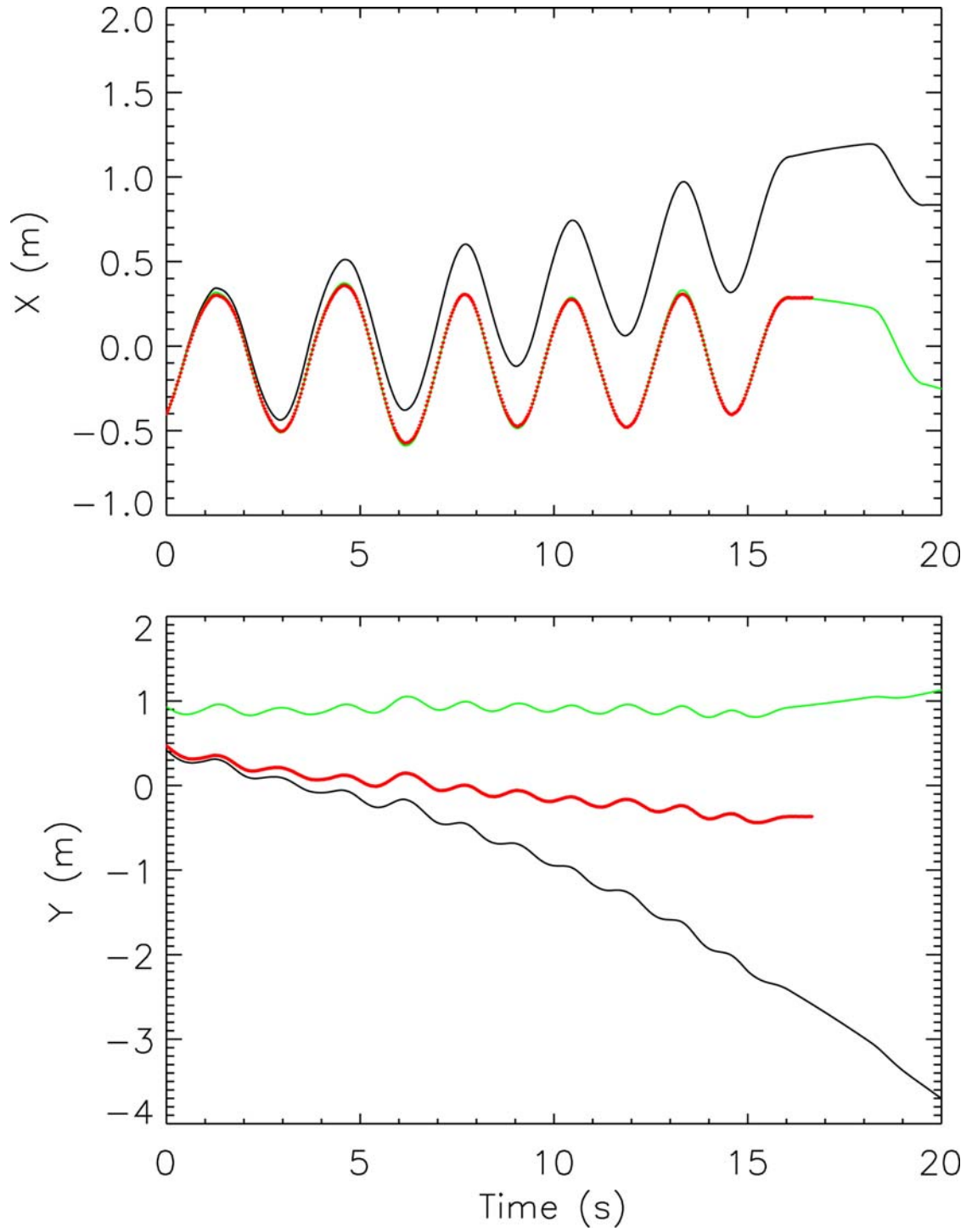


**Figure 33:** The video frame positions obtained by integrating the uncompensated accelerometer-derived velocity components (black) vs. those obtained by integrating the quadratic-corrected accelerometer-derived velocity components (green). The red curves represent the ground truth positions extracted from the video data for Data Set E.

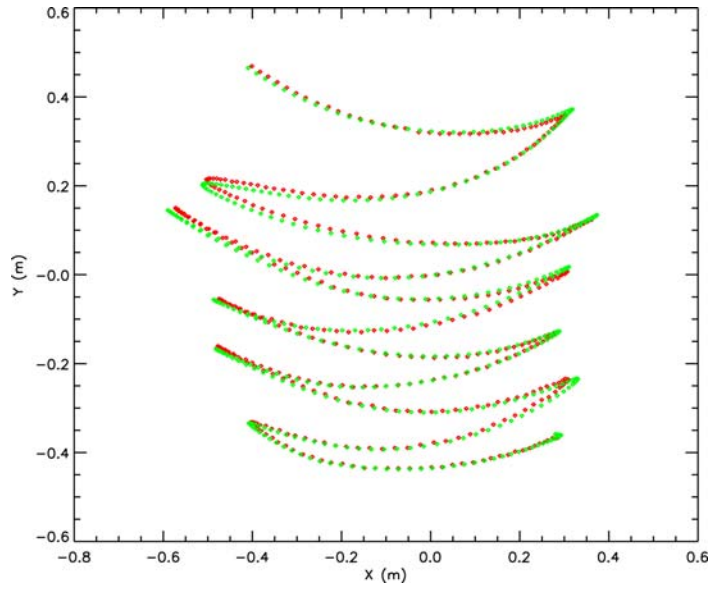


**Figure 34:** The trajectory of sticker 4 based on the ground truth positions extracted from the video data (red) vs. the trajectory obtained by fully compensating as described in the text (green) for Data Set E.

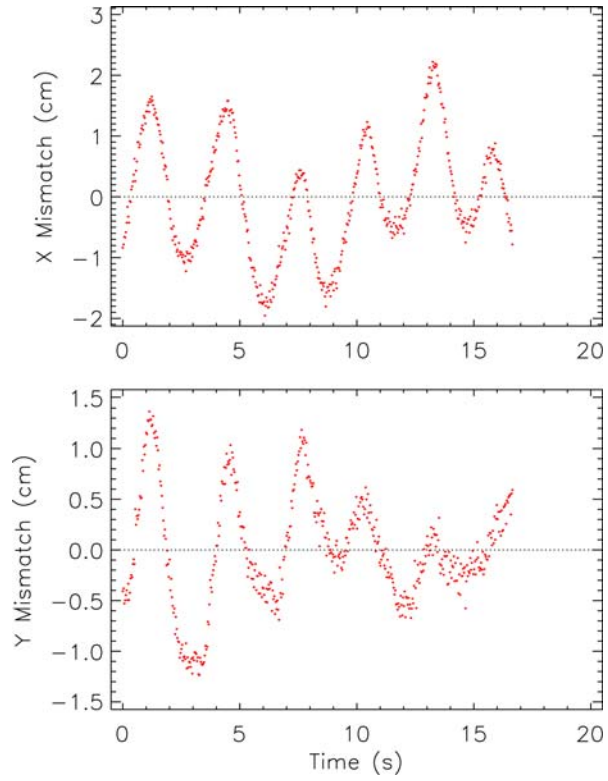


**Figure 35:** The mismatches between the red and green X and Y positions of Figure 34.

### 3.2. Electromagnetic Induction Sensor

As stated in the introduction, the ultimate goal of this project is to develop a handheld sensor that characterizes a target for discrimination as either UXO or clutter, and that does this with a low probability of false alarm. In order to accomplish this, a crucial ingredient is a reliable inversion algorithm that takes the electromagnetic induction (EMI) data and backs out a minimum number of parameters to make the decision. These target-characterizing parameters model the very specific spatial pattern of the EMI data the target produces ([6]–[7]). As a consequence, the inversion – which incorporates this model – requires the data to be spatially well-located for proper characterization. In fact, it was determined in ESTCP Project 200108 (EM61-HH with template) that position accuracies of a couple of cm were required to perform dependable inversions. This was based on the attainment of squared correlations (between the data and the model) greater than 0.99 for compact targets.

#### 3.2.1. Inversion Results

If we take the EMI and compensated IMU-derived trajectory of Figure 33 for Data Set E and carry out the inversion (refer to [6] for specifics), we get the result shown in Figure 36. The resulting target parameters are comparable to those obtained using the ground truth positions extracted from the video data. Both inversion results are presented in Table 3 and Table 4 below.

	$X_o$ (m)	$Y_o$ (m)	$Z_o$ (m)	$\psi_o$ ( $^\circ$ )	$\theta_o$ ( $^\circ$ )	$\phi_o$ ( $^\circ$ )	$R^2$
<b>IMU</b>	-0.076	-0.107	-0.367	0.2	-0.3	111.4	0.989
<b>Video</b>	-0.076	-0.107	-0.354	0.0	-0.5	114.7	0.991

**Table 3:** The target position, orientation and squared correlation inversion results, for the two cases where the IMU-derived trajectory and the video ground truth trajectory were used to position the EMI data of Data Set E.

	<b>Time Gate 1</b>			<b>Time Gate 2</b>			<b>Time Gate 3</b>			<b>Time Gate 4</b>		
	$\beta_x$	$\beta_y$	$\beta_z$	$\beta_x$	$\beta_y$	$\beta_z$	$\beta_x$	$\beta_y$	$\beta_z$	$\beta_x$	$\beta_y$	$\beta_z$
<b>IMU</b>	0.84	0.44	0.18	0.48	0.23	0.09	0.32	0.12	0.03	0.19	0.06	0.02
<b>Video</b>	0.71	0.38	0.19	0.40	0.19	0.09	0.27	0.10	0.04	0.16	0.05	0.02

**Table 4:** The responses (units of  $m^3$ ) that are induced when the primary field is aligned in turn along each of the three principal axes of the target, for each time gate of the EM61-HH.

From Table 3, we see that the squared correlations are on the lower end of the range required for reliable characterization. Although the position and orientation results for the target remained relatively consistent, both fits predicted the target to be a few cm deeper than in reality. The target here is a horizontally emplaced 40 mm projectile 32 cm below the sensor head (refer to Figure 3). In addition, the resulting target response coefficients given in Table 4 (which are strongly correlated with the dimensions of the target, and so should yield  $\beta_y \sim \beta_z$ ) demonstrated much more spread in the transverse components than would normally be desired for reliable



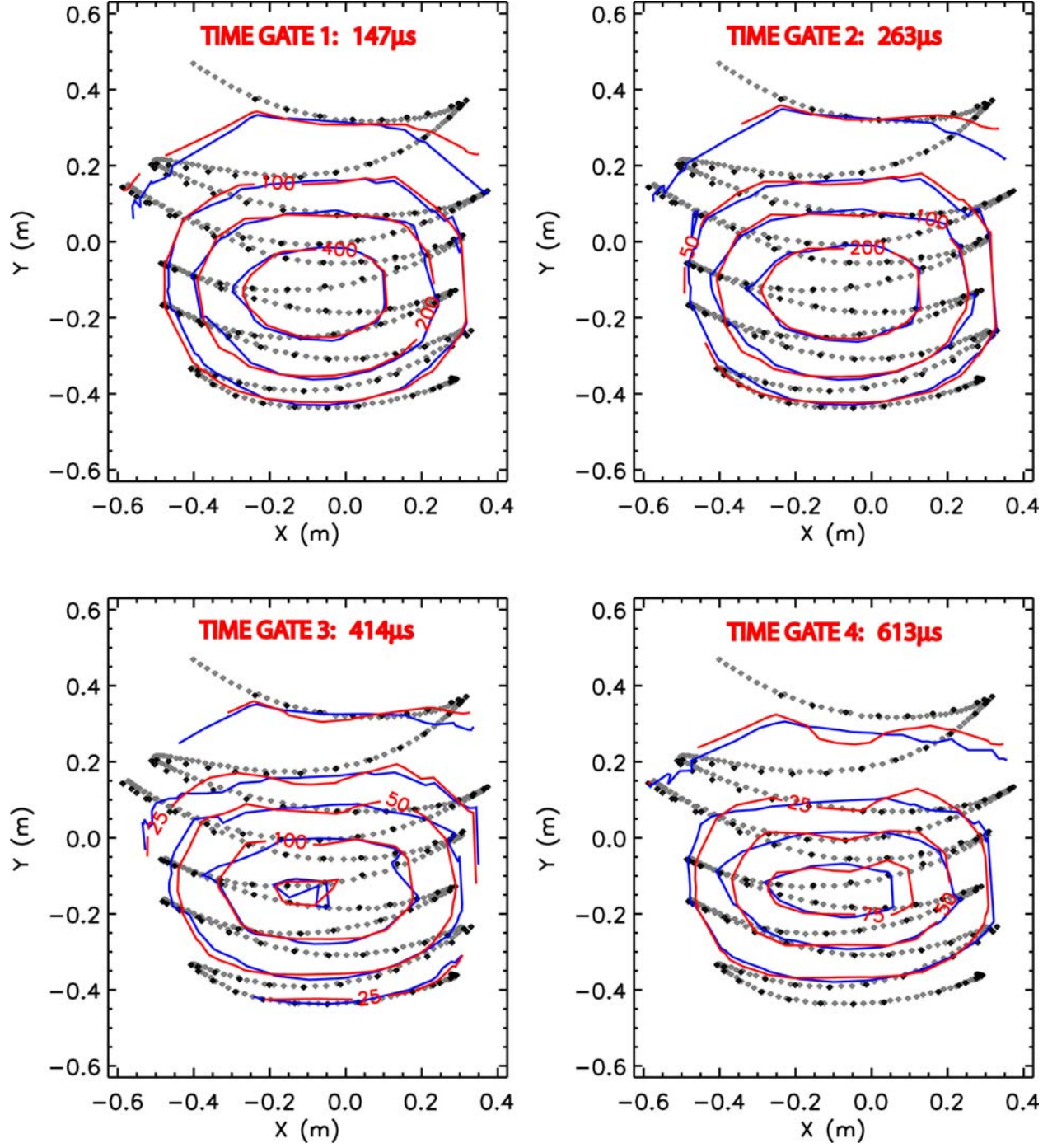


**Figure 36:** Contours of the EM61-HH data (blue curves) vs. those of the model based on the inversion target parameter results (red curves) for Data Set E with the compensated IMU-derived positions (black dots) employed. The grey dots represent the ground truth positions extracted from the video data (for reference).



characterization. Similar disappointing results were observed when inverting the EMI data of Data Set C.

Significantly, both the video ground-truthed and IMU-positioned inversions have fit coherence substantially poorer than typically found with the template data obtained in ESTCP Project 200108. The fit coherence ( $R^2$ ) is the square of the correlation coefficient between the data and the dipole model fit to the data.  $\sqrt{1-R^2}$  is a measure of the mismatch between the model fit and the data. Template data is typically found to have fit coherences of about 0.999. A significant difference between these data and the template data is that these data were obtained in a dynamic environment where the sensor was in motion rather than sitting still on a grid point. This suggests the need for a closer look at the EM61-HH response in a dynamic mode of operation, and incorporating this into our current model. This is treated in the following section.

## 4. EM61-HH Dynamic Response

When sweeping the EM61-HH back and forth over a target, it is noted that the peak response is both delayed and distorted relative to the actual target location. The receiver output of this sensor is analog integrated with a filter that both shifts and distorts the sensor's response. This filter can sufficiently distort signal shape to limit the inversion process. This has a significant impact on the accuracy of target parameter estimates from dipole inversion at sweeping speeds of more than a few cm/sec. At such speeds, it is necessary to account for the sensor's temporal response.

### 4.1. Dynamic Response Characteristics

The manufacturer (Geonics, Ltd.) informed us in private correspondence that EM61-HH system can be represented as an underdamped second-order system given by the standard transfer function of the form

$$(13) \quad H(s) = \frac{\omega_n^2}{s^2 + 2\zeta\omega_n s + \omega_n^2}$$

where  $\omega_n$  is the natural frequency, with  $\omega_n > 0$ ; and  $\zeta$  is the damping factor, with  $0 < \zeta < 1$ . To determine the applicable values for  $\omega_n$  and  $\zeta$  for our sensor, we turned to measurements. Using a small wire coil that switches between high and low impedance as triggered by a pulse generator, the EM61-HH response to a five second on / five second off signal was measured (Figure 37). The analytical expression for the step response of such a system is

$$(14) \quad y(t) = 1 - \frac{e^{-\zeta\omega_n t}}{\sqrt{1-\zeta^2}} \sin(\omega_n \sqrt{1-\zeta^2} t + \cos^{-1}(\zeta))$$

and was found to fit the measured data well with  $\omega_n = 6.2$  and  $\zeta = 0.78$  (Figure 38).

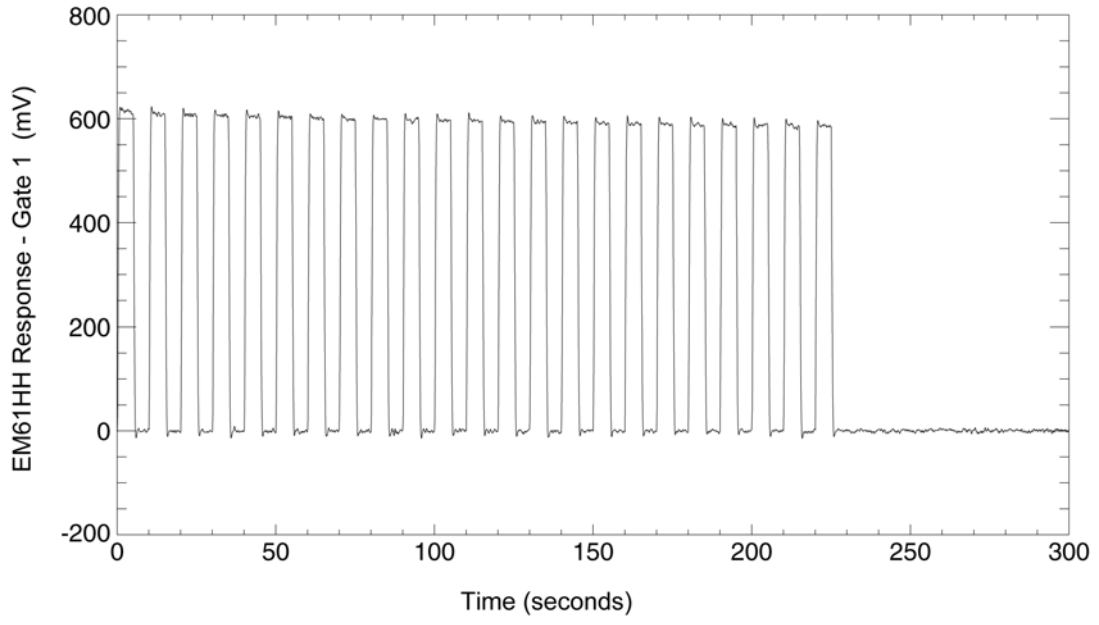


**Figure 37:** The measured EM61-HH response to a sequence of five second on / five second off pulses.

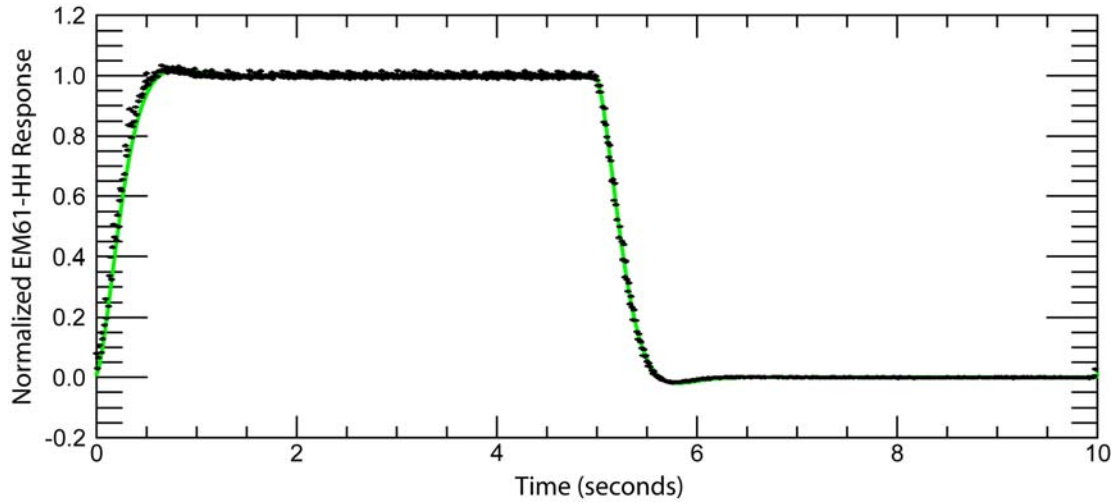


**Figure 38:** The normalized EM61-HH response to a five second on / five second off signal. Data from all the pulses in Figure 20 are used. The green curve represents the best fit to the data using (13) with coefficients  $\omega_n = 6.2$  and  $\zeta = 0.78$ .

## 4.2. EM61-HH Two-Dimensional Sweep Data

The original apparatus used in the 2D data collection process was modified in several ways to minimize any extraneous sources of error.

First, the equipment (i.e. the Crossbow IMU400 and the Geonics EM61-HH system – electronics & data logger included) was attached to a more rigid flat board and allowed to slide on a newly designed, level and stable, platform (Figure 39). The EM61-HH coil head was detached from its pole and placed at one end of the board, while the EM61-HH electronics & data logger along with the IMU, were placed at the other end of the board (Figure 40). As before, movement of the board was constrained to rotate about a pivot point, and the pivot point constrained to translate along a linear groove built into part of the platform, allowing for a variety of simple planar motions containing both translational and rotational contributions. This time, however, the IMU was centered on the pivot point. Again, the video camera was located directly above the platform, pointing downwards.



**Figure 39:** New overall setup for 2D motion measurements

Second, three bright LED's were placed on the EM61-HH coil head to enable the automated extraction of the ground truth positioning information from the video data (Figures 40 and 41). To aid in the latter, a tarp was used to shade the platform and the video camera exposure was adjusted to reduce the background (i.e. non-LED) intensities.

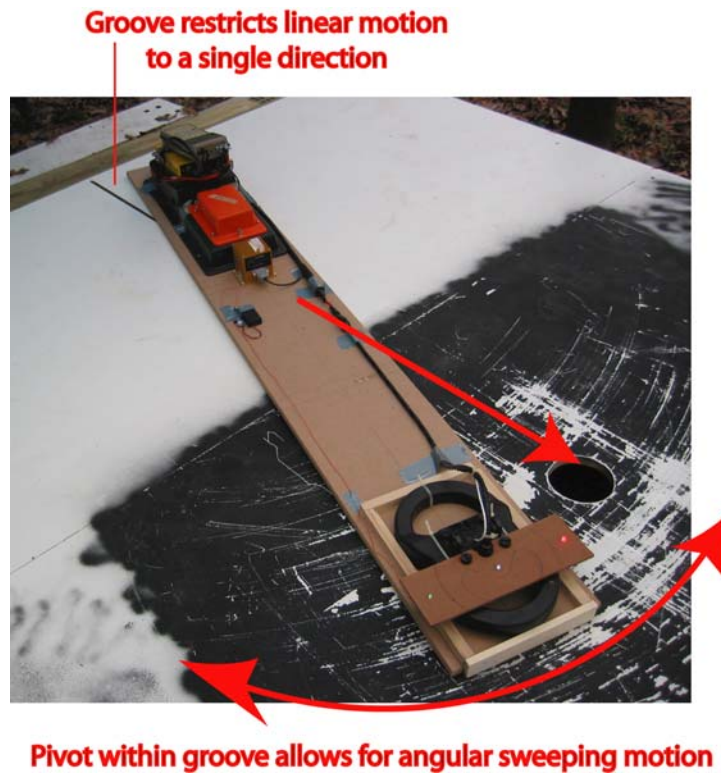


**Figure 40:- Close up of rigid flat board**

Finally, a peg board with holes spaced 1" apart in a regular 2D grid pattern (Figure 41) was imaged by the camera *at the height of the LED's*. This was used to find a polynomial fit that would map camera pixel locations to a calibrated rectangular X-Y coordinate system. The location of each LED was calculated from the centroid of its image over an eight pixel square. When the board was moved quickly (1 m/s), the image of each LED would noticeably smear out. As a sanity check, the separation of the two outer LED's was measured at 25.4 cm and compared to the mapped images. The mean separation noted in the mapped images was 25.3 cm with a standard deviation of 0.2 cm as the board was swept about.

The IMU data was initially collected on an IPAQ PDA (as shown in Figure 40), but the program to do this turned out to be unstable. Instead, a laptop with the GyroView program provided by the manufacturer was used. This meant that a serial cable (from IMU to laptop) had to be carefully dragged around while the board was being moved.

The EMI and IMU data were acquired using independent clocks and then manually synchronized after the fact. In principle, this should introduce one extra unknown representing the relative time lag between the two data streams. However, further complications arose due to limitations associated with the EM61-HH data logger. Specifically, sampling rate stability issues combined with coarse resolution of the data logger clock conspired to blur the true relative time relationship between the two data streams. In order to address this problem, by the summer of 2005, both EMI and IMU data were being collected with a common time stamp on the laptop using a LabView DAQ routine.

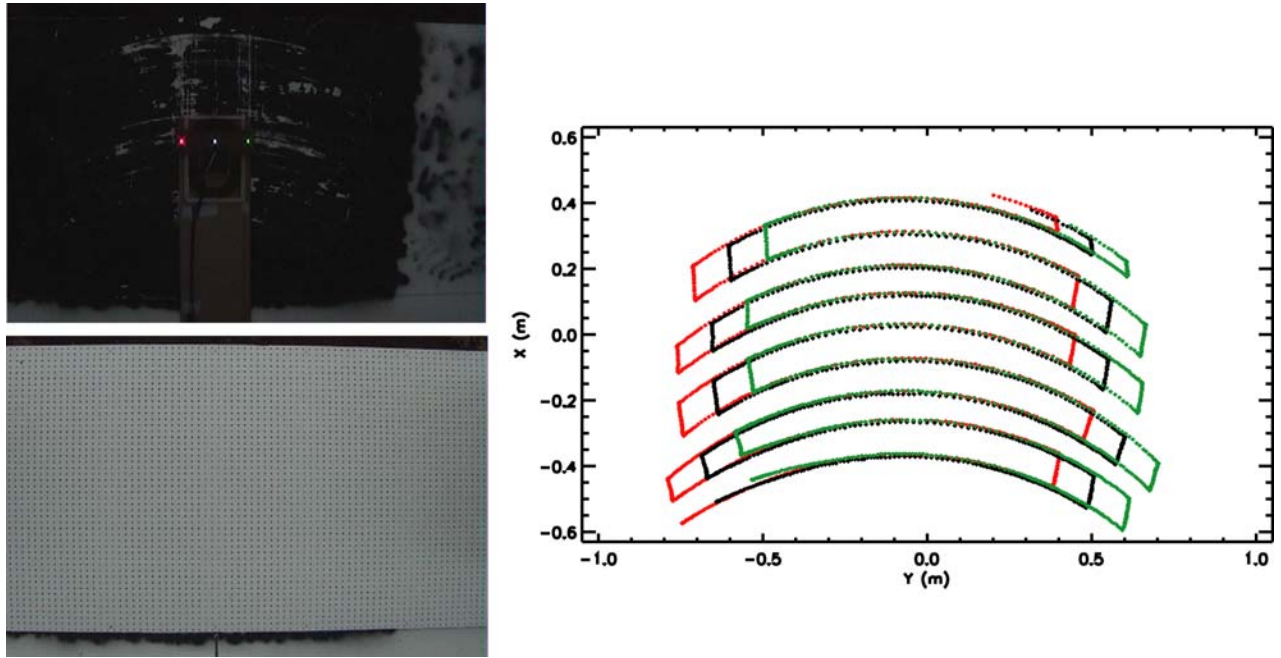


**Figure 41:** Automatic extraction of positioning ground truth from video frame data via intensity threshold using LEDs

### 4.3. Inversion Results

The transfer function with the established values for our sensor was incorporated into the dipole inversion model. Figure 42 shows comparisons of the measured EM61-HH signal during a sweep over a target and dipole fits using the static and the dynamic response models. The data are from three passes near the middle of the sensor trajectory. The dynamic response model clearly does a better job of representing the observed response.

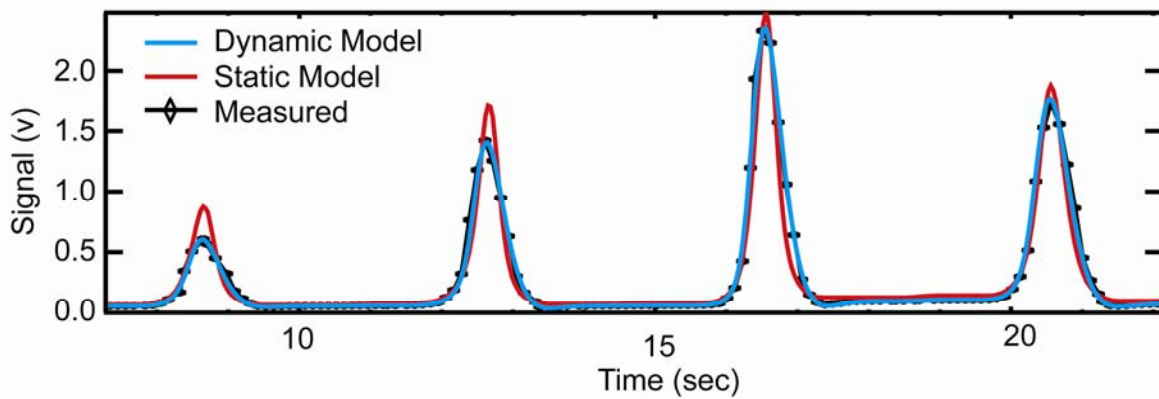


**Figure 42:** Comparison of static and dynamic response models with measured response.

Figure 43 compares inversion results with the static (upper plot) and dynamic (lower plot) response models. The data were collected on a test stand with the EM61-HH swept back and forth over the target. In these figures, the primary (largest)  $\beta$  is plotted along the horizontal axis, and the secondary  $\beta$ s are plotted along the vertical axis, with a symbol at the mean value and a line running between the two. For the test objects (two spheres and two projectiles), the two transverse beta values are expected to be equal. Furthermore, for the two spheres considered, all three betas (i.e. longitudinal and transverse) are expected to be equal. The dotted line represents the line where longitudinal and transverse values are equal. The dynamic model generally produces tighter eigenvalue clusters and better shape characterization (secondary  $\beta$ s more nearly equal) than does the static model.

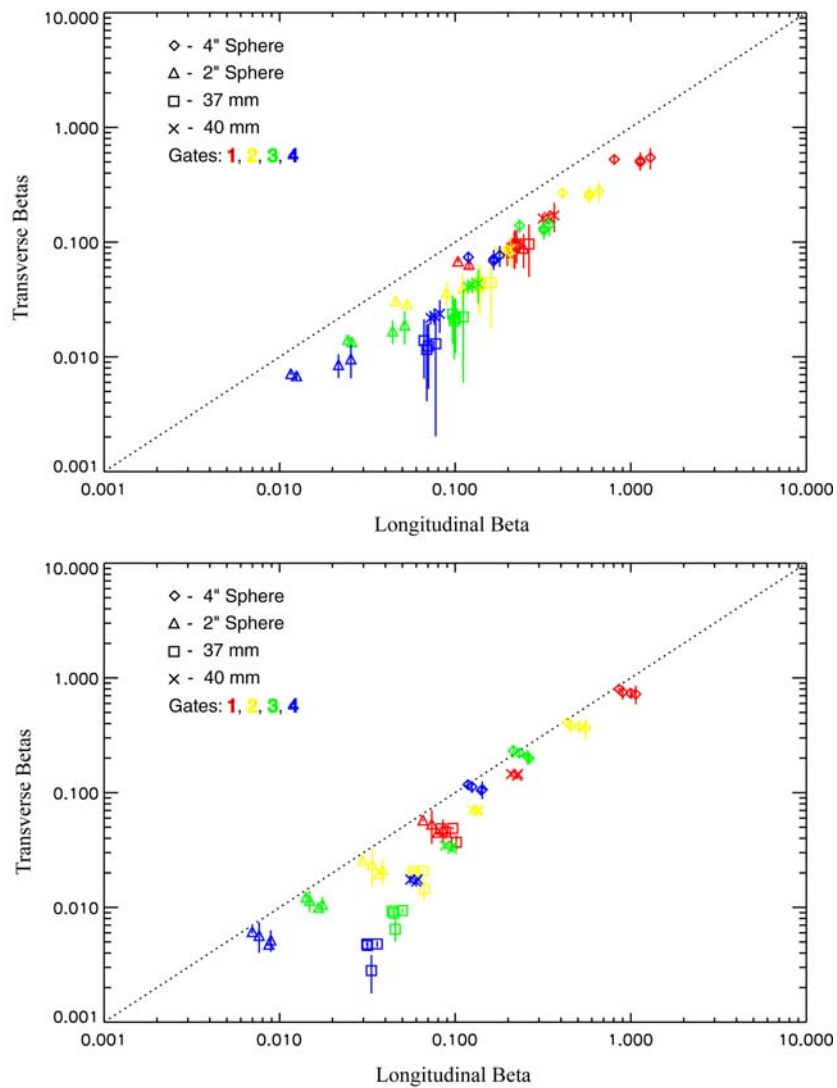


**Figure 43:** Inversion results showing  $\beta$ s when the dynamic response is not taken into account (upper panel) versus when it is taken into account (lower panel).



## 5. Arcsecond Laser-Based Positioning

Position ground truth becomes a significant issue when we consider three-dimensional motion. The video system is only appropriate for 2D motions. A laser positioning system developed by Arcsecond (subsequently acquired by Metris) was adapted for UXO field surveys in ESTCP project MM-0129. Arcsecond refers to their systems as “Indoor-GPS” positioning systems. Much of what they do is used for very precise measurements in manufacturing settings. The system is based on fixed rotating laser transmitters that they liken to GPS satellites. The transmitters have two rotating laser fans that are tilted relative to each other, plus a timing light strobe. By measuring the timing of the two laser fans relative to the timing strobe, one’s relative angular position from a transmitter can be measured. Given a set of two or more transmitters at known locations, all of these angular measurements can be used to calculate one’s position. The ESTCP MM-0129 system makes use of four rigidly attached light sensors in a tetrahedral configuration to measure both the survey platform’s position and orientation. In post-processing software, the displacements from the Arcsecond sensors to the EMI sensor can be used to calculate the 3D position and orientation of the EMI coil. Limited by the laser rotation rate around 40Hz, the position of the platform is measured at a rate of 20 samples per second.

### 5.1. Test Setup

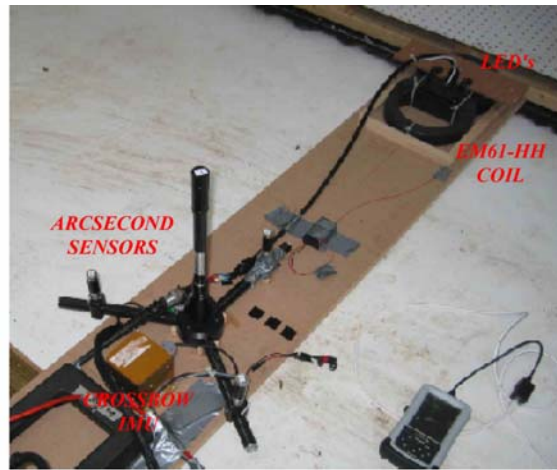
Our testing of the Arcsecond system for this project was reported in [8]. The tests were done on a level wooden platform. Test objects could be placed roughly 30 centimeters below the platform. Photos of the test setups are shown in Figure 44. All of the data presented here is over a four inch diameter carbon steel sphere. The 2D video and 2D Arcsecond position data were collected simultaneously. EM61-HH data was collected directly onto a laptop PC at a rate of 15 samples per second. The PC was also used to collect the Crossbow IMU data.

The 2D tests were done by attaching the equipment to a flat board and sliding the board along the platform surface. The EM61-HH coil head was detached from the usual pole and located at one end of the board. At the other end of the board, the Geonics electronics, the Crossbow IMU, and the Arcsecond sensors were attached (Figure 44a and 44b). As noted previously, the sensor location was tracked using video imaging of LEDs on the coil. The camera frame rate was 30 frames per second.

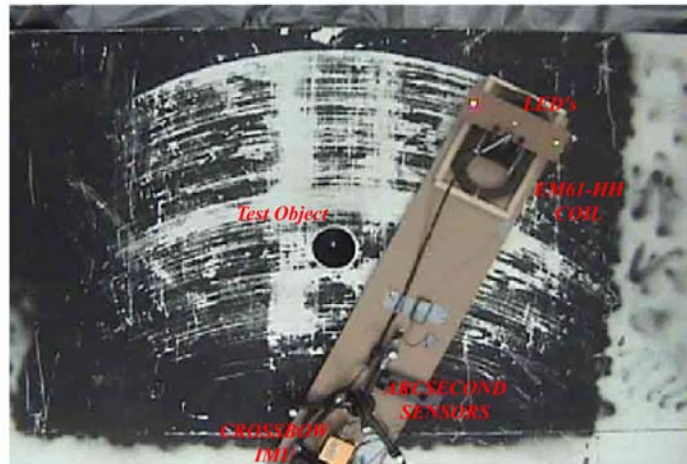
The Arcsecond system used for the 2D tests had a tetrahedral configuration of four sensors attached to the sensor board 75 cm back from the coil. The displacements from each Arcsecond sensor to the EM coil were measured for post-processing the coil’s position. When stationary, the RMS noise in the sensor positions is on the order of 0.2 millimeters and the calculated EM coil position noise is around 0.6 mm. For the 2D tests, only two laser transmitters were used.



(a)



(b)



(c)



**Figure 44:** 2D and 3D EM61-HH sensor positioning experiments. In (a) sideview and (b) video camera view, the 2D sensor board is shown with EM61 coil, LEDs, Arcsecond sensors and Crossbow IMU. In (c) the 3D setup is shown with standard EM61-HH pole, Arcsecond sensors and IMU.

For the 3D test, the EM61-HH coil was reattached to the standard Geonics rig. A flat board and a surveyor pole were attached to the rig to hold both the Crossbow IMU and the Arcsecond sensors. A shoulder strap held the rig over the experimenter's shoulder, and the EM coil could be swept side-to-side in a typical field survey interrogation of an object (see Figure 44c). For each data set, the coil would start flat and be lifted from the test platform for the sweep and placed flat on the platform surface at the end of each sweep.

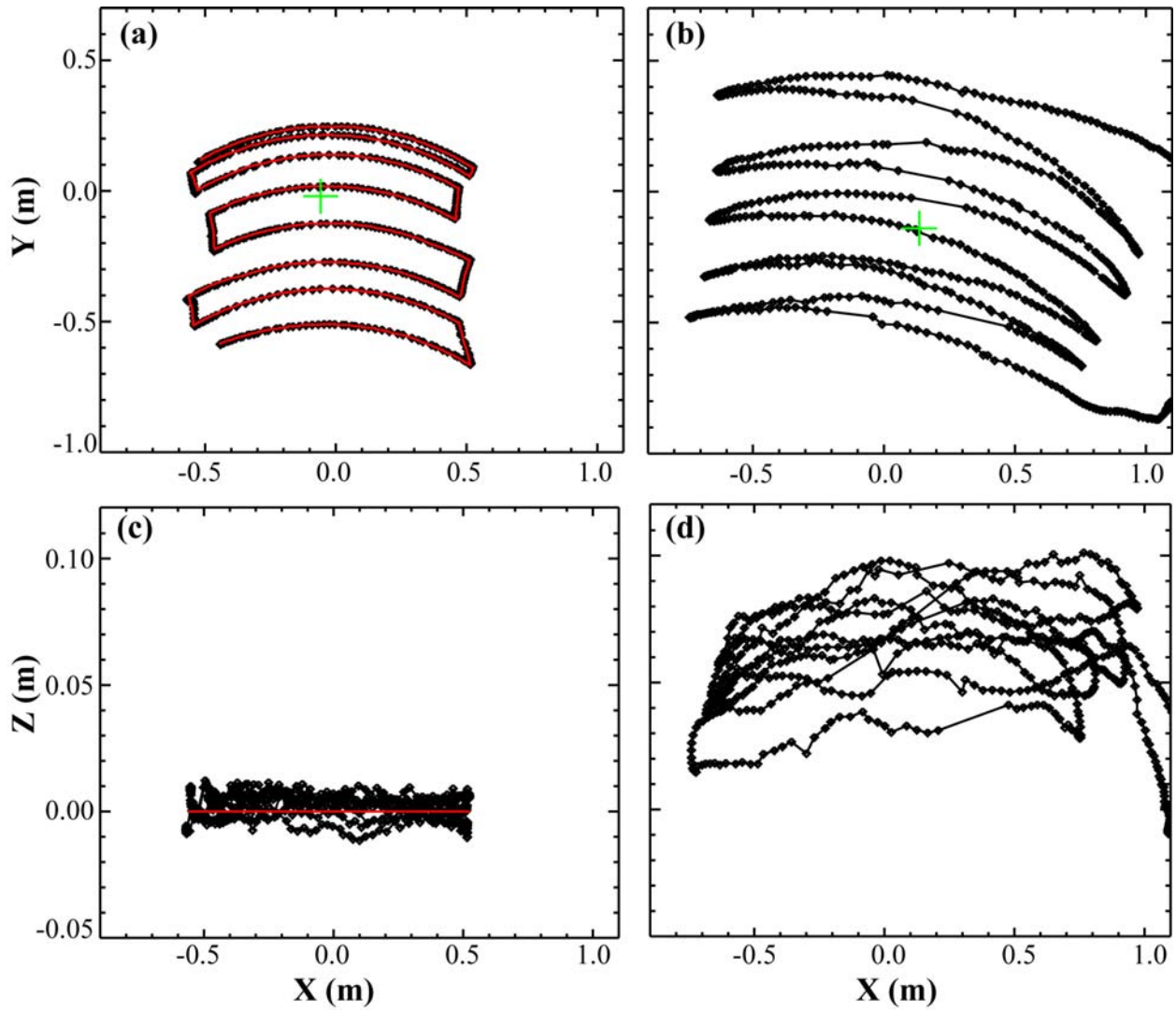
## 5.2. Test Results

Figure 45 plots sample trajectories of the EM coil from the three positioning data sets. An example of the concurrently collected video and Arcsecond positions are shown in 45a and 45c. The video data (red curve) was shifted in X, Y, and time to overlay with the Arcsecond positions. To compare the two sets, the video data was interpolated to the Arcsecond times. Across the central region of the video data, the standard deviations in the differences in X and Y were between 2 and 4 mm. The mean horizontal distance between the two position measurements was 3.5 mm with a standard deviation of 2.3 mm. Larger differences were noted around the edges of the video image. There is a distinct trend to differences at the edge and there maybe a residual error to the applied lens correction. The video data assumes a flat board, but the Arcsecond data in 45c shows almost 2 cm in variation. Along the Y direction, there is a distinct slope to the measured Z on the order of 1.0 cm over a distance of 100 cm. Over a narrow central region of the sweeps, the standard deviation in Z is 2.6 mm. Based on the reasonable agreement between these two systems we conclude that their positioning is probably good to 5 mm or better. Figure 45b and 45d plot a sample 3D trajectory of the EM coil. The measured variation in Z as the coil is lifted and swept side-to-side over the platform is on the order of 10 cm.

The EMI data were fit with the standard induced magnetic dipole response model, including the dynamic response of the EM61-HH. The model parameters are object position ( $x, y, z$ ), object orientation ( $\theta, \phi, \psi$ ), and the object's magnetic polarization responses along its primary axes ( $\beta_1, \beta_2, \beta_3$ ). Because the test object was a sphere, we simplified our fits with a single  $\beta$  value. Another important aspect of the inversion model was accounting for the temporal response of the EM61-HH

Results of fitting the measured data with the different positioning systems are shown in Figures 46 and 47. The black symbol/curves are the measured data and the green curve is the best model fit. In Figure 46, the data is plotted as a function of time. In Figure 47, it is plotted as a function of the X position. Note the displacements in X of the peak signals due to the sensor response; the actual sphere location is between the peaks.

For the 2D video/Arcsecond data, the measurements over the sphere were repeated and inverted seven times. For the 3D data, seventeen sets of measurements were made. Figure 48 presents the



**Figure 45:** Sample X-Y and X-Z plots of the EM61-HH coil trajectories. In (a) and (c), the 2D coil motion on the sensor board as measured by the Arcsecond (black symbols) and the video (red curve). In (b) and (d), the 3D motion of the coil on the standard EM61-HH pole. The green symbol is the object location.

inversion results for all of this data (red X - video fit, green triangle – 2D Arcsecond, black diamond – 3D Arcsecond).

The fitted depths and response  $\beta$ 's are plotted in the top panel of Figure 48. These two fit parameters are highly correlated in the inversion model. Given measurements with both signal noise and positioning error, the inversion model tends to vary these two parameters the most in an attempt to get the best model fit to the data. For the three positioning sets, the mean sphere  $\beta$ 's are: 6.70 – 2D Arcsecond, 6.88 – 2D video, and 6.94 – 3D Arcsecond. The standard deviations are: 0.18, 0.14, and 0.27, respectively. The sphere's depth was not noted accurately enough to check on the fitted

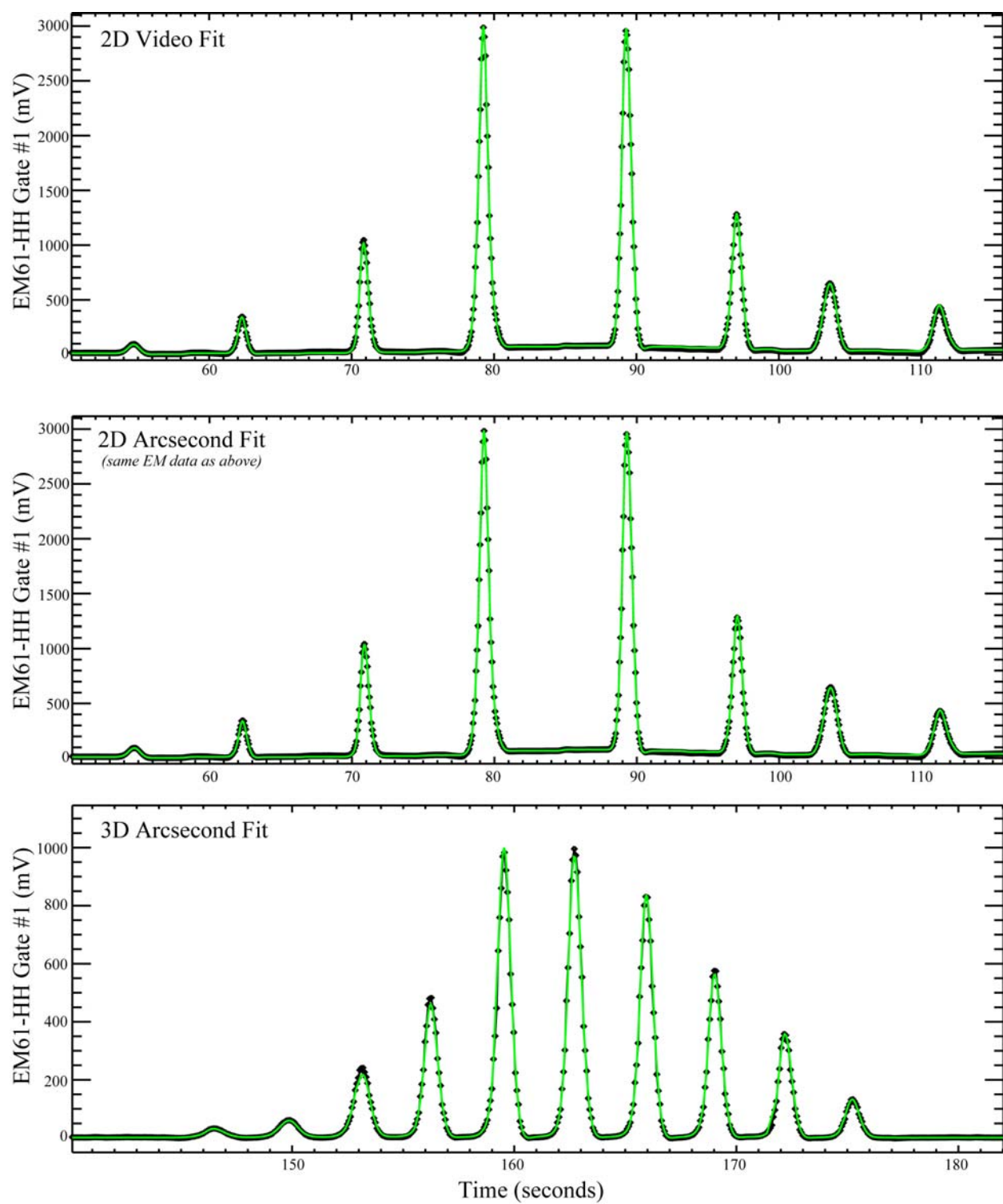


**Figure 46:** Time rasters of EM61-HH data (black curve and symbols) fitted to model (green curve).

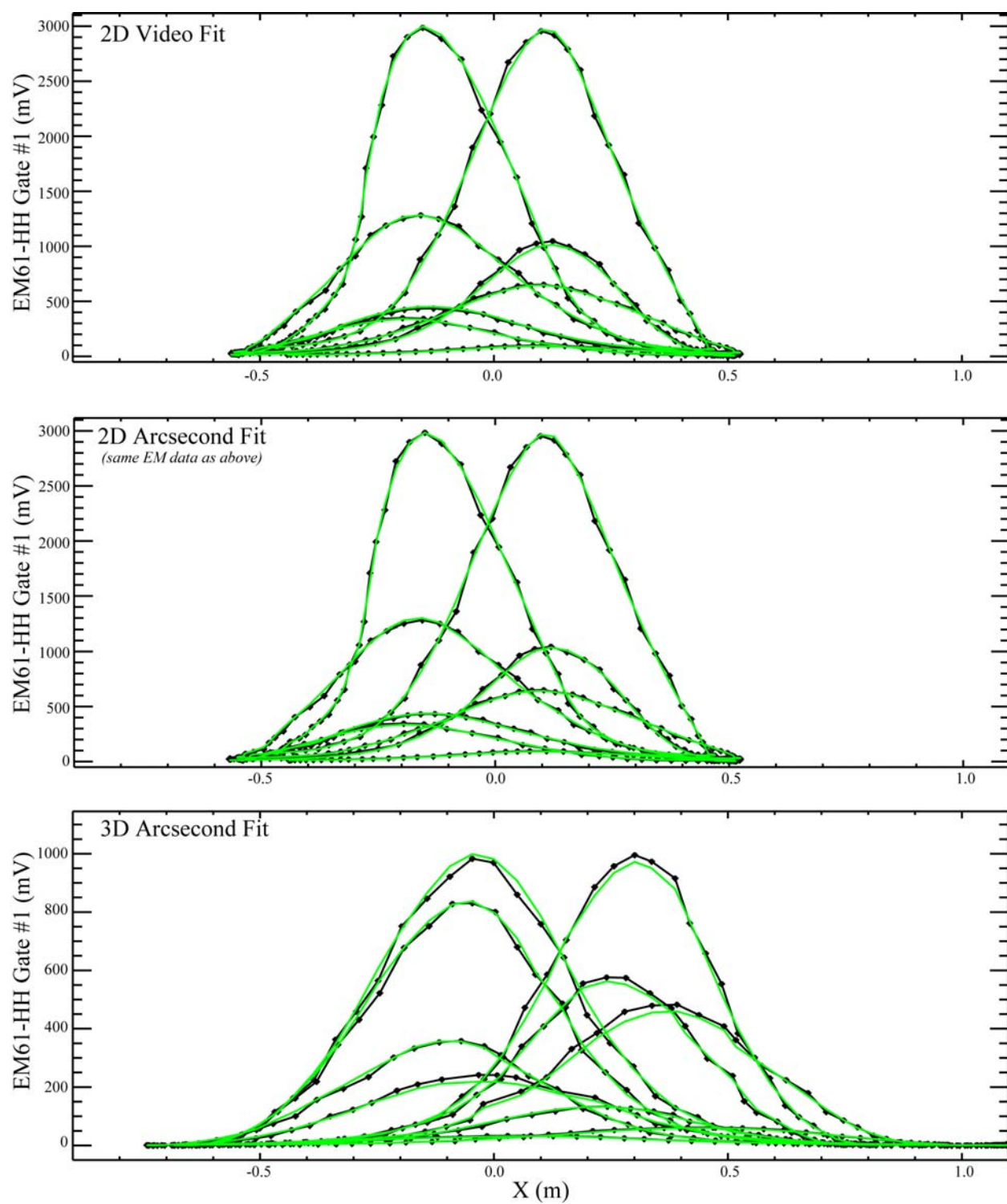


**Figure 47:** Plots along X of EM61-HH data (black curve and symbols) fitted to model (green curve).



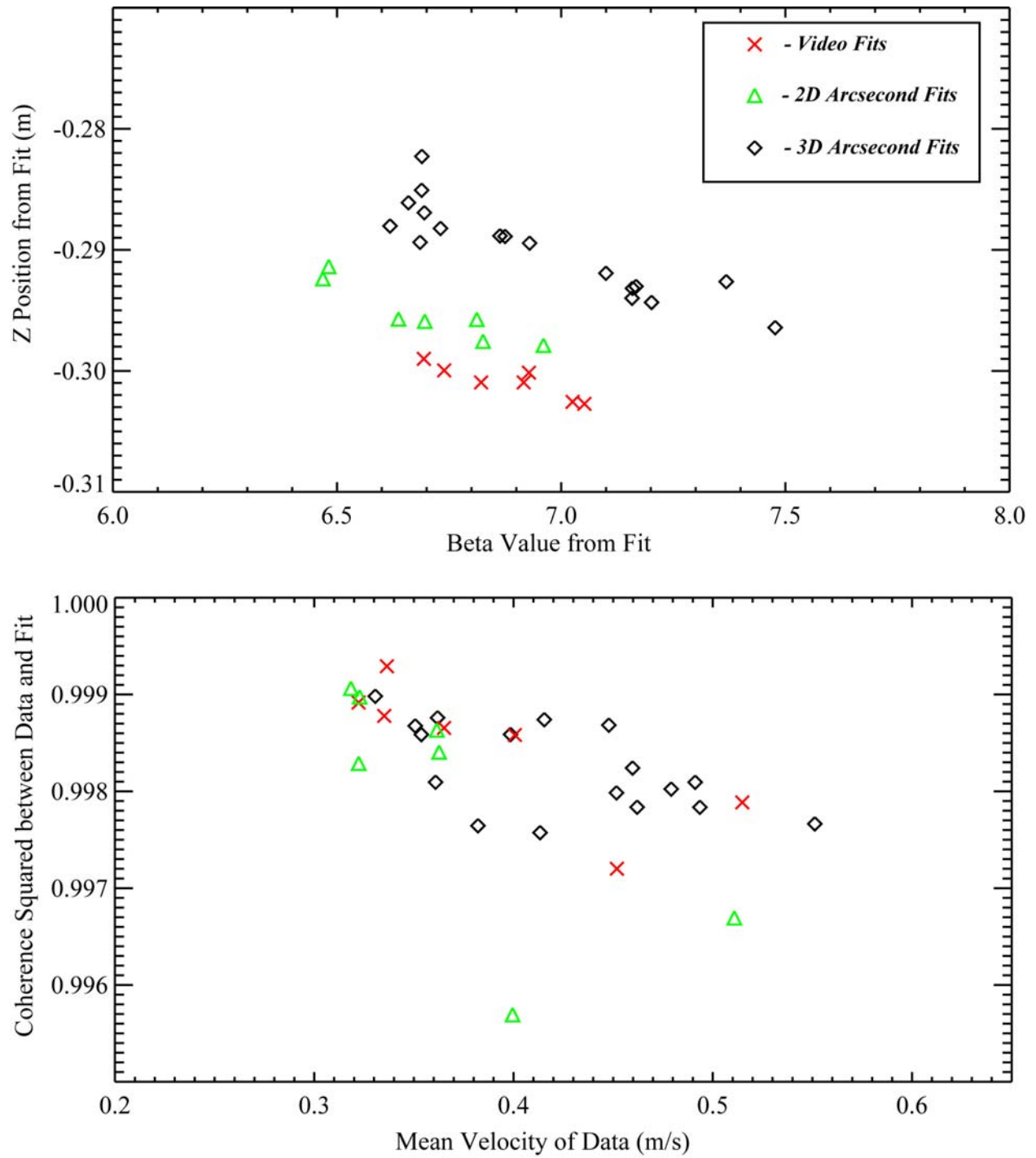


**Figure 48:** Results of fitting EM61-HH data with model using different positioning data.

depths. It was roughly 29 cm below the center of the EM coil when it was resting flat on the platform. For the three coordinate systems,  $z = 0$  was only roughly matched to this coil height.

In the lower panel of Figure 48, a measure of the fit quality is plotted versus the average swing speed of the EM61-HH coil. The peak speeds were on the order of 2 to 3 times greater. The fit quality parameter is the square of the coherence between the best model fit and the data. There is a clear trend to poorer fits as the coil velocity increases. This is not surprising given the positioning system limitations of video frame rate (30 fps) and laser rotation rate (40Hz). At a speed of 1 m/s, the coil has moved 3.3 cm in a video frame and 2.5 cm during a single laser spin. Man portable survey systems move at comparable speeds and vehicle survey platforms exceed it.

In an effort to simulate the error in inverting the polarization responses as a function of positioning errors, a simple Monte Carlo simulation was run. Static measurements on a fixed grid with exact positioning were taken over a 40mm projectile. The data were inverted for the  $\beta$  responses. The same data was inverted repeatedly with increasing random errors added to the known grid positions. The results are displayed in Figure 49, which shows the variability in the fitted polarization responses versus RMS position error in the top panel and the coherence squared of the fit the lower panel. At the level of 3 mm RMS position error, the average fit quality is about 0.998 and the spread in primary response is 15%. This is consistent with the Arcsecond 3D fits having an average fit quality of 0.9982 and a  $\beta$  spread of 13% ( $\sim 0.9/6.94$ ).

To summarize, in the 2D tests, the positions mapped were found to match video mapped images at RMS position differences of 3-4 mm. Inverted 2D and 3D positioned data had high fit qualities of 0.9982. The fitted magnetic polarization responses had a narrow range of values (13%) over a set of seventeen 3D measurements of a steel sphere. However, the fit quality decreased at faster sensor motion rates, indicating larger positioning errors as speeds approach 1 m/s. Simulations of EMI data inversion with randomized position errors came up with similar fit qualities and response parameter errors at an RMS position error level of 3mm. All indications are that this laser based system is tracking the EMI sensor with sub-centimeter accuracy, and is suitable for ground-truthing 3D IMU position data.

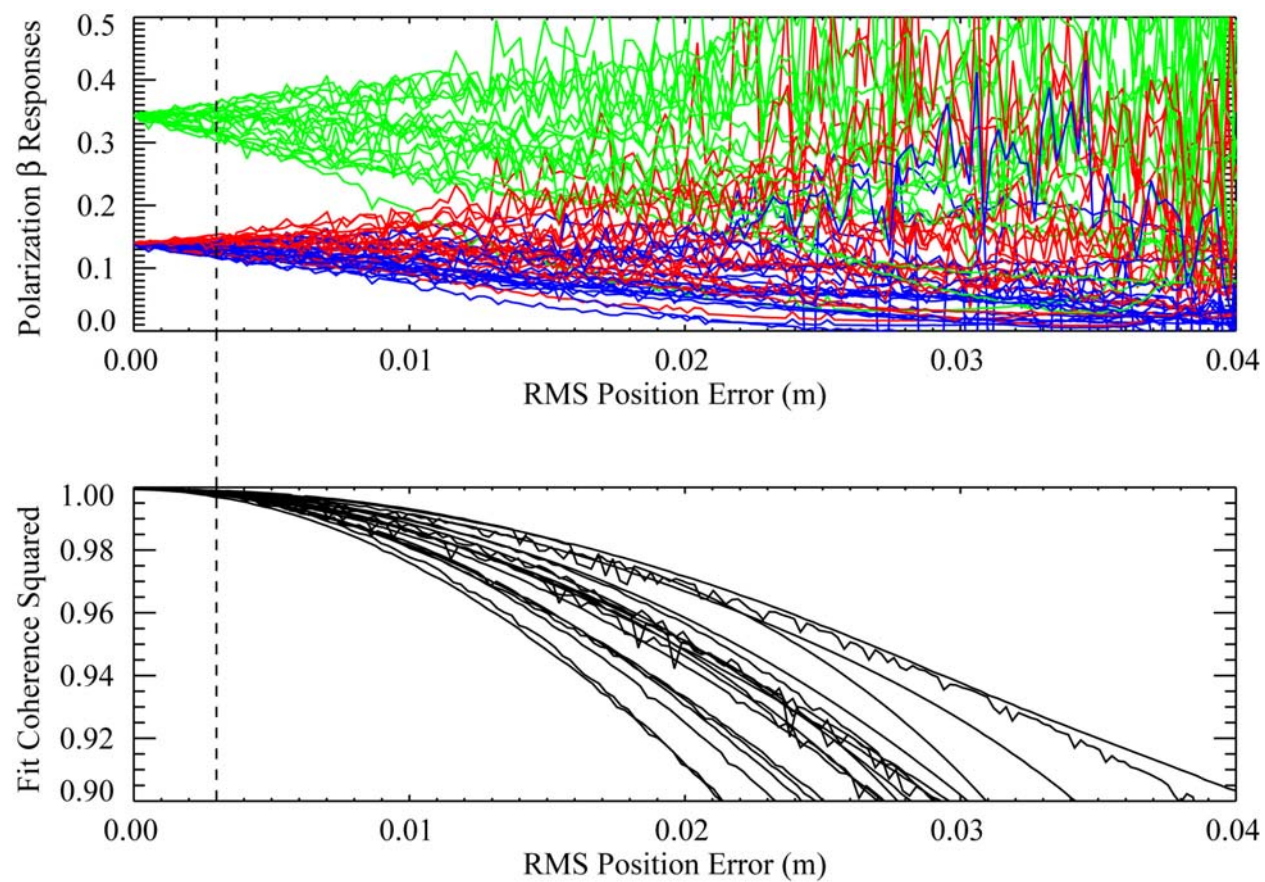


**Figure 49:** Monte Carlo simulation of inverting 40mm projectile data with randomly generated position errors. Dashed line at RMS position error of 3 mm with an average fit coherence of 0.998 and a primary  $b$  spread of 15% (0.05/0.34).



## 6. Three Dimensional Motion

With general three-dimensional motions it is necessary to have some sort of external aid in order to properly compensate the IMU measured quantities and bound the random walk errors. This may involve either deploying additional sensors to get periodic independent confirmation of the true or derived quantities, or periodically forcing the IMU to be in situations where the true or derived quantities are known. The simplest scheme is one where zero velocity updates are periodically taken.

### 6.1. Zero Velocity Update Method

The quantities measured by the IMU are the angular rate vector,  $\tilde{\boldsymbol{\omega}}$ , and the acceleration vector,  $\tilde{\mathbf{a}}$ . The angular rate can be expressed in the IMU body frame of reference as

$$(15) \quad \tilde{\boldsymbol{\omega}}(t) = \mathbf{s}_{\boldsymbol{\omega}} \cdot \boldsymbol{\omega}(t) + \mathbf{b}_{\boldsymbol{\omega}}(t) + \mathbf{n}_{\boldsymbol{\omega}}(t)$$

where  $\boldsymbol{\omega}(t)$  represents the true angular rate vector;  $\mathbf{b}_{\boldsymbol{\omega}}(t)$  and  $\mathbf{n}_{\boldsymbol{\omega}}(t)$  represent, respectively, the bias and zero-mean noise vectors in the angular rate measurements. A constant calibration scale factor  $\mathbf{s}_{\boldsymbol{\omega}}$  is included for generality. Comparisons with ground truth showed that the calibration factor can be set to 1 for our application. The acceleration vector is

$$(16) \quad \tilde{\mathbf{a}}(t) = \mathbf{s}_{\mathbf{a}} \cdot \mathbf{a}(t) + \mathbf{R}_{e \rightarrow b}(t) \mathbf{g} + \mathbf{b}_{\mathbf{a}}(t) + \mathbf{n}_{\mathbf{a}}(t)$$

where  $\mathbf{a}(t)$  represents the true acceleration vector, free of the influence of gravity.  $\mathbf{b}_{\mathbf{a}}(t)$  and  $\mathbf{n}_{\mathbf{a}}(t)$  represent, respectively, the bias and zero-mean noise vectors in the acceleration measurements; and  $\mathbf{s}_{\mathbf{a}}$  represents a calibration scale factor vector, equal to 1 for our application.  $\mathbf{R}_{e \rightarrow b}(t)$  is the rotation matrix that transforms earth's gravitational acceleration vector  $\mathbf{g}$  from the earth-fixed frame to the IMU body frame at time  $t$ .

$$(17) \quad \mathbf{R}_{e \rightarrow b}(t) \equiv \begin{bmatrix} \cos\psi(t)\cos\theta(t) & \sin\psi(t)\cos\theta(t) & -\sin\theta(t) \\ -\sin\psi(t)\cos\phi(t) + \cos\psi(t)\sin\theta(t)\sin\phi(t) & \cos\psi(t)\cos\phi(t) + \sin\psi(t)\sin\theta(t)\sin\phi(t) & \cos\theta(t)\sin\phi(t) \\ \sin\psi(t)\sin\phi(t) + \cos\psi(t)\sin\theta(t)\cos\phi(t) & -\cos\psi(t)\sin\phi(t) + \sin\psi(t)\sin\theta(t)\cos\phi(t) & \cos\theta(t)\cos\phi(t) \end{bmatrix}$$

where  $\psi(t)$ ,  $\theta(t)$  and  $\phi(t)$  are the yaw, pitch and roll angles, respectively (see Appendix A). Hence

$$(18) \quad \mathbf{R}_{e \rightarrow b}(t) \mathbf{g} = \mathbf{R}_{e \rightarrow b}(t) \begin{bmatrix} 0 \\ 0 \\ g \end{bmatrix} = \begin{bmatrix} -\sin\theta(t) \\ \cos\theta(t)\sin\phi(t) \\ \cos\theta(t)\cos\phi(t) \end{bmatrix} g$$

The trajectory of a moving IMU body in the local earth-fixed frame is determined by isolating the true acceleration vector  $\mathbf{a}(t)$  of (16) and transforming this to the local earth-fixed frame, before integrating the quantity twice - once to obtain the velocity vector, and a second time to

obtain the position vector. The task of isolating  $\mathbf{a}(t)$  from the measured acceleration vector, however, demands an accurate instantaneous accounting of both the gravitational contribution to acceleration and the bias vector, as well as knowledge of the scale factor vector.

In order to properly account for the gravitational contribution to acceleration, the evolving orientation of the IMU body frame relative to the earth-fixed frame is necessary. The orientation time series is computed by integrating the true angular rate vector  $\boldsymbol{\omega}(t)$  of (15) to obtain the Euler yaw, pitch and roll angles. Repeating (4), this represents solving a set of coupled differential equations

$$(19) \quad \frac{d}{dt} \begin{bmatrix} \phi(t) \\ \theta(t) \\ \psi(t) \end{bmatrix} \equiv \begin{bmatrix} 1 & \sin \phi(t) \tan \theta(t) & \cos \phi(t) \tan \theta(t) \\ 0 & \cos \phi(t) & -\sin \phi(t) \\ 0 & \frac{\sin \phi(t)}{\cos \theta(t)} & \frac{\cos \phi(t)}{\cos \theta(t)} \end{bmatrix} \begin{bmatrix} \omega_x(t) \\ \omega_y(t) \\ \omega_z(t) \end{bmatrix}$$

where  $\psi(t)$ ,  $\theta(t)$  and  $\phi(t)$  are the yaw, pitch and roll angles, respectively.

As with the acceleration vector, the task of isolating  $\boldsymbol{\omega}(t)$  from the measured angular rate vector also demands an accurate instantaneous accounting of the bias vector, as well as knowledge of the scale factor vector.

It should be pointed out that even if one were able to perfectly compensate for  $\mathbf{s}_\omega$ ,  $\mathbf{b}_\omega(t)$ ,  $\mathbf{s}_a$ ,  $\mathbf{R}_{e \rightarrow b}(t)\mathbf{g}$  and  $\mathbf{b}_a(t)$  from the measured vector IMU quantities, boundlessly growing errors would inevitably still arise due to the integration operations. These errors, known as random walk errors, occur as a result of integrating noise terms, whereby the variance of the estimates increases proportionately to the integration time.

During a zero velocity update,  $\boldsymbol{\omega}(t) \equiv 0$  and  $\mathbf{a}(t) = 0$ , so that we have, respectively, from (15) and (16),

$$(20) \quad \tilde{\boldsymbol{\omega}}(t) = \mathbf{b}_\omega(t) + \mathbf{n}_\omega(t)$$

and

$$(21) \quad \tilde{\mathbf{a}}(t) = \mathbf{R}_{e \rightarrow b}^{ZV} \mathbf{g} + \mathbf{b}_a(t) + \mathbf{n}_a(t)$$

The term  $\mathbf{R}_{e \rightarrow b}^{ZV} \mathbf{g}$  in (21) denotes an orientation-dependent bias vector that is constant for the duration of the zero velocity update, and is represented explicitly via (18) with  $\theta(t)$  and  $\phi(t)$  as constants. Since  $\tilde{\boldsymbol{\omega}}(t)$  and  $\tilde{\mathbf{a}}(t)$  are, to first order, well represented by linear regression vectors during a zero velocity update, we choose to write

$$(22) \quad \mathbf{b}_\omega(t) = \mathbf{A}_\omega + \mathbf{B}_\omega t \quad \text{and} \quad \mathbf{b}_a(t) = \mathbf{A}_a + \mathbf{B}_a t$$

Making use of (22), the true IMU quantities of (15) and (16) can be expressed, in the mean, as

$$(23) \quad \boldsymbol{\omega}(t) = (\mathbf{1} + \boldsymbol{\delta}_\omega) \cdot (\tilde{\boldsymbol{\omega}}(t) - (\mathbf{A}_\omega + \mathbf{B}_\omega t))$$

and

$$(24) \quad \mathbf{a}(t) = (\mathbf{1} + \boldsymbol{\delta}_a) \cdot (\tilde{\mathbf{a}}(t) - \mathbf{R}_{e \rightarrow b}(t) \mathbf{g} - (\mathbf{A}_a + \mathbf{B}_a t))$$

where  $\mathbf{1} + \boldsymbol{\delta}_\omega \equiv \mathbf{s}_\omega^{-1}$ ;  $\mathbf{1} + \boldsymbol{\delta}_a \equiv \mathbf{s}_a^{-1}$ ;  $\mathbf{1}$  is the identity vector; and  $\boldsymbol{\delta}_\omega$ ,  $\boldsymbol{\delta}_a$  are scale factor error vectors. Furthermore, transforming (24) from the IMU body frame to the earth-fixed frame gives

$$(25) \quad \mathbf{a}^e(t) \equiv \mathbf{R}_{e \rightarrow b}^T(t) \mathbf{a}(t) = \mathbf{R}_{e \rightarrow b}^T(t) [(\mathbf{1} + \boldsymbol{\delta}_a) \cdot (\tilde{\mathbf{a}}(t) - (\mathbf{A}_a + \mathbf{B}_a t))] - (\mathbf{1} + \boldsymbol{\delta}_a) \cdot \mathbf{g}$$

where  $\mathbf{R}_{b \rightarrow e}(t) \equiv \mathbf{R}_{e \rightarrow b}^T(t)$  is the transpose of (17), and  $\mathbf{R}_{e \rightarrow b}^T(t) \mathbf{R}_{e \rightarrow b}(t) \equiv \mathbf{I}$ , the identity matrix.

From (23), it is clear that nine parameters are necessary to fully specify  $\boldsymbol{\omega}(t)$ . An additional six parameters are needed to accurately determine the yaw, pitch and roll angles from  $\boldsymbol{\omega}(t)$  via (19); three related to the initial angles, and three related to the final angles. The former are crucial for proper initialization of (19), while the latter are required to confine the random walk errors that arise due to the integration operations. An appropriate choice for these parameters are the error angles  $\delta\psi_i = \psi_i - \hat{\psi}_i$ ,  $\delta\theta_i = \theta_i - \hat{\theta}_i$ ,  $\delta\phi_i = \phi_i - \hat{\phi}_i$ ,  $\delta\psi_f = \psi_f - \hat{\psi}_f$ ,  $\delta\theta_f = \theta_f - \hat{\theta}_f$  and  $\delta\phi_f = \phi_f - \hat{\phi}_f$ , where  $\psi_i$ ,  $\theta_i$  and  $\phi_i$  are the true initial yaw, pitch and roll angles, respectively;  $\hat{\psi}_i$ ,  $\hat{\theta}_i$  and  $\hat{\phi}_i$  are the estimated initial yaw, pitch and roll angles, respectively; and  $\psi_f$ ,  $\theta_f$ ,  $\phi_f$ , and  $\hat{\psi}_f$ ,  $\hat{\theta}_f$ ,  $\hat{\phi}_f$  are the true and estimated final angles, respectively.

By starting and ending with zero velocity updates, both the initial and final pitch and roll angles can be estimated from the measured acceleration vector using (18), (21) and (22). That is,

$$\mathbf{R}_{e \rightarrow b}^{ZV} \mathbf{g} \equiv \begin{bmatrix} -\sin \hat{\theta}^{ZV} \\ \cos \hat{\theta}^{ZV} \sin \hat{\phi}^{ZV} \\ \cos \hat{\theta}^{ZV} \cos \hat{\phi}^{ZV} \end{bmatrix} \mathbf{g} = \tilde{\mathbf{a}}(t) - (\mathbf{A}_a + \mathbf{B}_a t)$$

which leads to

$$(26) \quad \hat{\theta}^{ZV} = \sin^{-1} \left( -\frac{(\tilde{a}_x(t) - (A_{a_x} + B_{a_x} t))}{g} \right) \quad \text{and} \quad \hat{\phi}^{ZV} = \sin^{-1} \left( \frac{(\tilde{a}_y(t) - (A_{a_y} + B_{a_y} t))}{g \cos \hat{\theta}^{ZV}} \right)$$

If it is assumed that estimates for the initial and final yaw angles are also available, then, by specifying the six angle error parameters, the true initial and final angles are fully determined. This allows needed linear corrections to be made to each of the  $\psi(t)$ ,  $\theta(t)$  and  $\phi(t)$  solutions to (19).

From (25), to fully determine  $\mathbf{a}^e(t)$  then, we need the 15 parameters just described to completely specify the rotation matrix, and an additional 9 parameters for a total of 24 parameters. The velocity vector – which is the integration of  $\mathbf{a}^e(t)$  – is consequently fully determined since we

know what the true initial and final velocities are, thereby allowing linear corrections to be applied. If we start and end at the same position, the same can be said of the position vector – which is the integration of the velocity vector.

With all of the assumptions made above, we can therefore completely specify the position vector in the earth-fixed frame between two co-located zero velocity updates with 24 parameters:

$$\delta_{\omega}, \mathbf{A}_{\omega}, \mathbf{B}_{\omega}, \delta_{\mathbf{a}}, \mathbf{A}_{\mathbf{a}}, \mathbf{B}_{\mathbf{a}}, \delta\psi_i, \delta\theta_i, \delta\phi_i, \delta\psi_f, \delta\theta_f \text{ and } \delta\phi_f$$

## 6.2. Test Setup

A considerable simplification in the collection process was sought in order to attempt to understand the limitations involved in the compensation process of 3D motion IMU data. This involved sweeping the IMU sensor by itself from side-to-side and placing it on the ground at the end of each sweep for zero velocity updates. To implement this, a series of fixed locations on the test platform were marked by right angle metal braces and held in place using wooden dowels (see Figure 50). The locations were numbered 1 through 6 and midpoint to midpoint separations noted so that the relative zero velocity update positions were known. The IMU was then simply lifted and hand-placed at a series of locations, with the data being collected via a serial cable onto a laptop running GyroView.

The IMU was always oriented the same way on the left side (i.e. locations 1, 3 & 5) and 90 degrees from this on the right side (i.e. locations 2, 4 & 6). The start and finish IMU positions were always at location 1. It should be noted that the IMU placement was not always exact – sometimes it landed on the metal brace and was slightly tilted, and sometimes it was up to ¼ “ off position. To average these out, the IMU was moved back and forth between locations multiple times, and the measurements repeated several times.

## 6.3. Processing and analysis

The zero velocity update method comprises of the following sequence of steps:

- Determination of the angular rate bias vector
- Determination of the acceleration bias vector
- Determination of the orientation angles of the IMU body relative to the Earth’s frame
- Integration of the fully compensated acceleration vector in the Earth’s frame

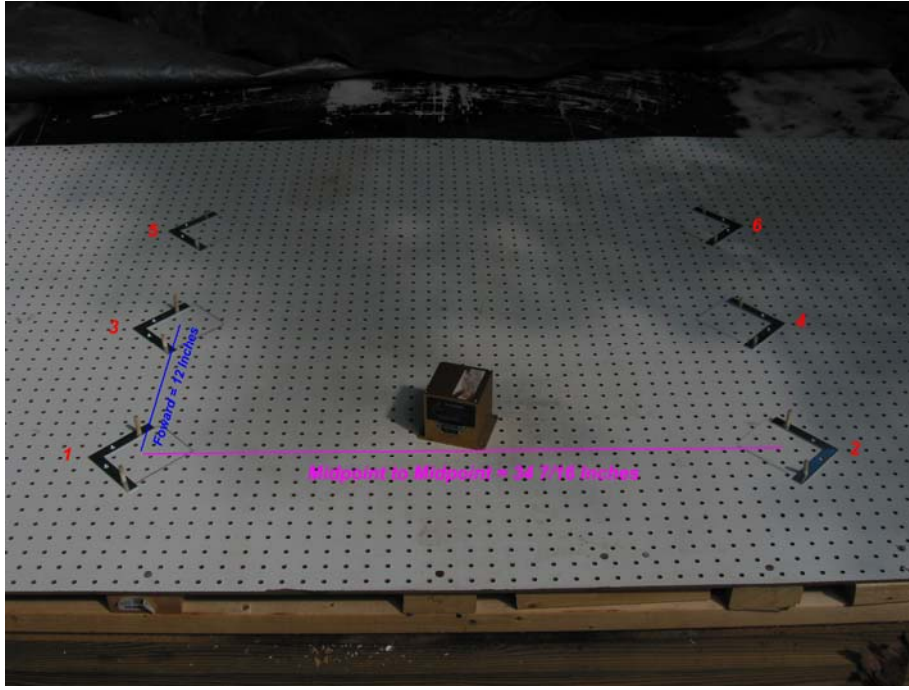


**Figure 50: Setup for 3D motion of just the IMU.**

The qualifier “fully” implies compensation of both the bias vector and the gravitational contribution, over all time. In the following sections we will trace these processing steps using the 3D IMU data collected as described in the discussion of Figure 50. For comparison, we will compare the results with performance based on processing static IMU data.

### **6.3.1. Determination of the Angular Rate Bias Vector**

The determination of the angular rate bias vector via (20) is relatively straightforward. With sufficient zero velocity updates taken periodically, a global representation of  $\mathbf{b}_\omega(t)$  can be defined. To first order, this is well represented by separate linear trends for each of the three components, i.e.

$$b_{\omega_x}(t) = m_{\omega_x}t + c_{\omega_x}$$

$$b_{\omega_y}(t) = m_{\omega_y}t + c_{\omega_y}$$

$$b_{\omega_z}(t) = m_{\omega_z}t + c_{\omega_z}$$

#### *The Static IMU*

Consider a 50 minute time series of static IMU data. Performing a linear regression on each of the angular rate components over the 50 minute segment, yields

$$\begin{aligned}
m_{\omega_x} &= 11.47 \times 10^{-6} \text{ }^\circ / s^2 \quad \text{and} \quad c_{\omega_x} = 0.19880433 \text{ }^\circ / s \\
m_{\omega_y} &= 0.60 \times 10^{-6} \text{ }^\circ / s^2 \quad \text{and} \quad c_{\omega_y} = 0.11388729 \text{ }^\circ / s \\
m_{\omega_z} &= 1.39 \times 10^{-6} \text{ }^\circ / s^2 \quad \text{and} \quad c_{\omega_z} = 0.11041257 \text{ }^\circ / s
\end{aligned}$$

Over the entire 50 minutes of data, the compensated angular rate components give

$$\begin{aligned}
\langle \tilde{\omega}_x(t) - b_{\omega_x}(t) \rangle &= -8.0 \times 10^{-14} \text{ }^\circ / s \quad \text{and} \quad \sigma(n_{\omega_x}) = 0.300 \text{ }^\circ / s \\
\langle \tilde{\omega}_y(t) - b_{\omega_y}(t) \rangle &= -5.7 \times 10^{-15} \text{ }^\circ / s \quad \text{and} \quad \sigma(n_{\omega_y}) = 0.332 \text{ }^\circ / s \\
\langle \tilde{\omega}_z(t) - b_{\omega_z}(t) \rangle &= -2.6 \times 10^{-16} \text{ }^\circ / s \quad \text{and} \quad \sigma(n_{\omega_z}) = 0.327 \text{ }^\circ / s
\end{aligned}$$

where  $\langle \bullet \rangle$  denotes averaging, and  $\sigma(\bullet)$  denotes computing the standard deviation.

If instead, consecutive 1 second windows of data over the entire 50 minutes of data are considered, we have

$$\begin{aligned}
\langle \tilde{\omega}_x(t) - b_{\omega_x}(t) \rangle &= 5.85 \times 10^{-7} \pm 0.010465650 \text{ }^\circ / s \quad \text{and} \quad \sigma(n_{\omega_x}) = 0.301 \pm 0.020 \text{ }^\circ / s \\
\langle \tilde{\omega}_y(t) - b_{\omega_y}(t) \rangle &= -1.89 \times 10^{-7} \pm 0.014537236 \text{ }^\circ / s \quad \text{and} \quad \sigma(n_{\omega_y}) = 0.332 \pm 0.023 \text{ }^\circ / s \\
\langle \tilde{\omega}_z(t) - b_{\omega_z}(t) \rangle &= -3.75 \times 10^{-7} \pm 0.014223592 \text{ }^\circ / s \quad \text{and} \quad \sigma(n_{\omega_z}) = 0.327 \pm 0.022 \text{ }^\circ / s
\end{aligned}$$

It should be noted that although the mean of the average values still approaches zero, local deviations on the order of  $0.01 \text{ }^\circ / s$  occur as a result of the linear trend assumptions made.

### *The Unconstrained Moving IMU*

Consider the IMU 3D motion data for the back and forth sweeping between two fixed points defined by right angle metal braces secured to the test platform. Zero velocity updates for a minimum of 5 seconds each were conducted at the fixed points. The time in motion between the zero velocity updates typically lasted under 3 seconds.

Performing a linear regression on each of the angular rate components (using the data over all zero velocity update segments), yields

$$\begin{aligned}
m_{\omega_x} &= -5.15 \times 10^{-6} \text{ }^\circ / s^2 \quad \text{and} \quad c_{\omega_x} = 0.16389530 \text{ }^\circ / s \\
m_{\omega_y} &= -123.13 \times 10^{-6} \text{ }^\circ / s^2 \quad \text{and} \quad c_{\omega_y} = 0.24644612 \text{ }^\circ / s \\
m_{\omega_z} &= 67.94 \times 10^{-6} \text{ }^\circ / s^2 \quad \text{and} \quad c_{\omega_z} = 0.08594225 \text{ }^\circ / s
\end{aligned}$$

Comparing these regression coefficients to the ones obtained in the previous example, it is clear that both the slope and initial bias coefficient values can vary significantly. This reinforces the importance of taking zero velocity updates, if for no other reason than to determine the appropriate  $\mathbf{b}_\omega(t)$  for the data in question.

Figure 51 below shows the mean (diamond symbols) and standard deviation (error bars) of the angular rate components at each of the zero velocity updates, with the derived linear regression curves over-plotted in red. The mean values have been placed at the temporal midpoint of each zero velocity update duration.

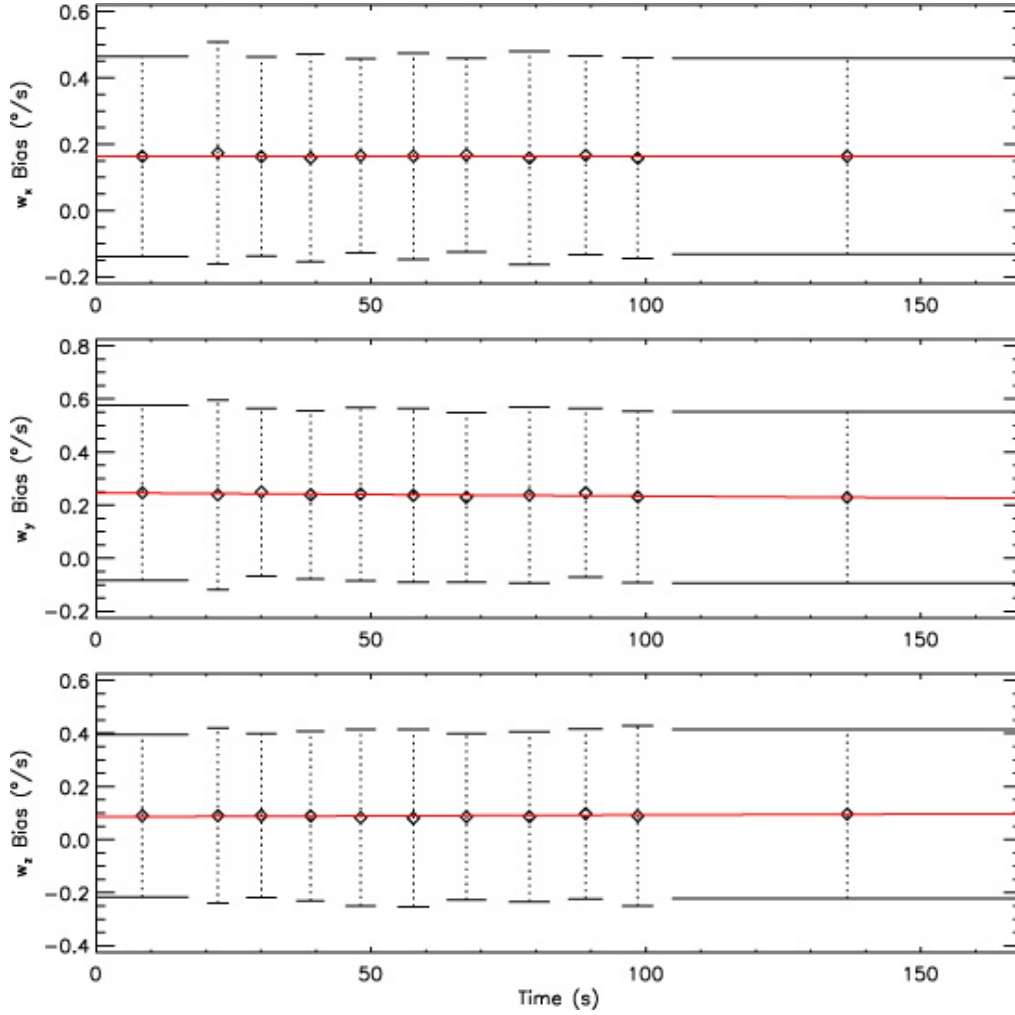


**Figure 51:** The angular rate bias vector components plotted [in red] with the mean and standard deviation for each of the zero velocity updates.

Subtracting each linear regression curve from the respective angular rate component, gives, over all zero velocity update segments

$$\langle \tilde{\omega}_x(t) - b_{\omega_x}(t) \rangle = -2.11 \times 10^{-7} \pm 0.004490364 \text{ } ^\circ/\text{s} \quad \text{and} \quad \sigma(n_{\omega_x}) = 0.305 \pm 0.013 \text{ } ^\circ/\text{s}$$

$$\langle \tilde{\omega}_y(t) - b_{\omega_y}(t) \rangle = -1.22103 \times 10^{-4} \pm 0.005412638 \text{ } ^\circ/\text{s} \quad \text{and} \quad \sigma(n_{\omega_y}) = 0.326 \pm 0.011 \text{ } ^\circ/\text{s}$$

$$\langle \tilde{\omega}_z(t) - b_{\omega_z}(t) \rangle = -1.252090 \times 10^{-3} \pm 0.004714105 \text{ } ^\circ/\text{s} \quad \text{and} \quad \sigma(n_{\omega_z}) = 0.322 \pm 0.011 \text{ } ^\circ/\text{s}$$

which is, more or less, in line with what was obtained for the compensated angular rate components in the previous example of the static IMU.

### 6.3.2. Determination of the Acceleration Bias Vector

The determination of the acceleration bias vector via (21) is more ambiguous. During any particular zero velocity update, the term  $\mathbf{R}_{e \rightarrow b}(t)\mathbf{g}$  will contribute an orientation-dependent constant bias vector to the measured acceleration vector. Without an independent measure of this contribution, the best we can do to determine the acceleration bias vector is to *use only zero velocity update data where the IMU orientation was known to be identical*. In so doing, (16) can be recast as

$$(27) \quad \tilde{\mathbf{a}}(t) = \mathbf{b}'_a(t) + \mathbf{n}_a(t)$$

where the global representation of  $\mathbf{b}'_a(t)$  now has the orientation-dependent constant vector absorbed into it. As with the angular rate bias vector, to first order,  $\mathbf{b}'_a(t)$  is well represented by separate linear trends for each of the three components, i.e.

$$\begin{aligned} b'_{a_x}(t) &= m_{a_x}t + c_{a_x} \\ b'_{a_y}(t) &= m_{a_y}t + c_{a_y} \\ b'_{a_z}(t) &= m_{a_z}t + c_{a_z} \end{aligned}$$

where now  $\mathbf{c}_a \equiv \mathbf{R}_{e \rightarrow b}(0)\mathbf{g} + \mathbf{b}_a(0)$ . Again, since we do not have independent confirmation of  $\mathbf{R}_{e \rightarrow b}(0)\mathbf{g}$ , it is currently assumed that  $\mathbf{b}_a(0) = \mathbf{0}$ .

#### *The Static IMU*

Consider the same 50 minute time series of static IMU data as before. Noting that the orientation of the IMU body remains unchanged throughout, a linear regression on each of the acceleration components over the entire 50 minutes can be performed, yielding

$$\begin{aligned} m_{a_x} &= 9.9 \times 10^{-8} \text{ g/s} \quad \text{and} \quad c_{a_x} = 0.000171506 \text{ g} \\ m_{a_y} &= -60.2 \times 10^{-8} \text{ g/s} \quad \text{and} \quad c_{a_y} = 0.020438798 \text{ g} \\ m_{a_z} &= 0.5 \times 10^{-8} \text{ g/s} \quad \text{and} \quad c_{a_z} = 0.998410810 \text{ g} \end{aligned}$$

Over the entire 50 minutes of data, the compensated acceleration components give

$$\begin{aligned} \langle \tilde{a}_x(t) - b'_{a_x}(t) \rangle &= 3.8 \times 10^{-16} \text{ g} \quad \text{and} \quad \sigma(n_{a_x}) = 0.001159 \text{ g} \\ \langle \tilde{a}_y(t) - b'_{a_y}(t) \rangle &= 8.6 \times 10^{-15} \text{ g} \quad \text{and} \quad \sigma(n_{a_y}) = 0.001390 \text{ g} \\ \langle \tilde{a}_z(t) - b'_{a_z}(t) \rangle &= 1.6 \times 10^{-13} \text{ g} \quad \text{and} \quad \sigma(n_{a_z}) = 0.001174 \text{ g} \end{aligned}$$

If instead, consecutive 1 second windows of data over the entire 50 minutes of data are considered, we have



$$\begin{aligned}\langle \tilde{a}_x(t) - b'_{a_x}(t) \rangle &= 3.0 \times 10^{-9} \pm 0.0001291835 \text{ g} \quad \text{and} \quad \sigma(n_{a_x}) = (11.52 \pm 0.95) \times 10^{-4} \text{ g} \\ \langle \tilde{a}_y(t) - b'_{a_y}(t) \rangle &= 1.5 \times 10^{-9} \pm 0.0001280888 \text{ g} \quad \text{and} \quad \sigma(n_{a_y}) = (13.85 \pm 1.00) \times 10^{-4} \text{ g} \\ \langle \tilde{a}_z(t) - b'_{a_z}(t) \rangle &= -3.0 \times 10^{-9} \pm 0.0001145845 \text{ g} \quad \text{and} \quad \sigma(n_{a_z}) = (11.69 \pm 0.94) \times 10^{-4} \text{ g}\end{aligned}$$

Again, although the mean of the average values still approaches zero, local deviations on the order of 0.1 mg occur as a result of the linear trend assumptions made.

### *The Unconstrained Moving IMU*

Consider the same IMU 3D motion data as before. Performing a linear regression on each of the acceleration components, using only the initial and final zero velocity update data (the IMU orientation was known to be identical during these updates), yields

$$\begin{aligned}m_{a_x} &= -13.75 \times 10^{-7} \text{ g/s} \quad \text{and} \quad c_{a_x} = 0.000434544 \text{ g} \\ m_{a_y} &= 3.82 \times 10^{-7} \text{ g/s} \quad \text{and} \quad c_{a_y} = 0.001184215 \text{ g} \\ m_{a_z} &= -3.23 \times 10^{-7} \text{ g/s} \quad \text{and} \quad c_{a_z} = 0.998566701 \text{ g}\end{aligned}$$

Subtracting each linear regression curve from the respective acceleration component, gives, over the initial and final zero velocity update segments

$$\begin{aligned}\langle \tilde{a}_x(t) - b'_{a_x}(t) \rangle &= (4.88 \pm 11.82) \times 10^{-7} \text{ g} \quad \text{and} \quad \sigma(n_{a_x}) = (9.14 \pm 0.64) \times 10^{-4} \text{ g} \\ \langle \tilde{a}_y(t) - b'_{a_y}(t) \rangle &= (36.87 \pm 89.28) \times 10^{-7} \text{ g} \quad \text{and} \quad \sigma(n_{a_y}) = (14.68 \pm 0.52) \times 10^{-4} \text{ g} \\ \langle \tilde{a}_z(t) - b'_{a_z}(t) \rangle &= (11.65 \pm 28.23) \times 10^{-7} \text{ g} \quad \text{and} \quad \sigma(n_{a_z}) = (11.35 \pm 2.03) \times 10^{-4} \text{ g}\end{aligned}$$

The fact that the deviations about the mean are much smaller than in the previous example is a direct consequence of having an inadequate statistical sampling. To be sure, if **all** the zero velocity update data where the IMU orientation was known to be identical (not just the initial and final segment data) is instead used, we have for the new linear regression coefficients

$$\begin{aligned}m_{a_x} &= -16.04 \times 10^{-7} \text{ g/s} \quad \text{and} \quad c_{a_x} = 0.000463814 \text{ g} \\ m_{a_y} &= 7.16 \times 10^{-7} \text{ g/s} \quad \text{and} \quad c_{a_y} = 0.001119055 \text{ g} \\ m_{a_z} &= -3.56 \times 10^{-7} \text{ g/s} \quad \text{and} \quad c_{a_z} = 0.998572324 \text{ g}\end{aligned}$$

Subtracting each linear regression curve from the respective acceleration component, gives, over the same zero velocity update data used to perform the regressions

$$\begin{aligned}
\langle \tilde{a}_x(t) - b'_{a_x}(t) \rangle &= (0.86 \pm 7.86) \times 10^{-5} g \quad \text{and} \quad \sigma(n_{a_x}) = (8.95 \pm 0.42) \times 10^{-4} g \\
\langle \tilde{a}_y(t) - b'_{a_y}(t) \rangle &= (-5.23 \pm 10.46) \times 10^{-5} g \quad \text{and} \quad \sigma(n_{a_y}) = (15.11 \pm 0.54) \times 10^{-4} g \\
\langle \tilde{a}_z(t) - b'_{a_z}(t) \rangle &= (0.55 \pm 2.25) \times 10^{-5} g \quad \text{and} \quad \sigma(n_{a_z}) = (10.78 \pm 1.14) \times 10^{-4} g
\end{aligned}$$

which is again, more or less, in line with what was obtained for the compensated acceleration components in the previous example of the static IMU.

### 6.3.3. Determination of the Orientation Angles

As noted earlier (19), the attitude of the IMU body frame relative to the Earth frame is determined from the compensated angular rates  $\omega_x(t)$ ,  $\omega_y(t)$  and  $\omega_z(t)$ , via the following coupled differential equations

$$\frac{d}{dt} \begin{bmatrix} \phi(t) \\ \theta(t) \\ \psi(t) \end{bmatrix} \equiv \begin{bmatrix} 1 & \sin \phi(t) \tan \theta(t) & \cos \phi(t) \tan \theta(t) \\ 0 & \cos \phi(t) & -\sin \phi(t) \\ 0 & \frac{\sin \phi(t)}{\cos \theta(t)} & \frac{\cos \phi(t)}{\cos \theta(t)} \end{bmatrix} \begin{bmatrix} \omega_x(t) \\ \omega_y(t) \\ \omega_z(t) \end{bmatrix}$$

where  $\psi(t)$ ,  $\theta(t)$  and  $\phi(t)$  are the yaw, pitch and roll angles, respectively. During zero velocity updates, an additional independent measure of both the pitch and roll angles is possible by making use of the de-biased acceleration data. Specifically, averaging (21) over the extent of the  $i$ -th zero velocity update that starts at time  $\tau_i$ , gives

$$(28) \quad \langle \tilde{\mathbf{a}}(t) - \mathbf{b}_a(t) \rangle = \mathbf{R}_{e \rightarrow b}(\tau_i) \mathbf{g}$$

where, explicitly in terms of the Euler angles,

$$(29) \quad \mathbf{R}_{e \rightarrow b}(\tau_i) \mathbf{g} \equiv \begin{bmatrix} -\sin \theta_{\tau_i} \\ \cos \theta_{\tau_i} \sin \phi_{\tau_i} \\ \cos \theta_{\tau_i} \cos \phi_{\tau_i} \end{bmatrix} g$$

and the constant angles  $\theta_{\tau_i}$  and  $\phi_{\tau_i}$  specify, respectively, the pitch and roll of the IMU body frame relative to the Earth frame during the  $i$ -th zero velocity update.

From (28) and (29),

$$(30) \quad \begin{bmatrix} \langle \tilde{a}_x(t) - b_{a_x}(t) \rangle \\ \langle \tilde{a}_y(t) - b_{a_y}(t) \rangle \\ \langle \tilde{a}_z(t) - b_{a_z}(t) \rangle \end{bmatrix} = \begin{bmatrix} -\sin \theta_{\tau_i} \\ \cos \theta_{\tau_i} \sin \phi_{\tau_i} \\ \cos \theta_{\tau_i} \cos \phi_{\tau_i} \end{bmatrix} g$$

allowing one to determine the angles via

$$(31) \quad \theta_{\tau_i} = \sin^{-1} \left( \frac{-\langle \tilde{a}_x(t) - b_{a_x}(t) \rangle}{g} \right)$$

and

$$(32) \quad \phi_{\tau_i} = \sin^{-1} \left( \frac{\langle \tilde{a}_y(t) - b_{a_y}(t) \rangle}{g \cos \theta_{\tau_i}} \right) = \cos^{-1} \left( \frac{\langle \tilde{a}_z(t) - b_{a_z}(t) \rangle}{g \cos \theta_{\tau_i}} \right)$$

It is implied in (31) and (32) that the averaging takes place over the duration of the  $i$ -th zero velocity update.

### *The Static IMU*

Again, consider the same 50 minute time series of static IMU data as before. Using the compensated angular rates, and assuming zero initial angles, the pitch and roll angles computed via (19) are shown in Figure 52 below.

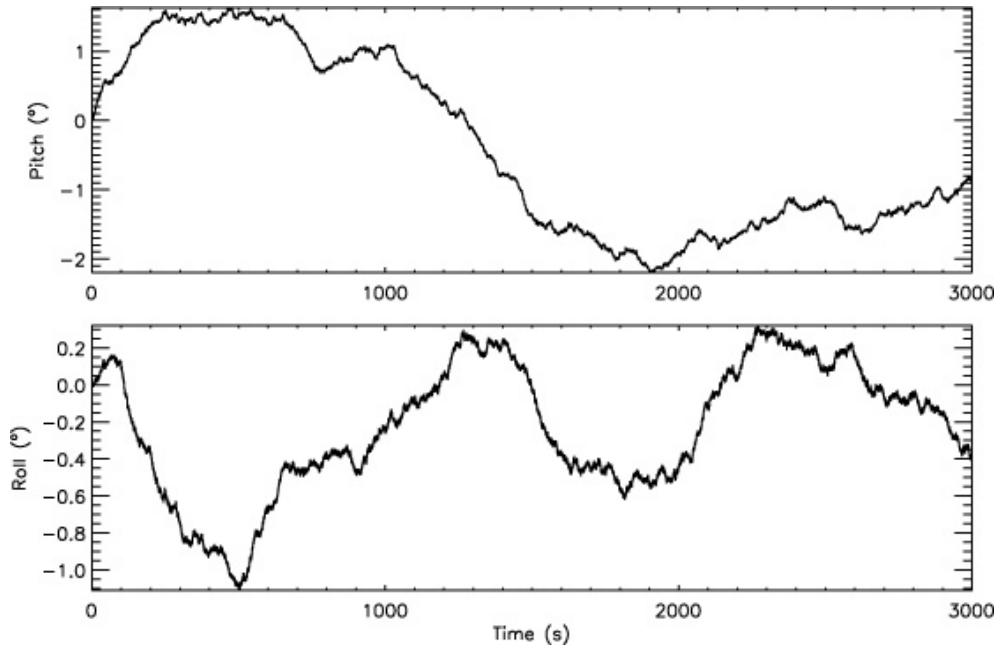


**Figure 52:** The pitch and roll angles determined via (19), for the case of the IMU sitting still on a table top for 50 minutes. Compensated angular rates have been used and initial angles of zero assumed.

Now assume that we have zero velocity updates of 5s duration, followed by 3s of unknown motion, for the entire 50 minutes. The zero velocity updates provide an additional independent measure of both pitch and roll angles, via (31) and 321). Since the computed angles over *all* the zero velocity updates vary by less than  $0.01^\circ$ , these angles serve well to constrain inevitable angular errors that evolve via the usage of (19).

Figure 53 shows the result of forcing the pitch and roll angles over the zero velocity updates (shown in red) to be those computed via (31) and (32), while using (19) to determine the angles between the zero velocity updates (shown in black). The additional effect of removing linear

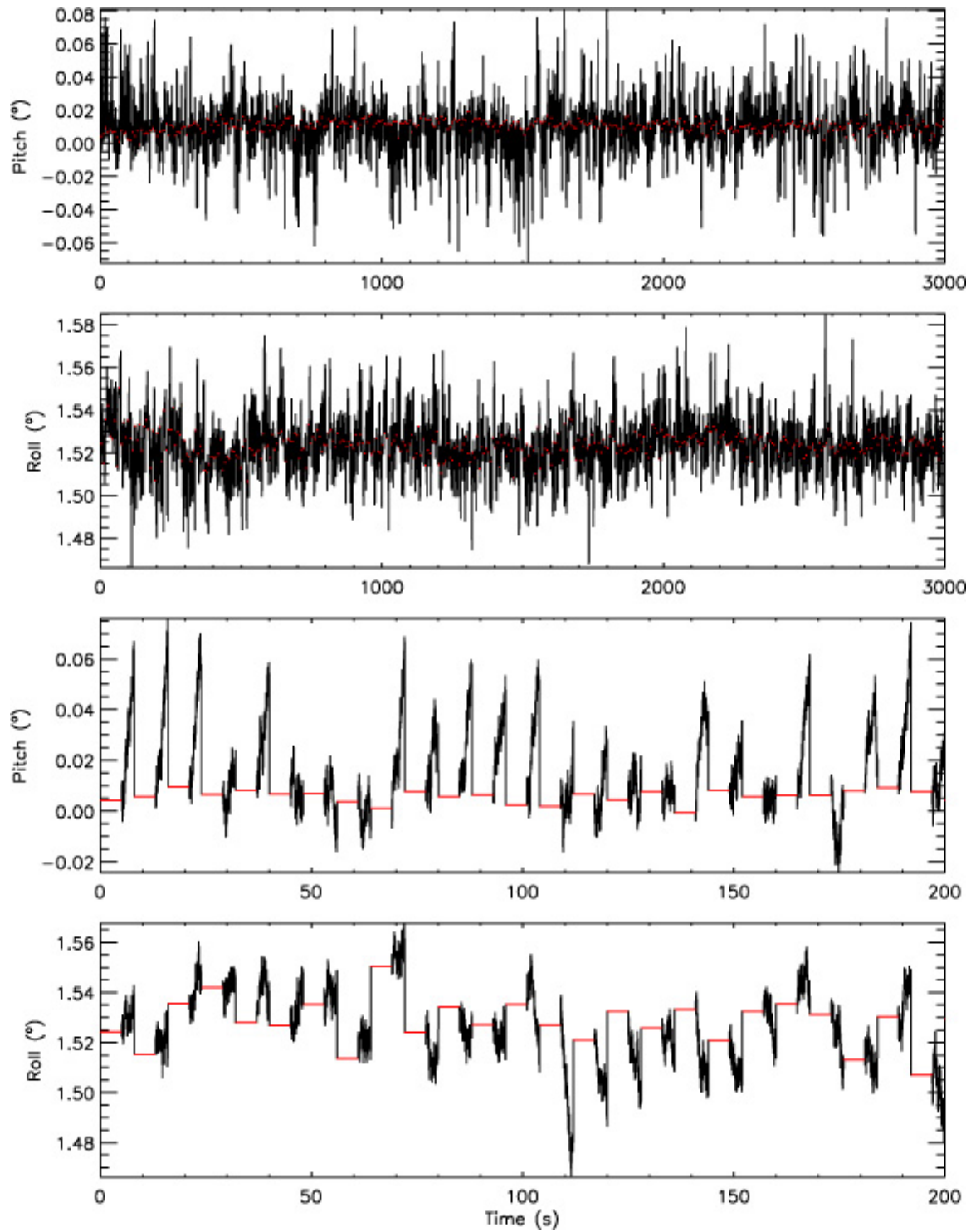
trends between the zero velocity updates, so that angles at the end of these segments agree with angles at the subsequent zero velocity update, is shown in Figure 54. The bottom two panels in both Figures 53 and 54 show close ups of the first 200 seconds of the data in the top two panels.

### *The Unconstrained Moving IMU*

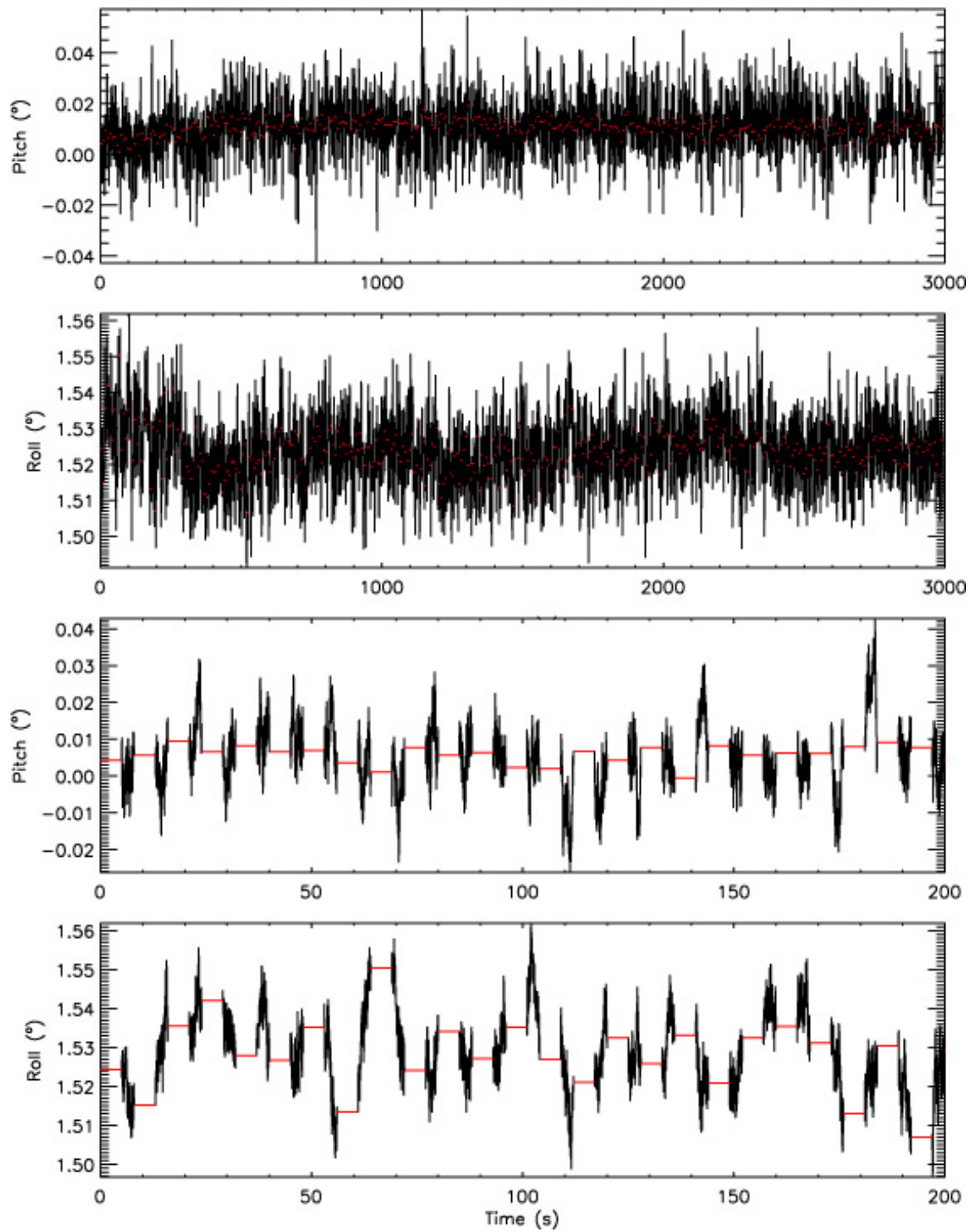
Again, consider the same IMU 3D motion data as before. Using the compensated angular rates, and assuming zero initial angles, the pitch and roll angles computed via (19) are shown in Figure 55 below. The data at the two fixed points (about which the sweeping takes place) are explicitly represented in red, for one point, and green, for the other. Apart from an obvious anomalous orientation on the second return to the first point, gradual temporal trends are observed for the angles at the fixed points – most notably for the pitch angle at the first fixed point. The trends, however, are not well represented by simple low order polynomials.

Figure 56 shows the result of forcing the pitch and roll angles over the zero velocity updates (taken at the fixed points mentioned above) to be those computed via (31) and (32), while using (19) to determine the angles between the zero velocity updates. The additional effect of removing linear trends between the zero velocity updates, so that angles at the end of these segments agree with angles at the subsequent zero velocity update, is shown in Figure 57.

By using compensated pitch and roll angles, along with compensated angular rates, a favorable estimate of the yaw angle via (19) is now possible. The top panel of Figure 58 shows the yaw angle obtained by simply assuming an initial angle of  $-45^\circ$  in (6). Since the IMU body is known to eventually return to its initial position and orientation, a final yaw angle of  $-45^\circ$  is also assumed. The bottom panel shows the result of subtracting a linear trend from the yaw angle in the top panel, so that the final computed angle agrees with the assumed final angle of  $-45^\circ$ .



**Figure 53:** The pitch and roll angles determined via (31) and (32), respectively, using the de-biased accelerations over assumed 5 second zero velocity updates [in red], and via (19) using the compensated angular rates during assumed 3 second segments of unknown motion between updates [in black], for the case of the IMU sitting still on a table top for 50 minutes. The bottom two panels are close ups of the first 200 seconds.



**Figure 54:** The pitch and roll angles of Figure 53, but with linear trends subtracted from the assumed segments of unknown motion between updates. Any discontinuities that existed between the angles at the end of these segments and those at the subsequent zero velocity updates have been removed. As before, the bottom two panels are close ups of the first 200 seconds.

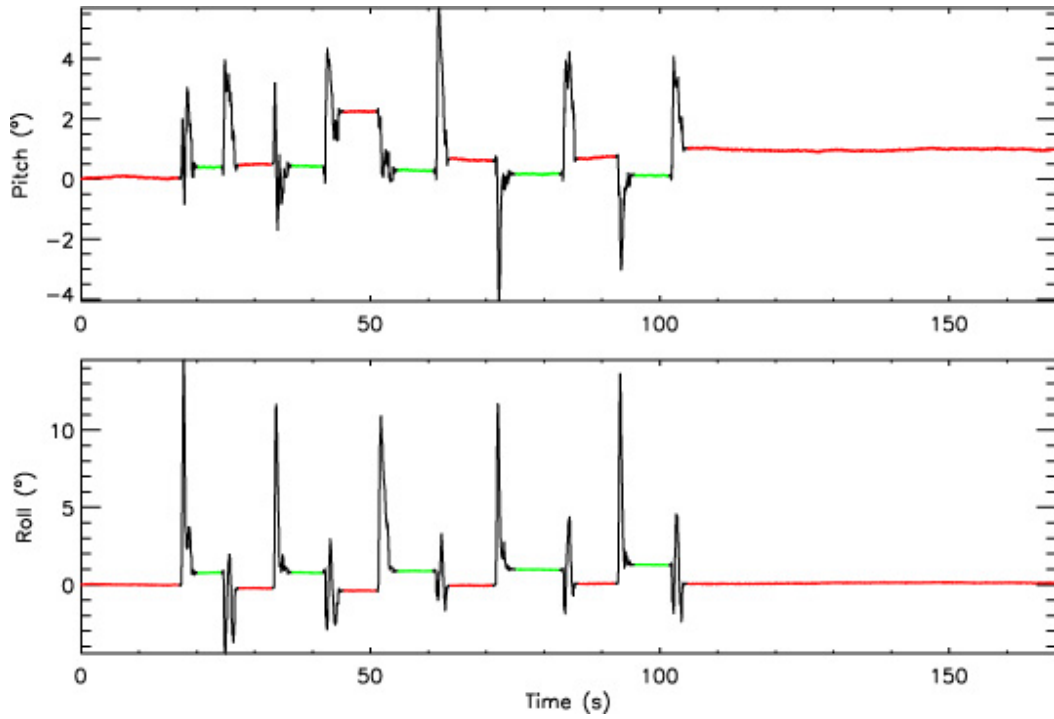


**Figure 55:** The pitch and roll angles determined via (19), for the case of back and forth 3D sweeping motion of the IMU between two well-defined fixed points [represented by the red and green data]. Compensated angular rates have been used and initial angles of zero assumed.

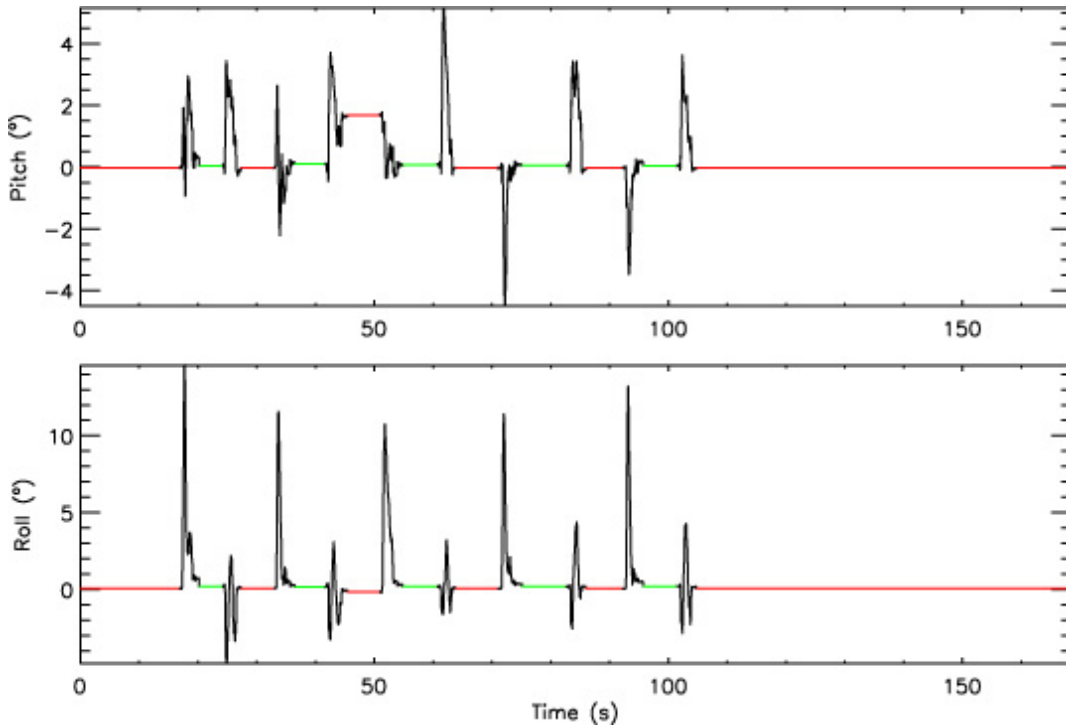


**Figure 56:** The pitch and roll angles determined via (31) and (32), respectively, using the de-biased accelerations during the zero velocity updates [in red and green], and via (19) using the compensated angular rates between updates [in black], for the case of back and forth 3D sweeping motion of the IMU between two well-defined fixed zero velocity update points.

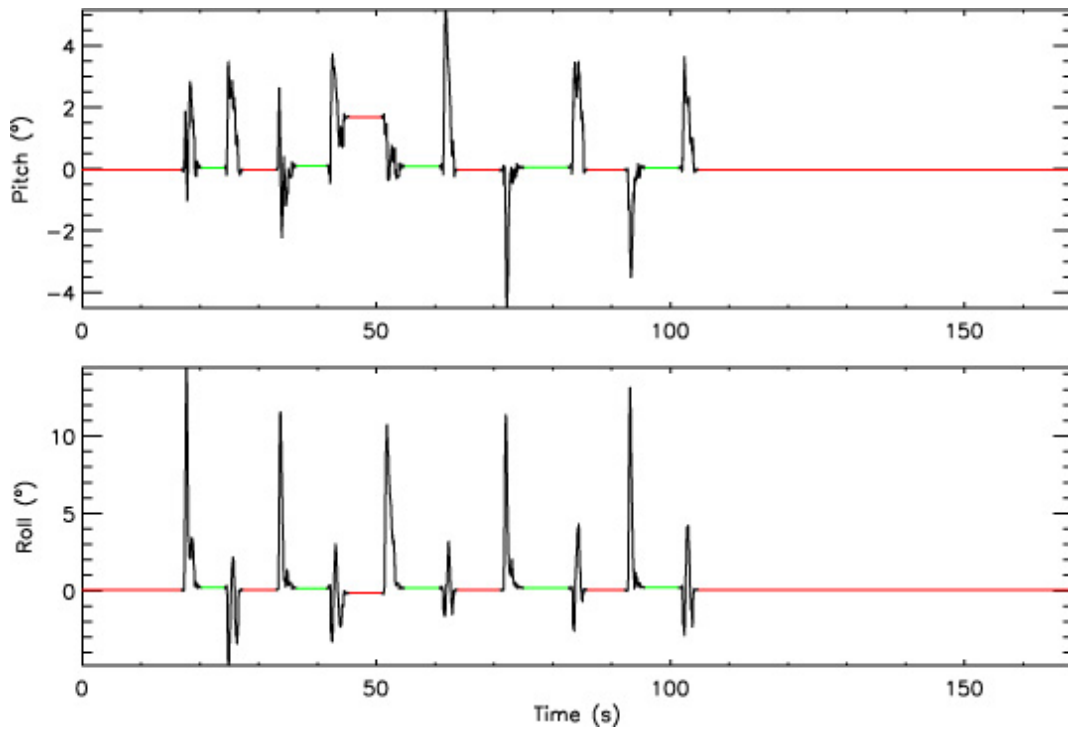


**Figure 57:** The pitch and roll angles of Figure 56, but with linear trends subtracted between zero velocity updates so as to remove any existing discontinuities.

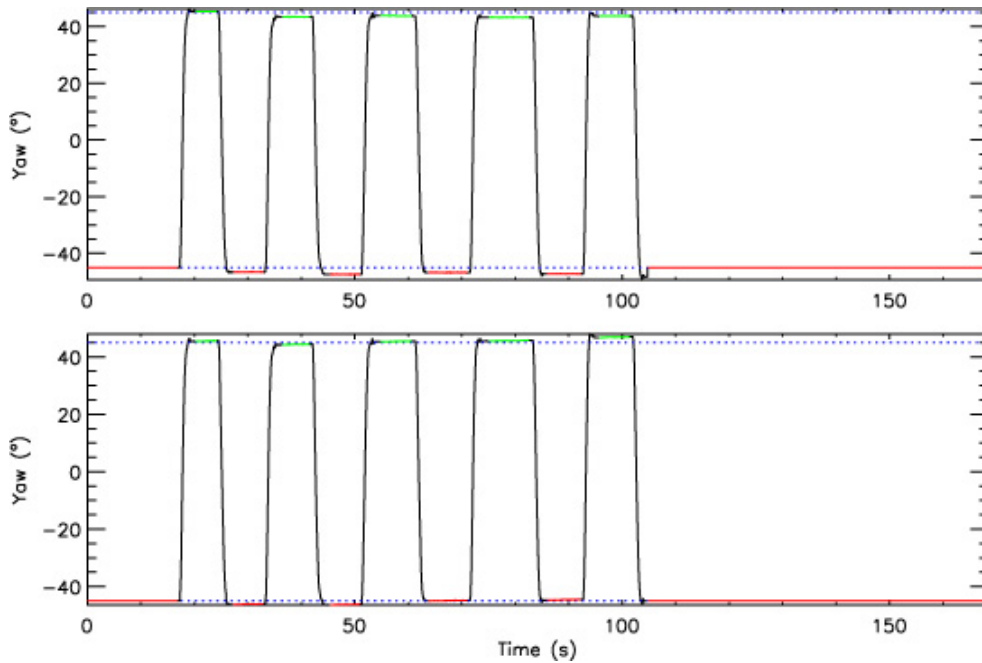


**Figure 58:** The yaw angle determined via (19) using the compensated angular rates and the compensated pitch and roll angles of Figure 57. The yaw angles during the initial and final zero velocity updates were assumed to be  $-45^\circ$ . The bottom panel shows the compensated yaw angle, where a linear trend has been subtracted between the end of the initial, and the beginning of the final, zero velocity updates.

#### 6.3.4. Integration of the Fully Compensated Acceleration Vector



Having determined the compensated pitch and roll angles, the gravitational contribution to the acceleration vector,  $\mathbf{R}_{e \rightarrow b}(t)\mathbf{g}$ , is now known over all  $t$ . With this, an estimate of the true (or fully compensated) acceleration vector  $\mathbf{a}(t)$  is achievable via (16).

Recall that the vector  $\mathbf{a}(t)$  of (16) is defined in the IMU body frame. Since the goal is to determine the position of the IMU in the Earth frame, it is necessary to transform the vector  $\mathbf{a}(t)$  from the IMU body frame to the Earth frame before carrying out the successive integration operations to obtain the velocity, followed by the position, vectors.

### *The Static IMU*

Consider the same static IMU data as before and, again, assume that we have zero velocity updates of 5s duration, followed by 3s of unknown motion, for the entire 50 minutes. The compensated pitch and roll angles have already been determined for this case (refer to Figure 54). The gravitational contribution to the acceleration vector, for all  $t$ , is therefore known and the full compensation of the acceleration vector is now possible via (16). Figure 59 below shows that when this is evaluated, however, a residual bias in the z-component still persists, requiring a revision in our previous assumption of  $\mathbf{b}_a(0) = \mathbf{0}$ . We shall see later that a more thorough revision of this assumption is needed in order to attain the cm level accuracy in positioning that this project ultimately seeks.

Subtracting the residual bias from the z-component yields the fully compensated acceleration vector. Transforming this vector from the IMU body frame to the Earth frame and integrating, results in the velocity vector shown in Figure 60 below. Since, by definition, the velocity is zero during zero velocity updates, the integration process is only carried out between updates, during segments of assumed unknown motion. The additional effect of subtracting linear trends between the zero velocity updates is shown in Figure 61 below. This is done so as to force agreement between what the integration tells us the velocity ought to be, and what we know the velocity to be, at the subsequent updates.

Finally, integrating the compensated velocity vector of Figure 61 provides an estimate of the position vector. Figures 62 and 63 show the outcome of this integration process with three separate assumptions used. If no assumption other than an initial position of zero is made, the results are the black curves of Figures 62 and 63. In order to reduce the positional errors that inevitably accumulate over time, assumptions based on revisiting known positions – i.e. zero position updates, in this case – are examined. The green curves represent the result of assuming a final zero position update, while the red curves represent the result of assuming zero position updates at every 25<sup>th</sup> zero velocity update. It is clear from Figure 63 that with sufficient zero position updates, the errors can be reduced to the desired cm level for the entire 50 minute duration.

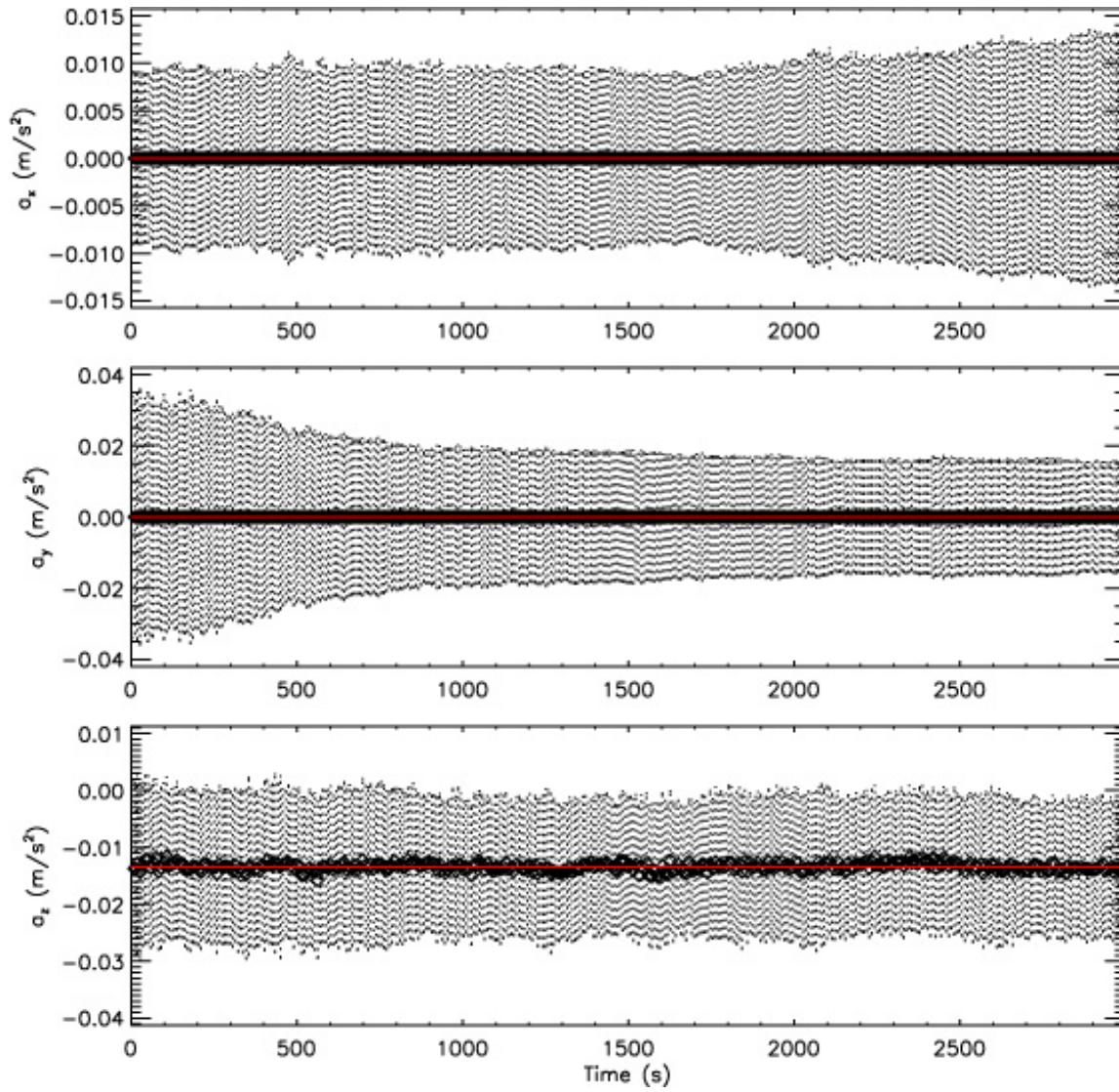


**Figure 59:** The mean and standard deviation of the compensated acceleration components over each of the assumed zero velocity updates, for the case of the IMU sitting still on a table top for 50 minutes. Due to the proximity and sheer quantity of updates, the diamonds representing the means appear to merge into continuous thick dark curves, while the error bars produce the lighter fabric that envelope the mean curves. The red curves represent residual linear trends.

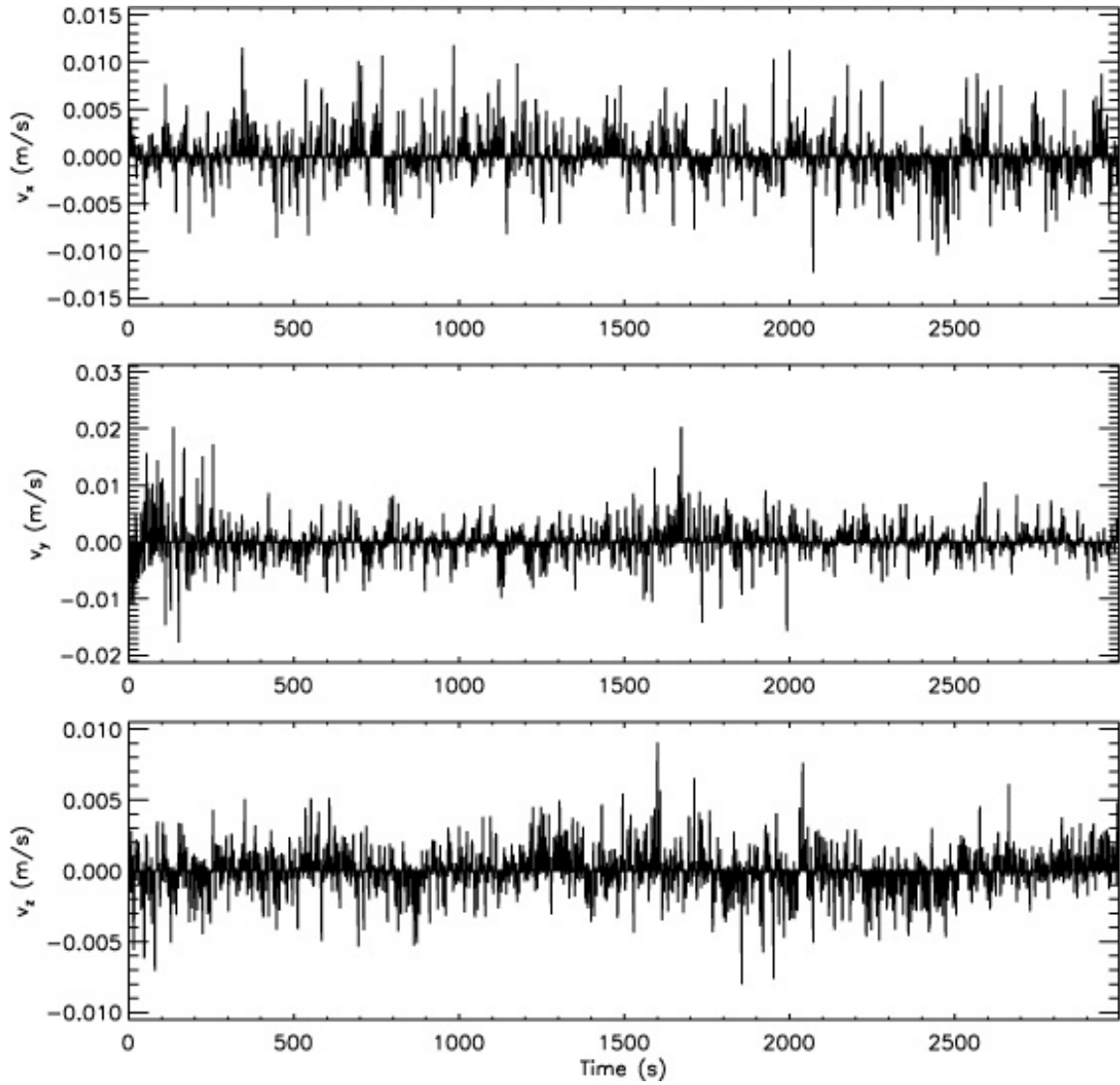


**Figure 60:** The velocity components obtained by integrating the corresponding fully compensated acceleration components between the assumed zero velocity updates, for the case of the IMU sitting still on a table top for 50 minutes. By definition, the velocity is zero during the zero velocity updates. The fully compensated acceleration components used here have had the residual trends, shown in Figure 59, subtracted from each component, and have also been transformed from the IMU body frame to the Earth frame.

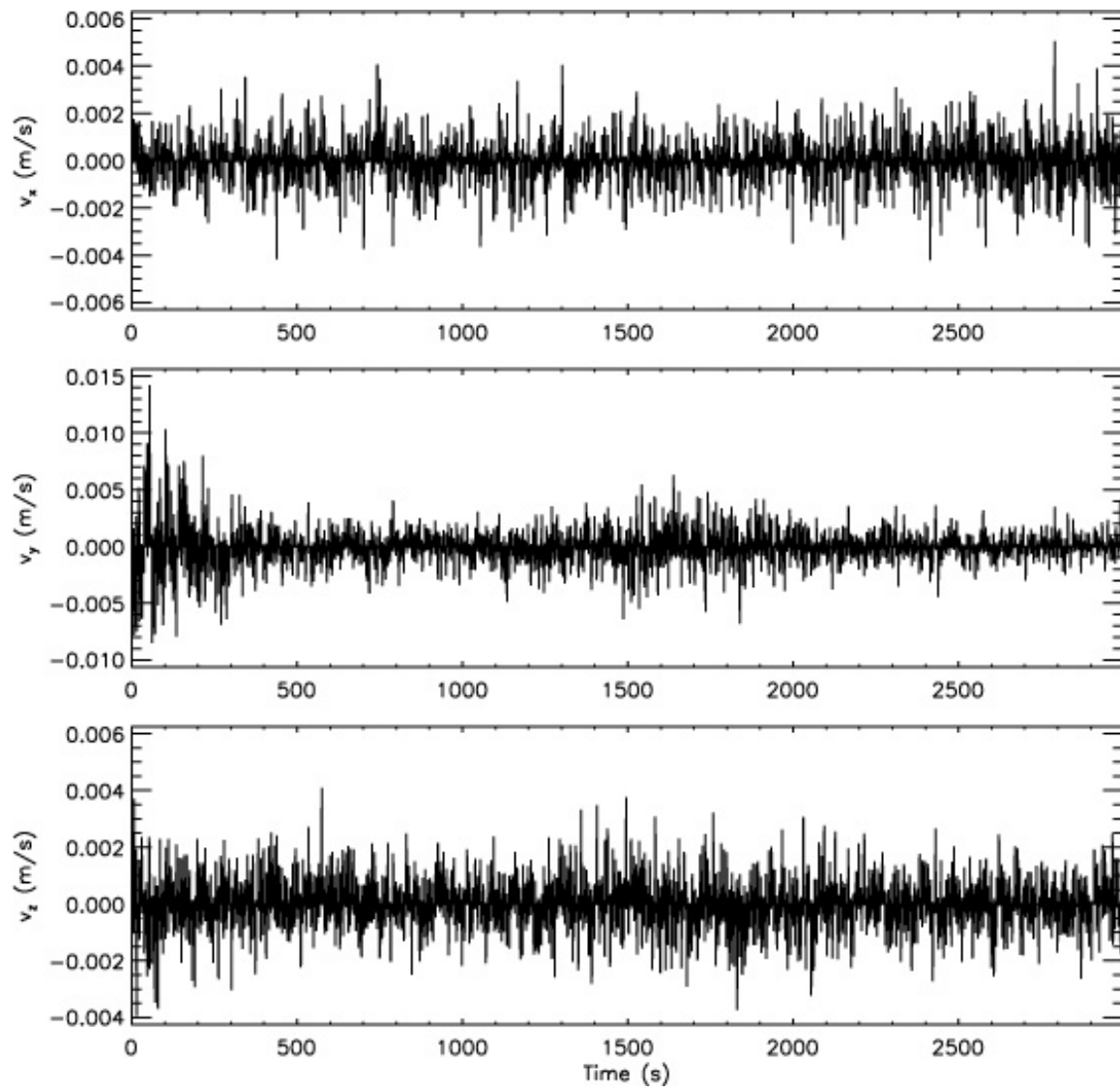


**Figure 61:** The velocity components of Figure 55, but with linear trends subtracted between zero velocity updates so as to remove any existing discontinuities.

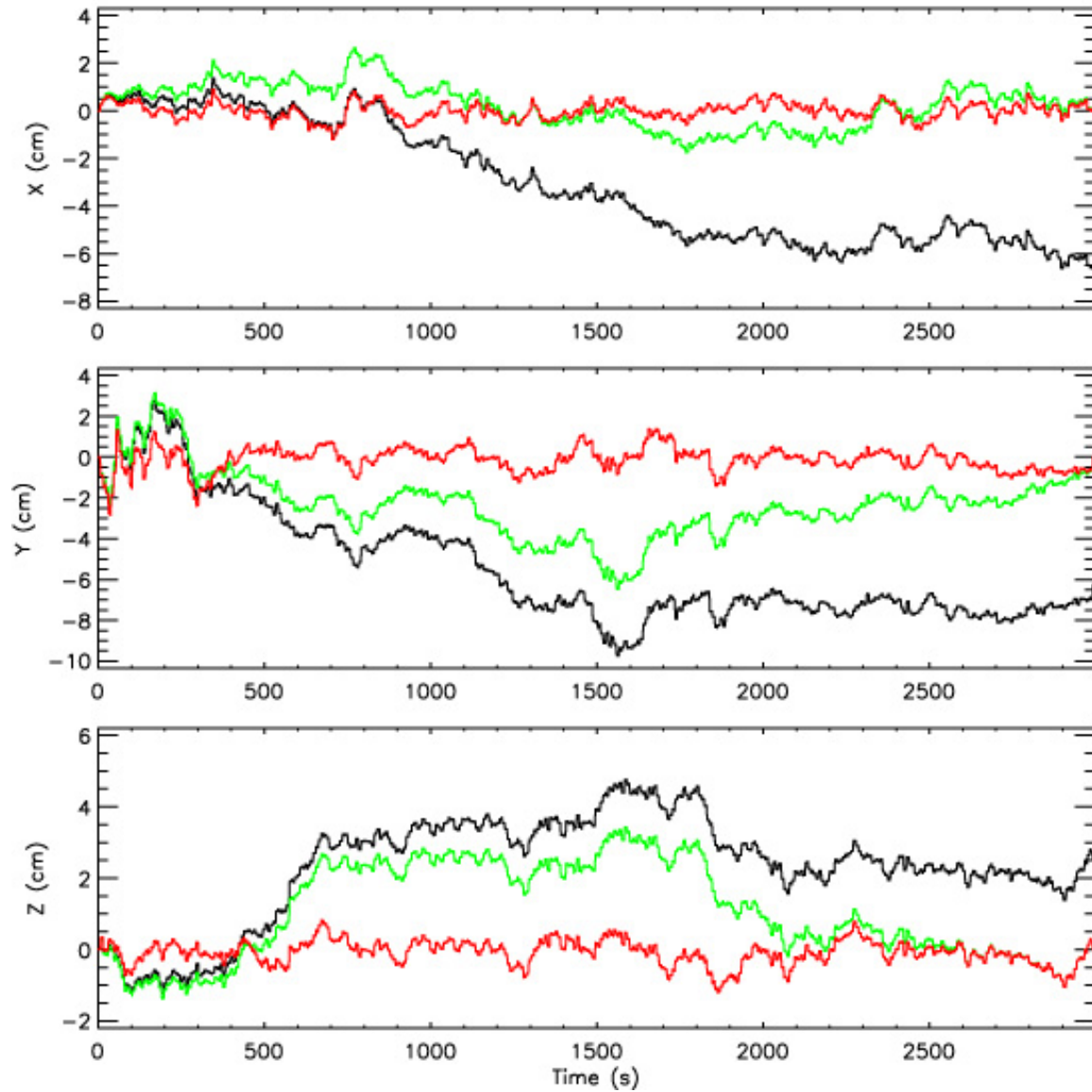


**Figure 62:** The estimated position components in the Earth frame obtained by integrating the corresponding compensated velocity components of Figure 61. The black curves represent direct integrations, with initial positions of zero being the only assumptions made; the green curves are the result of forcing the final positions to be zero as well, with linear corrections applied between both ends; and the red curves are the result of forcing every 25<sup>th</sup> update (200 seconds) to be zero, with linear corrections applied between each of these.

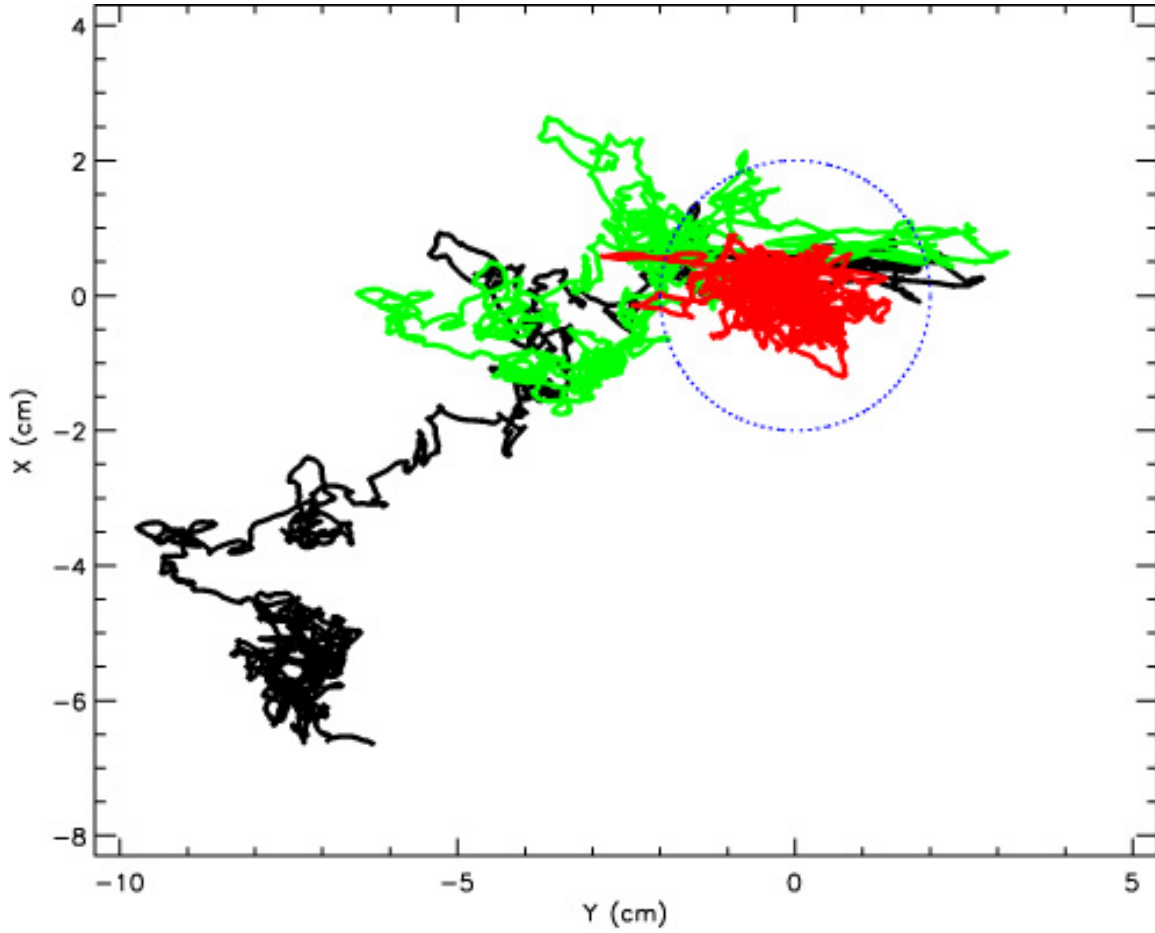


**Figure 63:** The estimated X and Y positions of Figure 62 plotted against one another, showing the deviations from the true (0,0) position. The blue circle shown has a radius of 2 cm about the true position. The same color coding used in Figure 62 is retained here.

### *The Unconstrained Moving IMU*

Again, consider the same IMU 3D motion data as before. Analogous to the static IMU case, the evaluation of the full compensation of the acceleration vector via (16) reveals the presence of a residual bias in the z-component. As shown in Figure 64, the magnitude of this bias is similar to that observed in Figure 59, but not identical.

The source of the residual bias is evident. Recall the assumption made (i.e.  $\mathbf{b}_a(0) = \mathbf{0}$ ) following the introduction of (27) so that the linear regressions on zero velocity update acceleration data with identical IMU orientation resulted in  $\mathbf{c}_a \equiv \mathbf{R}_{e \rightarrow b}(0)\mathbf{g}$ . Clearly from the examples that immediately follow this,  $|\mathbf{c}_a| \neq g$ , even though the physics require it. A simple way to resolve this inconsistency is by requiring that  $\mathbf{b}_a(0) \neq \mathbf{0}$  such that  $|\mathbf{c}_a - \mathbf{b}_a(0)| \equiv g$ . However, while this simple method should directly account for the residual bias discussed above, it does not.

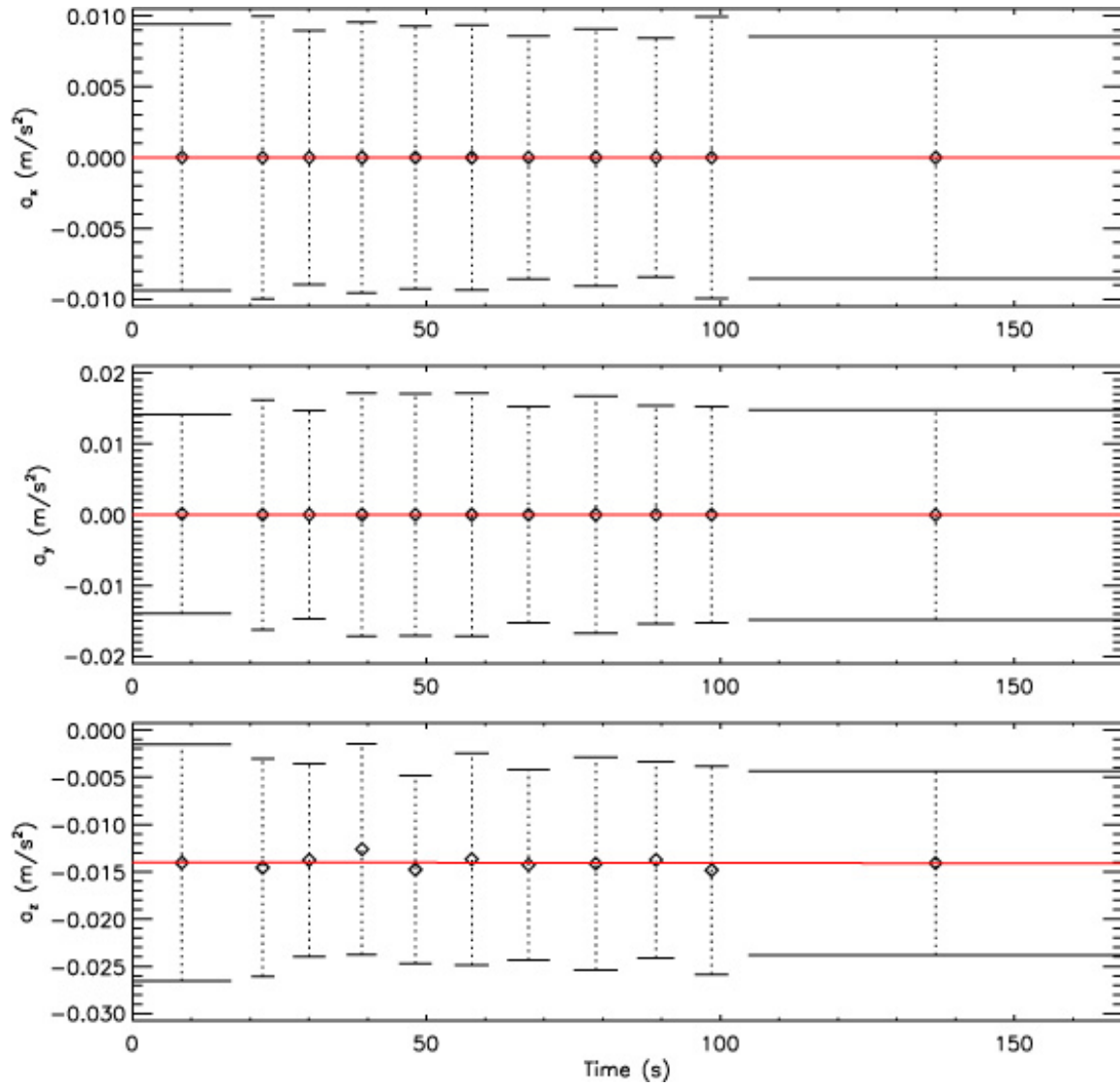


**Figure 64:** The mean and standard deviation of the compensated acceleration components over the zero velocity updates, for the case of back and forth 3D sweeping motion of the IMU between two well-defined fixed points. The zero velocity updates take place at the two fixed points

The velocity vector obtained by integrating the fully compensated acceleration vector (i.e. the compensated acceleration vector obtained via (16) minus any residual biases) is shown in Figure 65. Again, since the velocity is, by definition, zero during zero velocity updates, the integration process is only carried out between updates. As before, the results of the integration process between updates will diverge from what they should be by the time the subsequent updates are reached. The magnitudes of these divergences differ from the static IMU case by about a factor of ten (c.f. Figures 60 and 65).



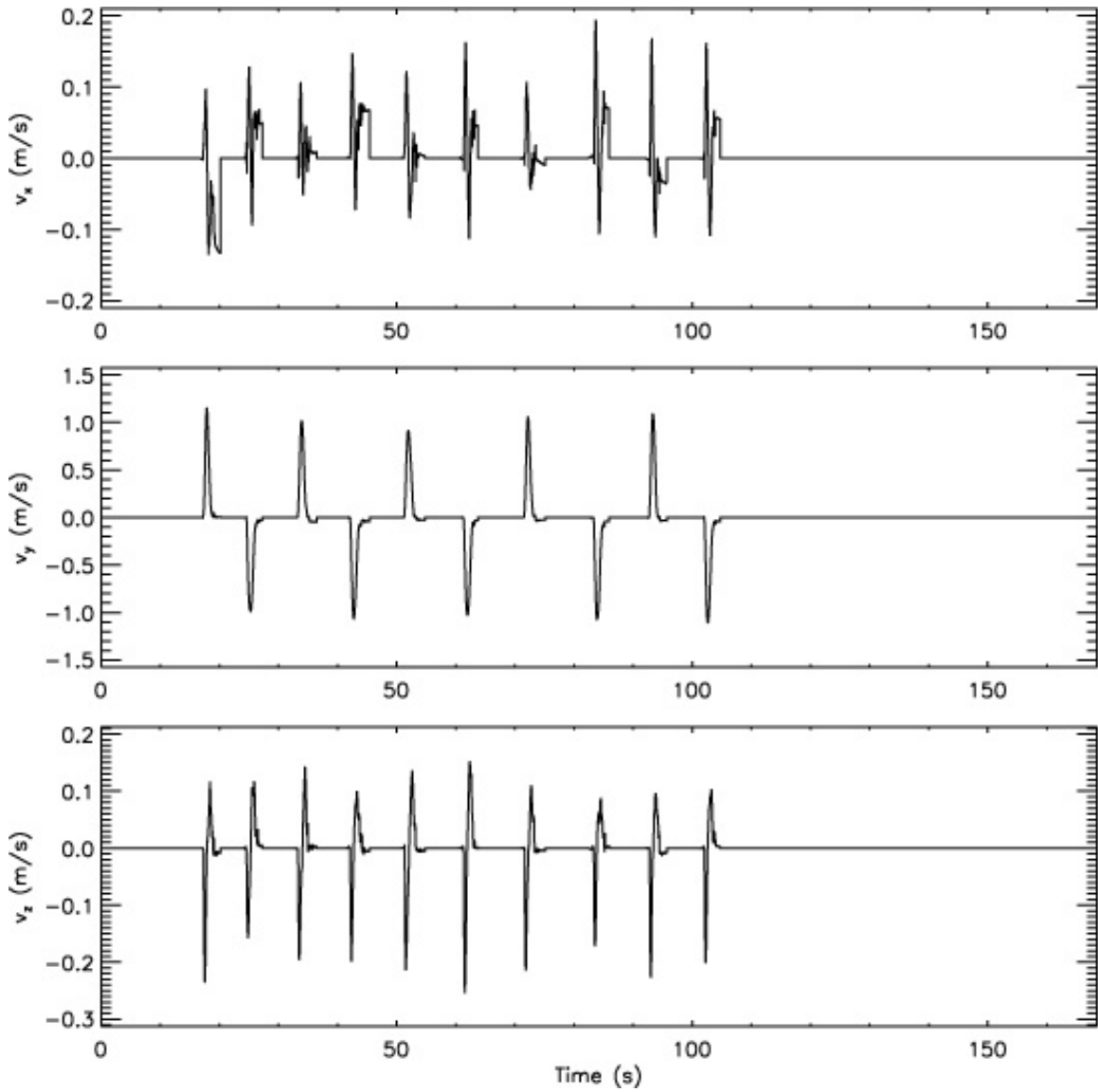


**Figure 65:** The velocity components obtained by integrating the corresponding fully compensated acceleration components between the zero velocity updates, for the case of back and forth 3D sweeping motion of the IMU between two well-defined fixed points. By definition, the velocity is zero during the zero velocity updates. The fully compensated acceleration components used here have had the residual trends, shown in Figure 64, subtracted from each component, and have also been transformed from the IMU body frame to the Earth frame.

The compensated velocity vector components are shown in Figure 66. As before, the compensation is obtained by removing linear trends between the zero velocity updates. This step ensures that the integrated final velocities between updates agree with the subsequent update velocities. Integration of these compensated velocities result in the estimated positions represented in Figures 67 and 68. Similar to the static IMU case, three different outcomes of the estimated positions are considered: one where no assumptions other than an initial position of zero is made (black curves); one where the additional assumption that we return to the initial position at the end is made (green curves); and one where the assumption is made that we return to the initial position at every other zero velocity update (red curves).



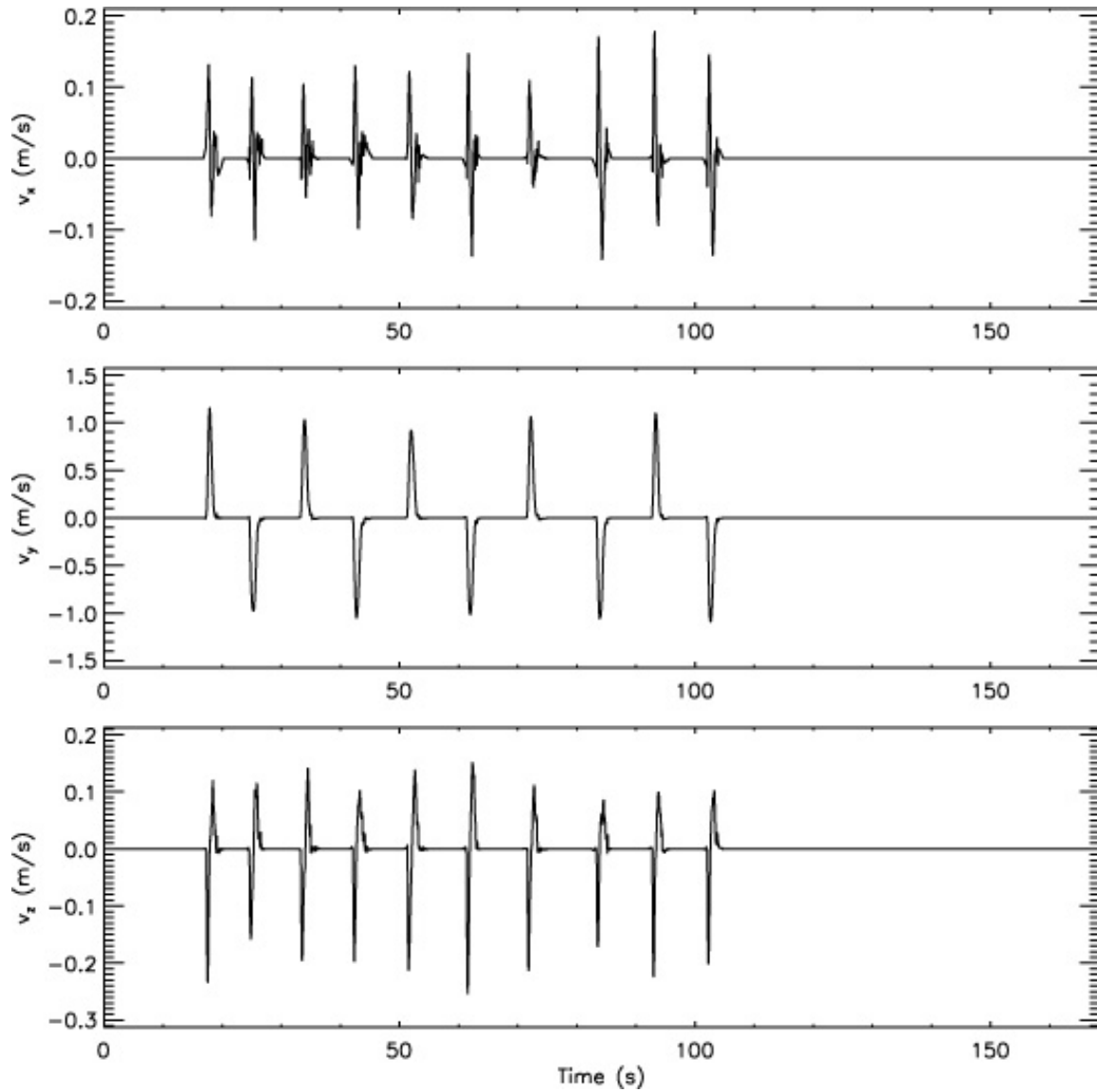


**Figure 66:** The velocity components of Figure 65, but with linear trends subtracted between zero velocity updates so as to remove any existing discontinuities.

The fixed end points of the 3D sweeping motion are represented in Figure 68 by blue circles of 2 cm radius. It is clear from the top panel of Figure 68 that systematic trends in both the  $x$  and  $y$  positions exist. However, even after applying the evermore restrictive zero position update assumptions (i.e. lower two panels), the project goal of cm level positional accuracy is not being met. Even with position updates between each back and forth sweep (red curves) the location accuracy drifts off by several centimeters over the course of the sweeping motion.

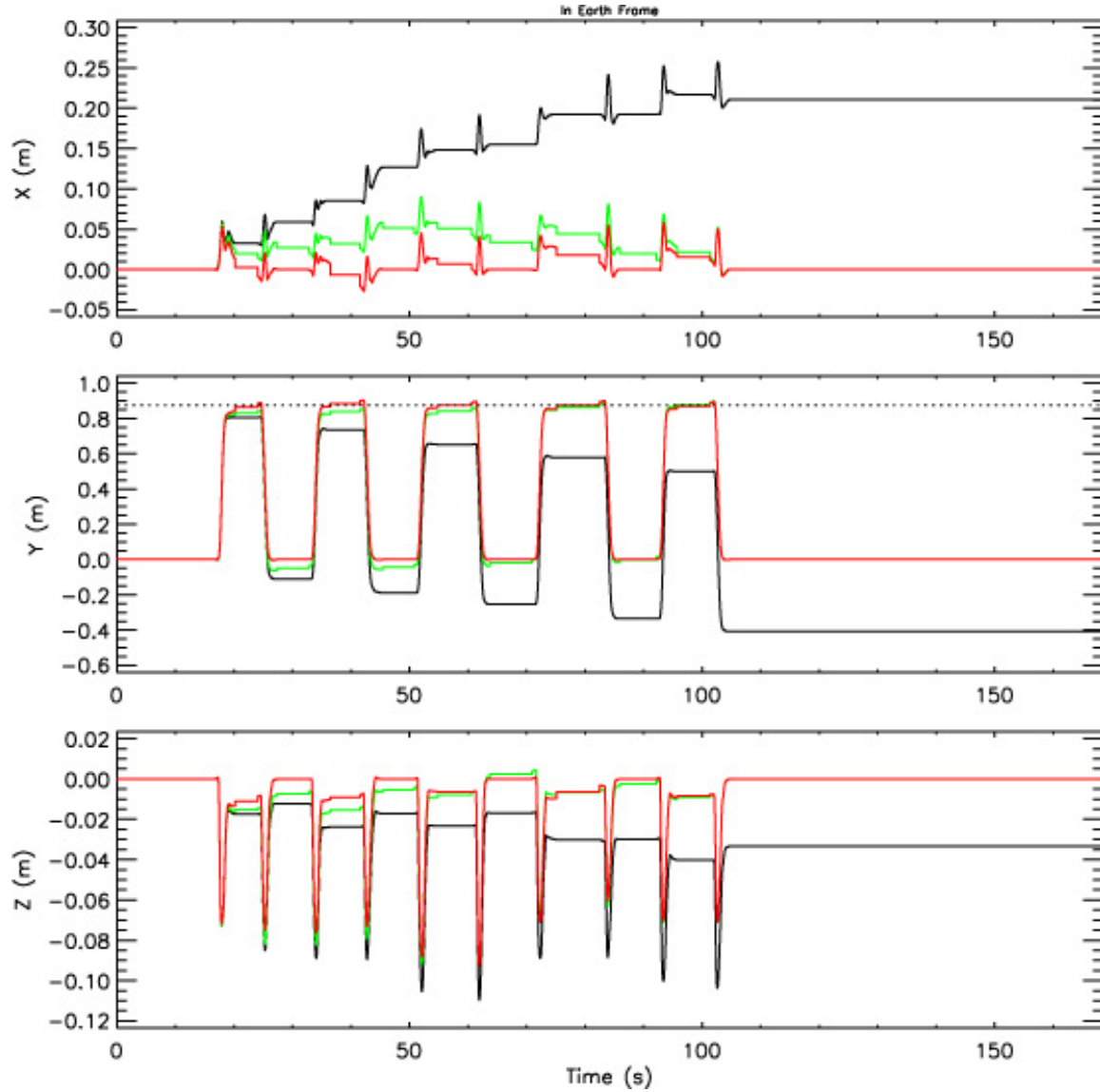


**Figure 67:** The estimated position components in the Earth frame obtained by integrating the corresponding compensated velocity components of Figure 61. The black curves represent direct integrations, with initial positions of zero being the only assumptions made; the green curves are the result of forcing the final positions to be zero as well, with linear corrections applied between both ends; and the red curves are the result of forcing every other update position to be zero, with linear corrections applied between each of these.

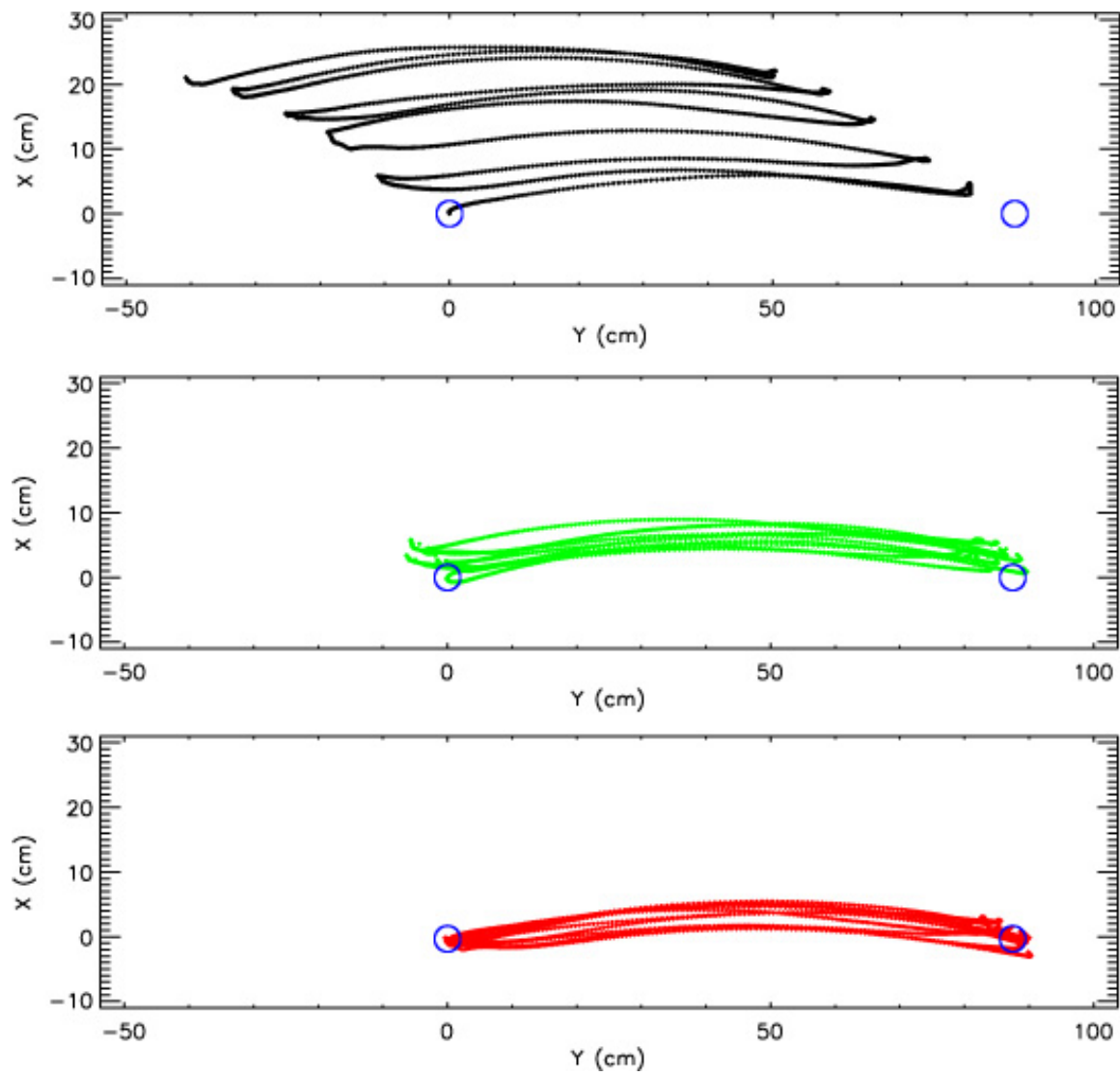


**Figure 68:** The estimated X and Y positions of Figure 67 plotted against one another, showing the deviations from the two fixed points (blue circles) about which the sweeping takes place. The blue circles shown have radii of 2 cm. The same color coding used in Figure 67 is retained here.

## 7. SAINT Tests

Although we had good results in determining sensor location from the Crossbow IMU data for 2D motion, the results for 3D motion were discouraging. We believe that this is because of unacceptable levels of noise and drift in the Crossbow angle rate measurements. Accurate determination of the IMU's orientation is vital to getting accurate position information because even a very small error in angle can introduce erroneous gravity contributions to the X and Y accelerations, which in turn integrate up to large position errors. A higher quality Honeywell HG1900 IMU was integrated with the EM61-HH by ENSCO under ESTCP project MM-0604. It is referred to as the Small-Area Inertial Navigation Tracking or SAINT system. We collaborated with MM-0604 to evaluate whether or not the SAINT could provide sufficiently accurate sensor position information to support reliable UXO/clutter discrimination. Results are reported in [9].

### 7.1. The SAINT system

The SAINT system is shown in Figure 69. It comprises a Honeywell HG1900 IMU, Leica digital magnetic compass and embedded CPU to record the data to compact flash card. The EM61-HH data is collected by the standard Geonics Allegro logger. Calculation of sensor location from the IMU is done in post-processing.

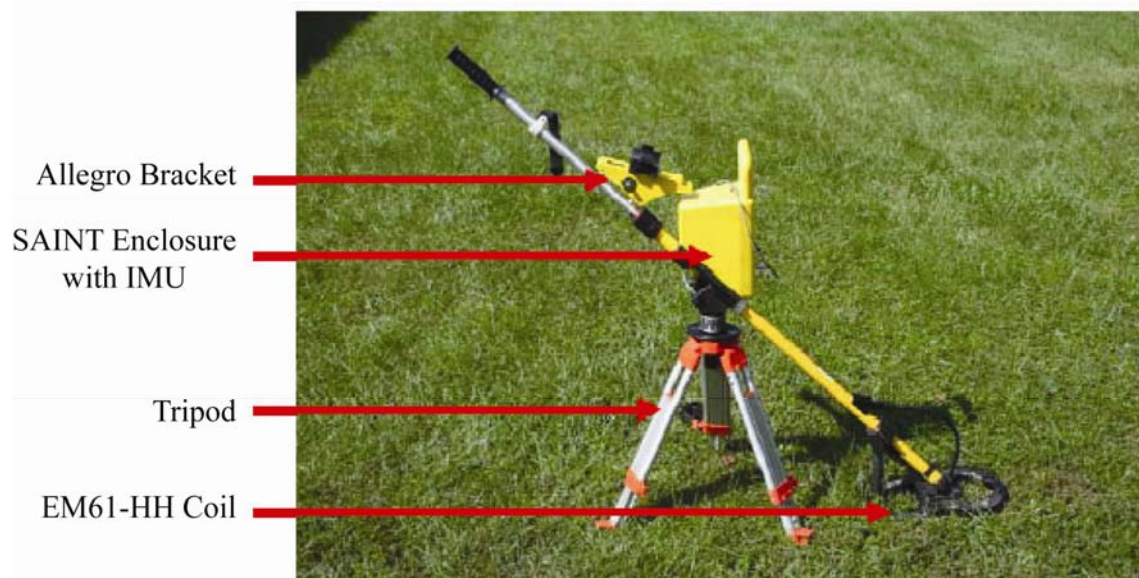


**Figure 69:** SAINT System combining EM61-HH and Honeywell HG1900 IMU.

The HG1900 is a more expensive unit (~\$10K vs. ~\$4K), but its angular rate random walk spec ( $0.1 \text{ deg/hr}^{1/2}$ ) is substantially better than that of the Crossbow IMU400CC-100 ( $2.25 \text{ deg/hr}^{1/2}$ ). It also has a significantly higher bandwidth than the Crossbow unit (600 Hz vs. 135 Hz). Figure 70 shows simultaneous angle rate data from the Crossbow unit and the Honeywell unit. They were mounted side-by-side on the shaft of the EM61-HH. The data in Figure 70 were collected as the sensor was being swept back and forth. Several things are apparent in these data: the Honeywell data appears smoother (higher bandwidth) and less noisy than the Crossbow data, and there appears to be a bit of drift with the Crossbow unit, especially in the Y-axis angle rate.

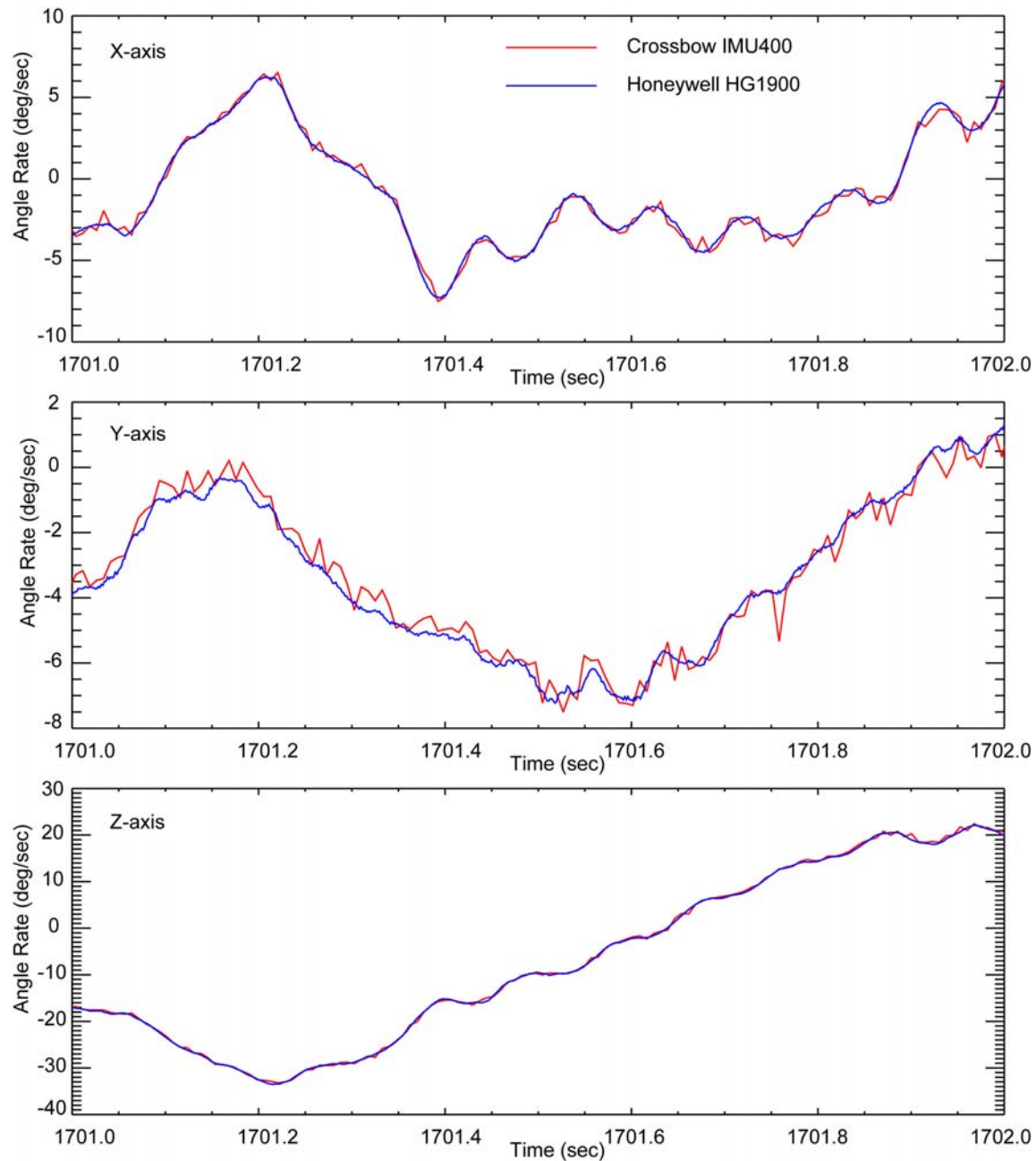


**Figure 70: Simultaneous angle rate data from Crossbow and Honeywell IMUs.**

## 7.2. Test Setup

As part of ESTCP project MM-0604 the SAINT IMU/EM61-HH was used to interrogate a selection of the Calibration Grid buried inert ordnance at the Aberdeen Proving Ground Standardized Test Site. The EM61-HH sensor was swept back and forth over known object locations and positioning for this 3-D sensor trajectory was measured using the Honeywell unit. We set up the Arcsecond system to provide ground truth on a subset of this data. For the data

where the EM61-HH sensor was simultaneously tracked with the Arcsecond system and the IMU, we found that typically the agreement between the IMU-derived sensor positions and the Arcsecond ground truth was good to within 1-3 cm.

The Aberdeen Calibration Grid is set up into rows A through K and columns 1 through 15 increasing from the NE corner of the grid. The smaller buried items are separated by 2 meters. For this test, a selection of items at shallower depths was interrogated, because of the limitations on the EM61-HH's detection of deep objects and the overly challenging depths used on the Calibration Grid. The items covered were 20mm, 40mm grenade, 57mm, 60mm mortar, 2.75 inch rocket warhead, 81mm mortar, 105mm, 155mm, and a shot-put. For the most part, three examples of each item were interrogated using only the ENSCO Honeywell system. Each interrogation over a given object was repeated at least three times, resulting in three independent data sets over each object. A 20mm at the grid location A3 was measured repeatedly with both the IMU and the Arcsecond system. In this case, five measurements were taken in the morning and then five more in the afternoon.

The Arcsecond system that we used included a set of four fixed transmitter stations and the four receivers attached to the EM61-HH. After a calibration set up, the system collects data to track the EM61-HH coil head in 3-D along with orientation angles of yaw, pitch, and roll. The actual full trajectory at a 20 Hz data rate is only available in post-processing of the receiver measurements. The current post-processing only provides the trajectory in a local Arcsecond frame of reference based on the location of the fixed transmitters. In order to map the Arcsecond data to either the local APG grid or to UTM coordinates a surveyed point in the northeast corner of the site and a set of known grid points were measured with the Arcsecond system.

The ENSCO/Honeywell inertial system integrates measurements from the HG1900 IMU. The integration starts and stops from a given "zero point". All data is relative to this zero point. The direction of the ENSCO local coordinates is determined by the Leica electronic compass included in the system. In order to interrogate all of the cells across the site, four different zero points were used. To translate from ENSCO's local coordinates to Arcsecond's, these zero points were measured with the Arcsecond. The IMU raw data is collected at 600 Hz. After post-processing this data to an actual trajectory (x, y, z, yaw, pitch, and roll), ENSCO down sampled the position results to 20 Hz. The ENSCO data was provided in a positive z pointing down coordinate system and had to be converted to match the upward z pointing system used by the Arcsecond and our EM fitting algorithms.

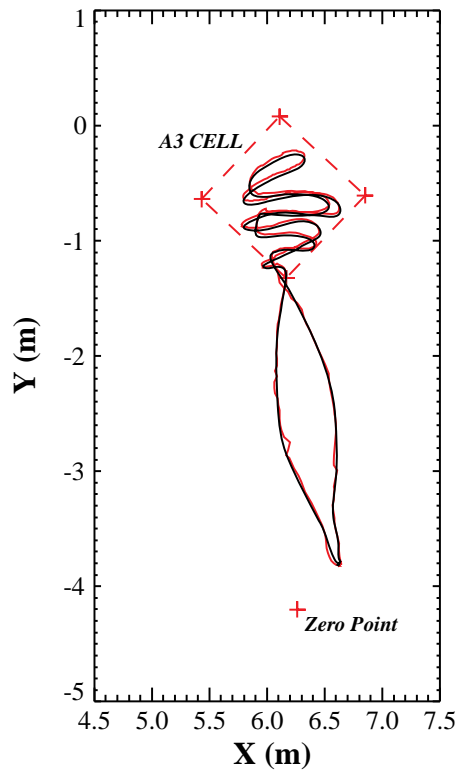


**Figure 71:** EM61-HH coil head trajectory over A3 cell in ArcSecond coordinate system. IMU-derived trajectory is plotted in black and ArcSecond trajectory in red.

### 7.3. Trajectory Comparisons

To compare the two measured trajectories, the ENSCO data was shifted in time, shifted in space, and rotated to best match the Arcsecond trajectory. The time shift is due to the two different data acquisition clocks used by the systems. The spatial shift was based on the ENSCO zero point measured by the Arcsecond. For the ten common data sets, roughly the same rotation angle provided a good match between the two sets of data. The average angle was 41.2 degrees counter-clockwise to match the ENSCO data to the Arcsecond. The angles ranged from 40.1 to 42.05 with a standard deviation of 0.6. Figure 71 plots a comparison of the two trajectories in the X, Y plane for one of the joint data collections over the A3 cell location. The black curve is from the ENSCO system and the red is from the Arcsecond. The red plus signs are measured grid and zero point locations.

To match the UTM coordinate system, a variety of local grid points was measured by the Arcsecond. Based on these, the Arcsecond coordinates must be rotated 35.9 degrees clockwise to align with true north. From this, the ENSCO coordinates needed to be rotated 5.3 degrees counter-clockwise to match UTM.

Using the average rotation angle and zero point, Figure 72 plots the ENSCO-only trajectories from the same zero point. This time the data is in the local grid coordinates relative to the northeast corner of the A1 cell. The red curve is from a common Arcsecond/ENSCO trajectory. The black curves are all from ENSCO only data collections. The red plus signs are fixed grid points measured by the Arcsecond system. For these ENSCO only trajectories, there appears to



be some further rotation and possibly shift required to get them to match the actual measured cell location. Figure 73 plots similar results from two other zero points.

Figures 74 and 75 graph comparisons of joint ArcSecond/ENSCO trajectories in more detail. In 74(a) and 75(a), the ArcSecond trajectory is plotted in red and ENSCO is in black. The other graphs plot (b) the horizontal and (c) vertical distances between the two trajectories as a function of time. In Figure 74 there is very close agreement and in Figure 75 there is not. The Arcsecond system typically jitters about the true trajectory, and occasionally spikes way off when one or more receivers are blocked. However, its absolute positioning over time tends to be very good. The ENSCO data plots a very smooth trajectory, but appears to drift off from the Arcsecond trajectory. Out of the ten joint trials, eight of them drifted off on the order of one to three centimeters in the horizontal similar to the example in Figure 74. For two of the trials, the ENSCO trajectory drifted way off, and the extent of the drift varied over time as in Figure 75. Comparing the orientation angles between the two showed similar results with typical differences in orientation being on the order of only several degrees or less. Statistics for the differences in position and orientation of the two trajectories are presented in Table 5 for all ten runs.

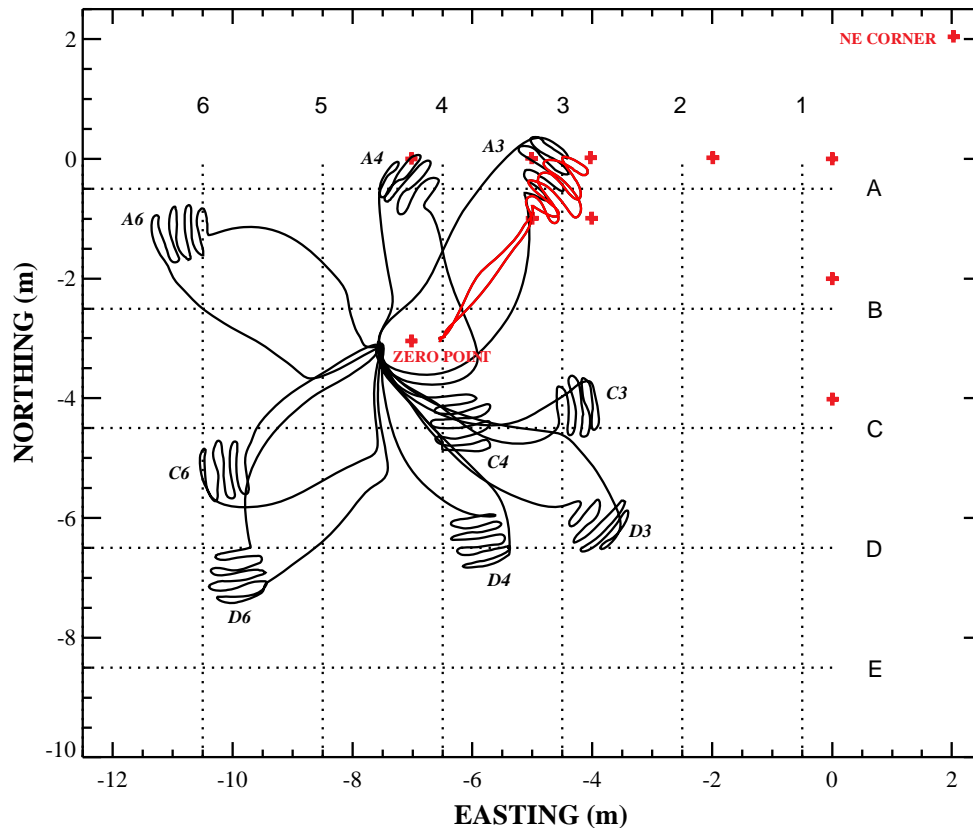


**Figure 72: Different cell trajectories about zero point and relative to APG local grid. Joint ArcSecond/IMU data in red and IMU only data in black.**



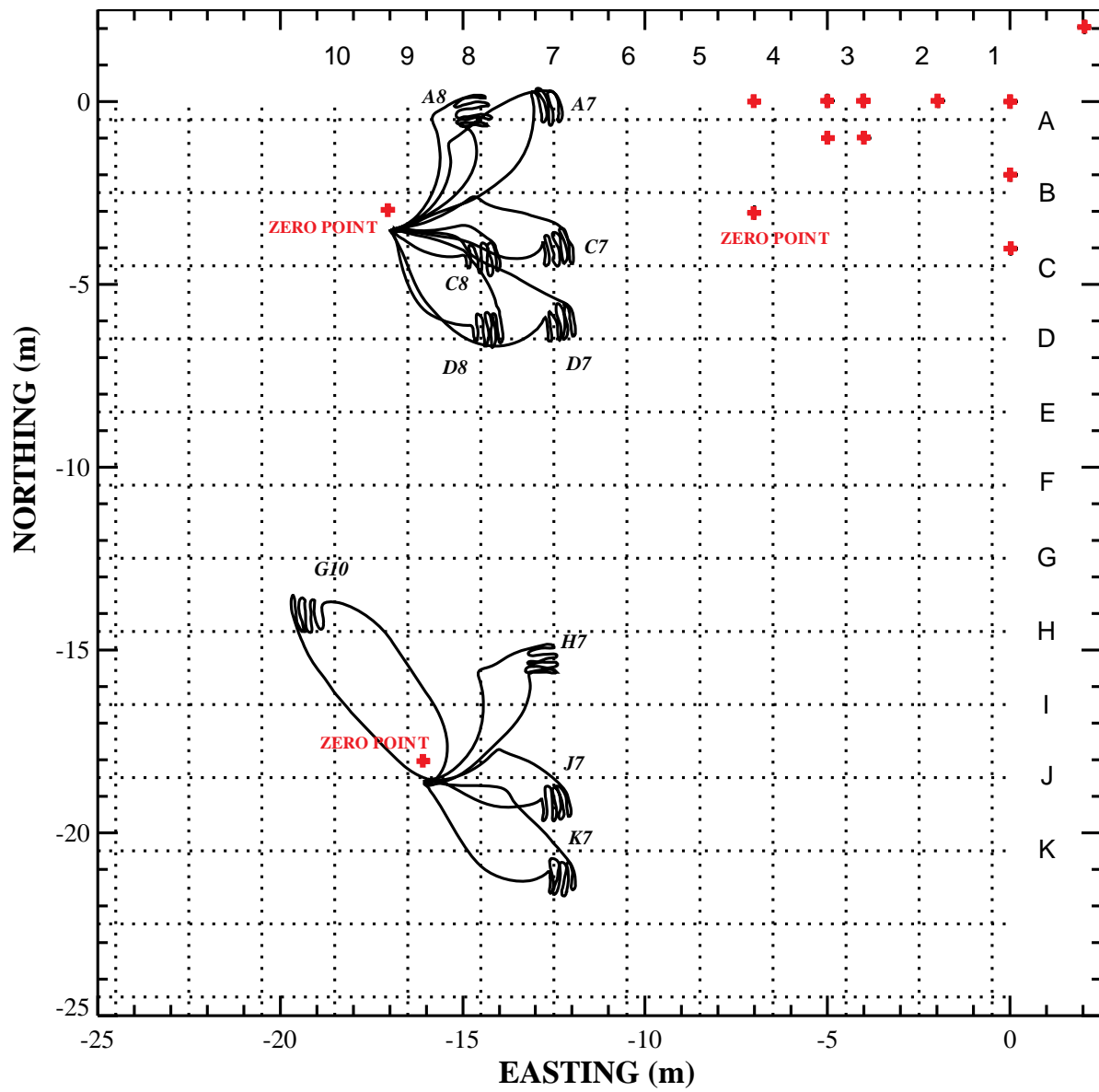


**Figure 73:** Different cell trajectories from IMU only data at other Arcsecond measured zero points. Local grid coordinates.

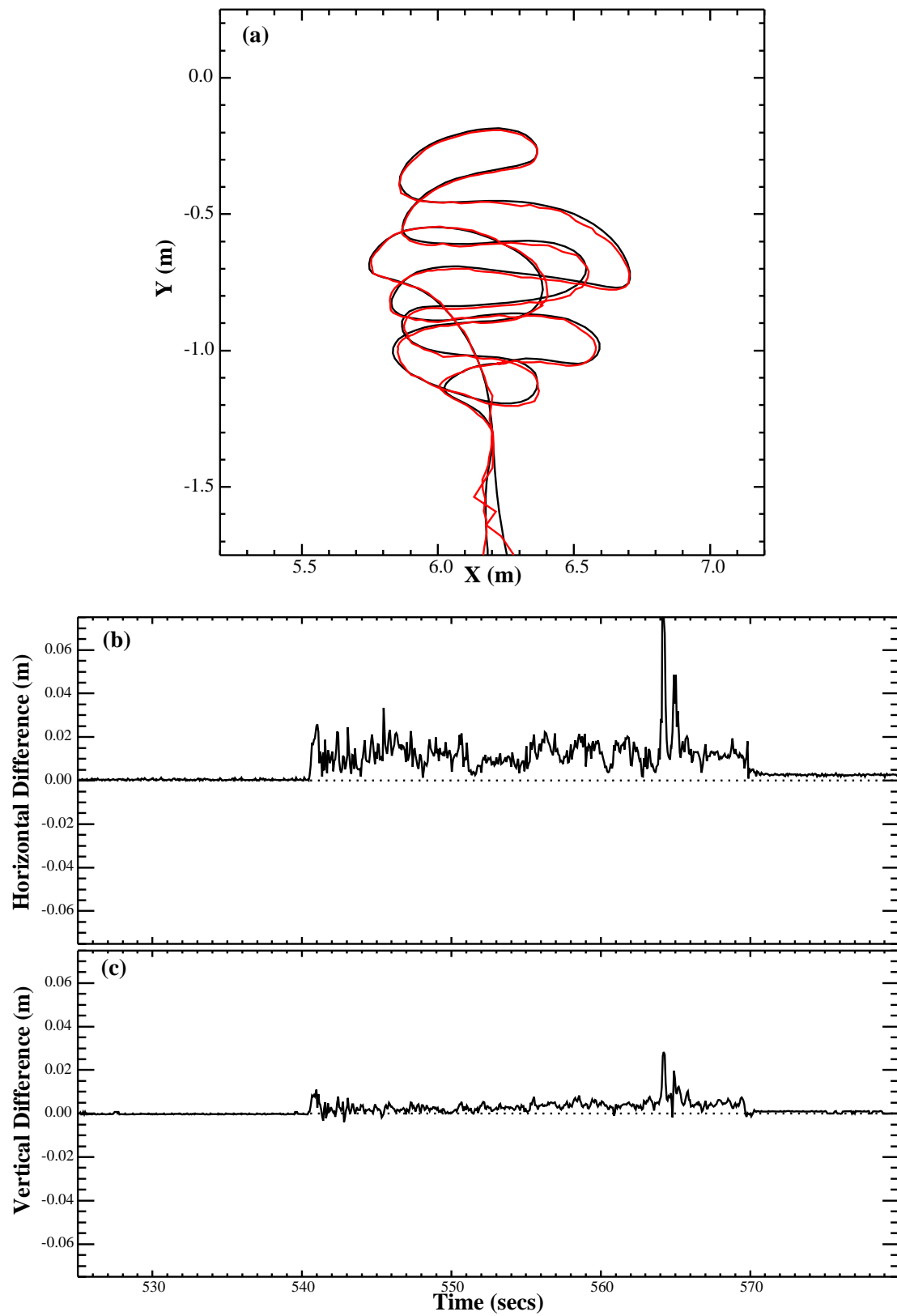


**Figure 74: Comparison of IMU (black) and ArcSecond (red) trajectories. ArcSecond coordinates.**

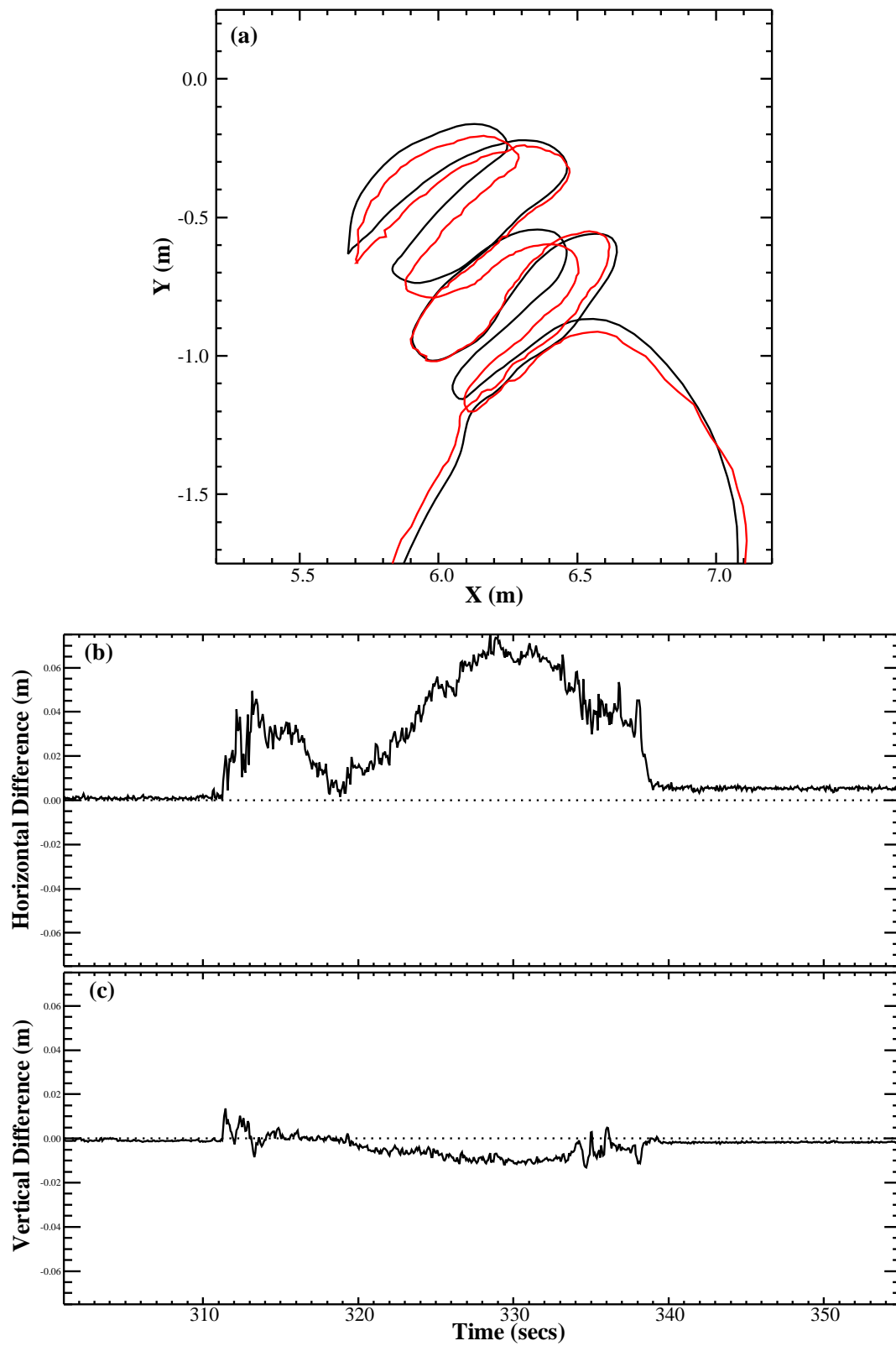


**Figure 75:** Second comparison of IMU (black) and ArcSecond (red) trajectories. ArcSecond coordinates.

		Difference in X (m)	Difference in Y (m)	Horizontal Difference (m)	Difference in Z (m)	Difference in Yaw (degs)	Difference in Pitch (degs)	Difference in Roll (degs)
Run #1	Mean	-0.002	0.001	0.017	-0.005	1.96	-2.41	-1.37
	Standard Deviation	0.018	0.013	0.014	0.006	0.86	0.61	0.47
Run #2	Mean	-0.001	-0.006	0.013	-0.003	1.83	-2.45	-1.33
	Standard Deviation	0.011	0.008	0.009	0.003	0.74	0.40	0.35
Run #3	Mean	-0.004	0.044	0.046	-0.004	1.62	-2.56	-1.33
	Standard Deviation	0.007	0.020	0.017	0.002	0.62	0.31	0.27
Run #4	Mean	-0.002	0.022	0.027	-0.003	1.58	-2.46	-1.31
	Standard Deviation	0.012	0.011	0.007	0.003	0.60	0.32	0.31
Run #5	Mean	-0.003	0.025	0.028	-0.002	1.65	-2.49	-1.37
	Standard Deviation	0.007	0.013	0.009	0.002	0.73	0.27	0.28
Run #6	Mean	-0.003	0.017	0.020	-0.003	0.79	-1.13	-0.62
	Standard Deviation	0.007	0.009	0.008	0.003	0.64	0.27	0.39
Run #7	Mean	0.000	0.000	0.008	-0.005	0.85	-1.04	-0.66
	Standard Deviation	0.007	0.007	0.005	0.002	0.41	0.19	0.21
Run #8	Mean	-0.006	0.026	0.028	-0.002	0.73	-1.21	-0.71
	Standard Deviation	0.007	0.011	0.010	0.005	0.69	0.56	0.39
Run #9	Mean	0.000	-0.001	0.012	-0.004	0.94	-1.09	-0.62
	Standard Deviation	0.013	0.010	0.012	0.003	0.85	0.38	0.52
Run #10	Mean	0.011	-0.024	0.039	0.005	1.45	-1.14	-0.66
	Standard Deviation	0.027	0.022	0.021	0.005	0.67	0.25	0.29
OVERALL	Average Mean	-0.001	0.010	0.024	-0.003	1.341	-1.798	-0.997
	Average Standard Deviation	0.012	0.012	0.011	0.003	0.680	0.356	0.347

**Table 5: Differences between ArcSecond and IMU Trajectories.**

## 7.4. Inversion Results

The EM61-HH data was collected on the standard Allegro handheld computer provided by Geonics. The data was collected at a data rate of 15 Hz. The Geonics handheld has a second COM port to collect standardized GPS data. ENSCO is working on using this port to provide time stamping between the IMU data and the EM61-HH data. However, at the time of these tests this was not working properly. There was no attempt at all to synchronize the ArcSecond data to the Geonics data. The EM61-HH data was manually shifted to within a second of the other systems, and we accounted for the residual time difference by adding it in as a fit parameter in our EM inversion routine.

The basic electromagnetic induction response model involves a simple dipole response [6]. Inversion of this model solves for the object's location, object orientation, and the magnetic polarization response terms. The polarization terms, referred to here as  $\beta$ 's, determine the strength of the object's induced response along the object's physical axes. It is these terms that allow for discrimination between buried ordnance and other metallic clutter. For elongated ferrous ordnance items such as a projectile or mortar, there is one large, primary  $\beta$  response along the item's long axis and two smaller, secondary responses transverse to this,  $\beta_X > \beta_Y = \beta_Z$ . Accurately determining these parameters from model-based inversion is limited by the signal-to-noise ratio (SNR) of the sensor data and by the positioning accuracy of the sensor trajectory.

Simulations performed for the SERDP/ESTCP Geolocation Workshop showed that positioning accuracy of better than 1 centimeter is required to invert  $\beta$ 's with less than 20% error.

There are other complications in inverting the EM61-HH data combined with the IMU trajectory. Over minutes of data collection, the zero level of the sensor will change. The data collected here starts with the sensor on a metal tripod with an unknown offset. It then moves back and forth over an object perhaps reaching zero at points, perhaps not. Because of this, an offset parameter has been added to the data inversion. Also, the EM data is not synchronized with the IMU data. A time difference term is yet another fit parameter.

Besides the fit parameters, the inversion algorithm returns a reduced chi-squared value for the fit and a squared correlation coefficient  $R^2$  between the best model fit and the measured data. The dipole fit error is expressed as  $\sqrt{(1-R^2)}$ . The percentage fit error grows with both low SNR signals and with poor positioning. For the ten separate measurements made over the A3 cell, the EM61-HH data was inverted first using the ArcSecond positioning and then using the IMU positioning. Figure 76 plots the fit error results for one positioning system versus the other using the same EM data. For half of the data, the two systems result in comparable fit errors. For the data sets where the trajectories did not match well, the IMU fit errors are significantly greater.

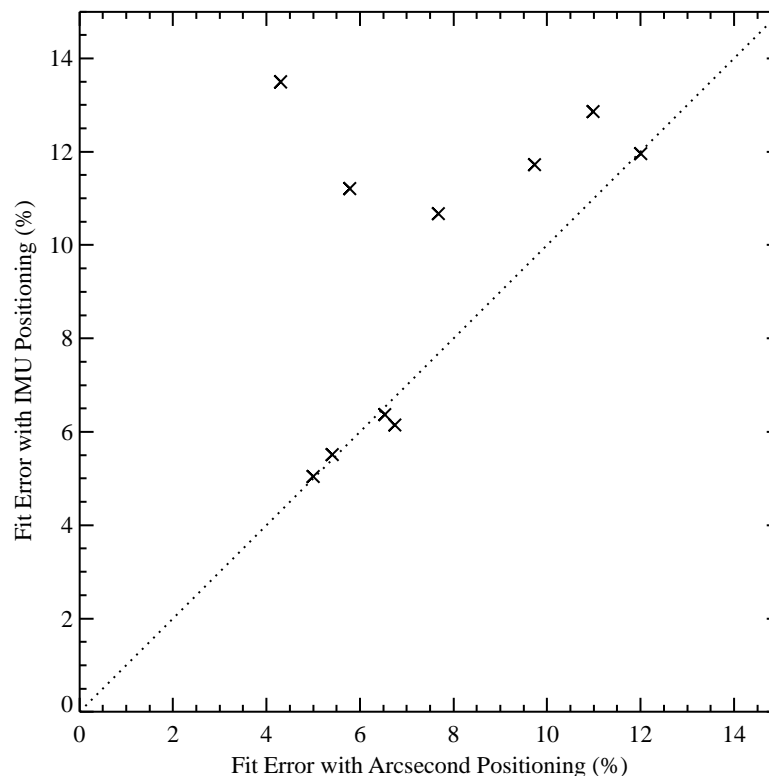


**Figure 76: Fit error comparison between EM data with IMU and ArcSecond positioning.**

Figure 77 plots the spread in the inverted  $\beta$  parameters over all 20 mm measurements. In these plots, the x axis plots the largest  $\beta$  value from the fit. The y axis plots the average (diamond symbol) and the range (vertical line) of the two secondary  $\beta$  values. For axisymmetric objects like the 20 mm, the secondary  $\beta$ 's should be equal and the vertical line should be a dot. The points in 77(a) are from fits using Arcsecond positioning. The mean primary  $\beta$  value is 0.387

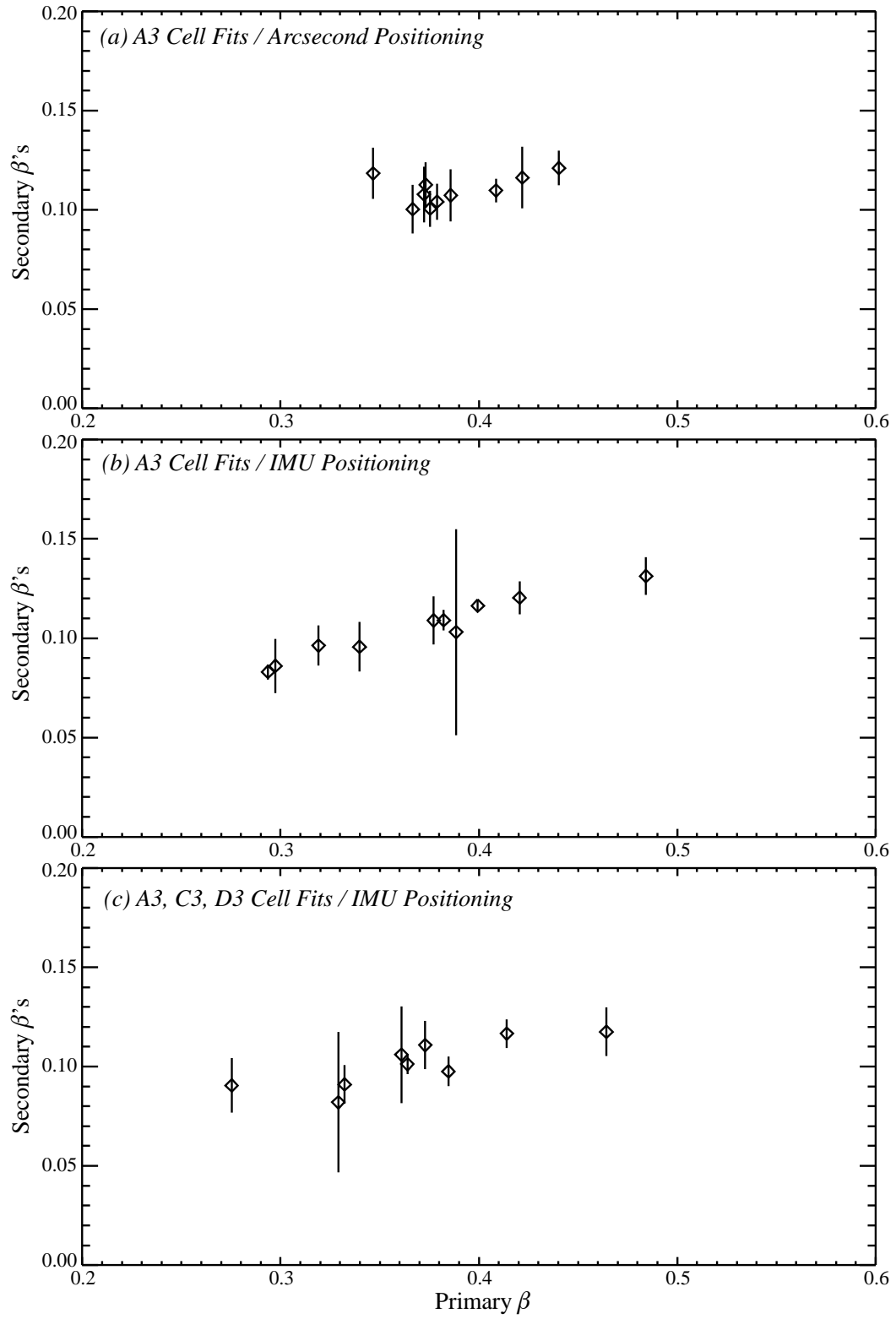
with a standard deviation of 0.028 (7% of mean). The average secondary value is 0.110 with a standard deviation of 0.014 (13%). The same fits with IMU positioning are shown in 12(b). The mean value is 0.370 with a standard deviation of 0.059 (16%). The secondary mean is 0.105 with a standard deviation of 0.024 (23%). The spread in the  $\beta$  fits is roughly twice as great for the IMU positioning. Similar increased spreads in the other object fit parameters (X, Y location and depth) were observed with the IMU positioning. Figure 77(c) plots the fit results for IMU only measurements made over the 20 mm cells: A3, C3, and D3. The results are comparable to 77(b). Figure 78 plots the fit results for data collected over the A4, C4, and D4 cells containing a 40 mm grenade. These results are plotted in black with diamond symbols. For comparison, the 20 mm results are plotted in red. There are comparable spreads in this data, but it is sufficiently small to discriminate between the two items. It should be noted that one fit result is significantly off and that another data set failed to fit successfully.

Figure 79 plots the fit error versus the SNR of the EM61-HH signal from these data sets: joint 20 mm ArcSecond (green X) / IMU (red X), 20 mm IMU only (black diamond), and 40mm grenade IMU only (blue triangle). The general trend is for decreasing fit error with increasing SNR. The solid black curve is a calculated limit for fit error as a function of SNR assuming no position errors. The dotted curves plot the limits assuming position errors on the order of one and two centimeters. The bulk of the fits fall under the one centimeter curve.

The rest of the data collected over other cells on the APG calibration grid had SNR in the range of roughly 0 to 30 dB. With an RMS noise level of ~4 millivolts, this is in the range of a few to approximately 100 millivolts. The inversion algorithm had trouble converging to a solution for data in the 20 to 30 dB range. In some cases, several local minima were found by the fit algorithm.

The majority of the joint ArcSecond and ENSCO IMU positioning data showed agreement in the horizontal sensor head trajectories to be within one to three centimeters (see Table 5). There were two data sets where the ENSCO IMU data was found to drift significantly off from the ArcSecond horizontal positioning. The EM fits resulting from these two systems showed general agreement, with the ArcSecond showing a smaller spread in the fit parameters (7% to 13% variations about the mean response  $\beta$ 's versus 16% to 23%). Even with the larger spread in  $\beta$ 's, the IMU positioned fits are sufficient to discriminate between a 20 mm projectile and a 40 mm grenade. Comparisons of the fit results overall are promising with the bulk of the fit errors falling about theoretical curves indicating roughly one centimeter relative positioning error (figure 79).

There is no current explanation for the two data runs that drifted significantly off. There was nothing indicated in the IMU output to flag them as being poor. The EM fits were of poorer, but not unreasonable, quality (10-14% versus 5-10%). The fit algorithm did have trouble converging for this data and there were several  $\beta$  parameter outliers.



**Figure 77:** Comparison of fitted  $\beta$  polarization parameters on 20 mm cells.

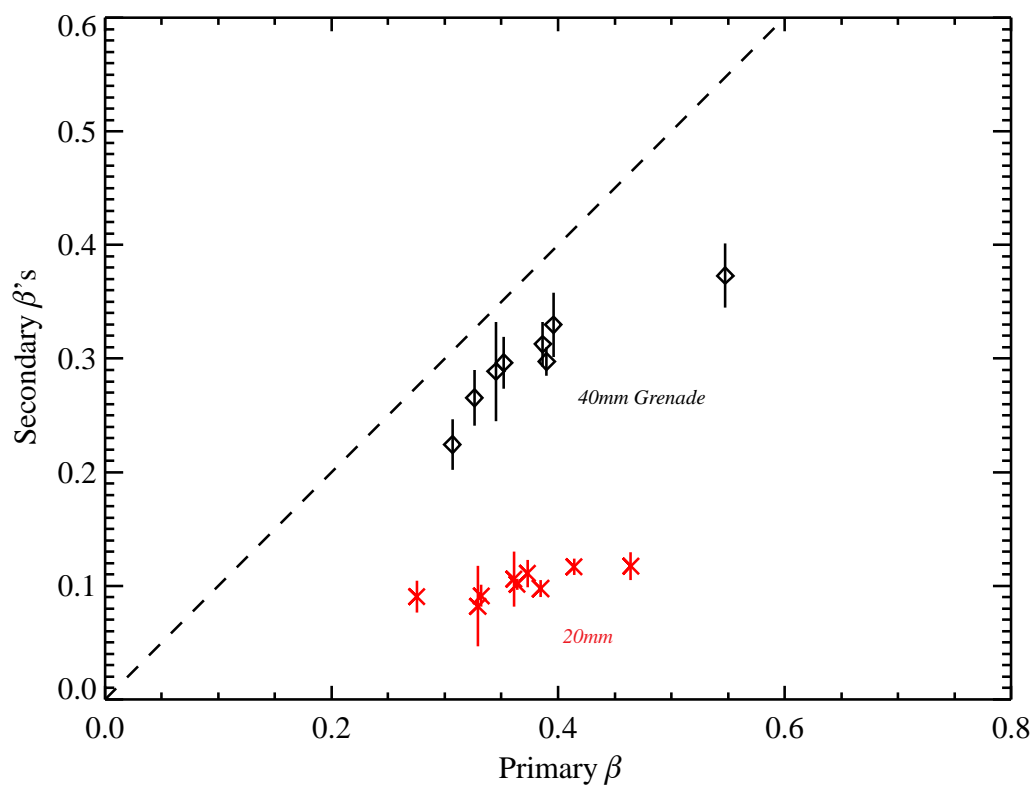


**Figure 78:**  $\beta$  fits of 40mm grenade data compared to 20 mm fits.

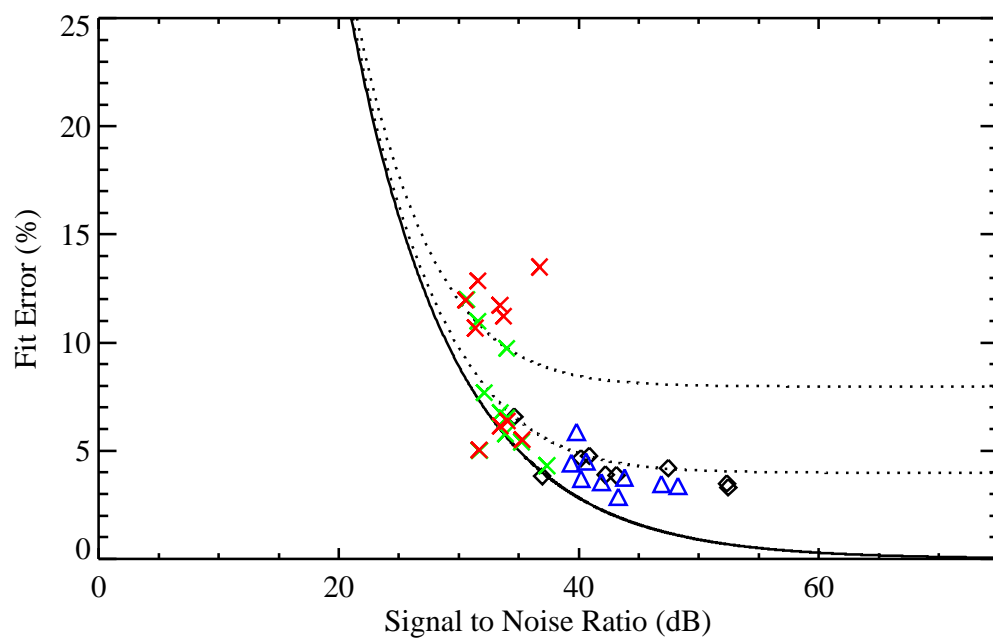


**Figure 79:** Plots of fit error versus EM61-HH signal-to-noise ratio. Curves indicate limits based on 0, 1, and 2 centimeter positioning errors.



## 8. Adaptive Processing – Joint Target/Track Estimation

The analysis reported in the previous section shows that while the Honeywell IMU is capable of providing sub-centimeter sensor positioning accuracy, it does not always do so. As part of this project we have investigated the possibility of including sensor data in the track estimation process. The approach is based on the principle that the best model/data fit occurs when the sensor trajectory is correct. Slight errors in the trajectory degrade the fit quality. The idea is then to assume that the trajectory from the IMU is in error, and allow slight modifications of the trajectory in the EMI inversion process, iterating until the best fit to the data is achieved.

Trajectory errors typically arise because of errors in estimating the biases or initial and final sensor orientation. From §2 we see that the IMU track in the earth-fixed frame between two co-located zero velocity updates can be completely specified by 24 parameters. If  $\delta_{\omega}$ ,  $\delta_a$ ,  $B_{\omega}$ , and  $B_a$  are assumed known and stable (this is the case for the Honeywell IMU), we are left with 12 parameters needed to specify the track via IMU measurements (with the implicit assumption that we start and end with zero velocity updates at the same position). These are:

$A_{\omega}$  - the initial biases in the angular rate measurements (3);

$A_a$  - the initial biases in the acceleration measurements (3);

$\delta\psi_i$ ,  $\delta\theta_i$ ,  $\delta\phi_i$ ,  $\delta\psi_f$ ,  $\delta\theta_f$  and  $\delta\phi_f$  - the uncertainties in the initial and final yaw, pitch and roll angles (6)

By defining a function that accepts these 12 parameters as an input vector and returns a measure of goodness-of-fit, we can use a downhill simplex method (such as AMOEBA, described in section 10.4 of Numerical Recipes in C [10]) to perform a multidimensional minimization of the function. The function uses the 12 input parameters to construct a track from the IMU data, thus associating a position and orientation to each EM61-HH reading, and uses this track information as input data our standard EM Marquardt-Levenberg inversion. The downhill simplex iterates on track parameter hypotheses, and at each step, the EMI inversion gives the best fit target parameters. The correlation squared,  $R^2$ , is computed and  $1 - R^2$  is returned as the goodness-of-fit measure of the function.

Figure 80 shows results of applying the downhill simplex method to adaptively refine the sensor trajectory when the measured trajectory is slightly in error. It is based on simulated EM data for an object with the following characteristics:

$$x_o, y_o, z_o = (1.7, 2.7, 0.25) \text{ m}$$

$$\psi_o, \theta_o, \phi_o = (27, 2, 0)^\circ$$

$$\beta_1, \beta_2, \beta_3 = (2, 0.5, 0.5)$$

The inset diagram shows the true trajectory in black and the input (distorted) trajectory in red. The main plot in Figure 80 shows the RMS difference between the true trajectory and the estimated trajectory as the number of iterations of the downhill simplex estimator increases. The deviation of the initial distorted trajectory from the true trajectory is about 5 cm rms. The search algorithm converges to within about 0.5 cm rms of the true trajectory.

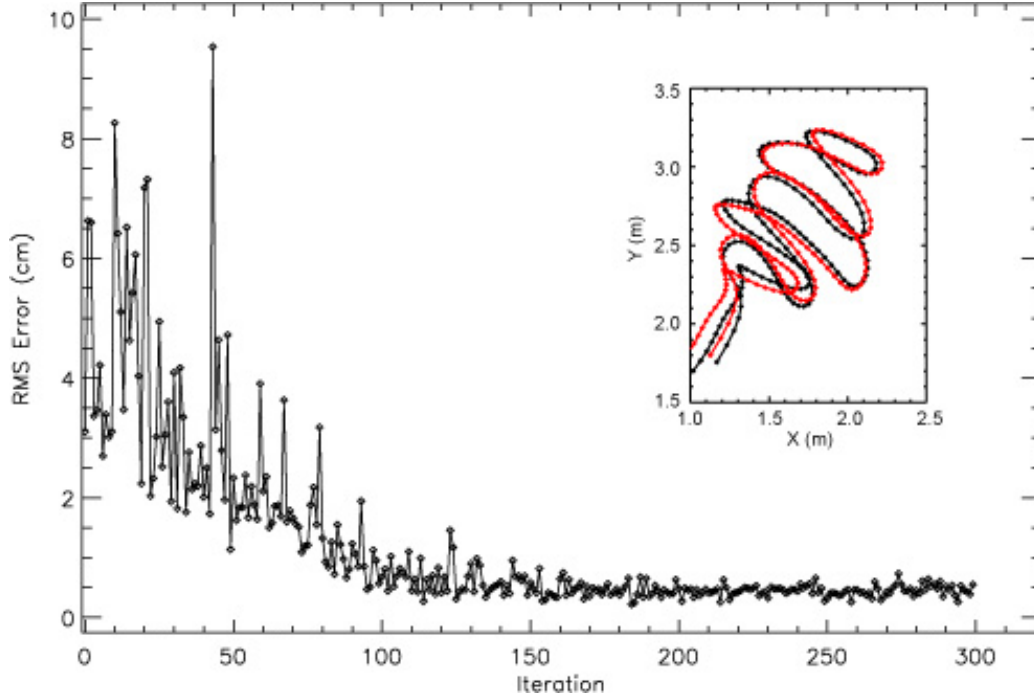


**Figure 80:** Approach to true trajectory using downhill simplex procedure. Inset shows initial distorted trajectory in red and true trajectory in black.

There is no noise in the simulation shown in Figure 80. We have repeated the procedure with added noise of 2 mV rms and 4 mV rms. The peak signal is 70 mV. In both cases the procedure converges. The final track error is also about 0.5 cm rms for 2 mV noise and is about 1 cm rms for 4 mV noise. The estimated target parameters for each case are shown in Table 6. There is a slight degradation in performance with increasing noise. Figure 81 compares the observed variation of dipole fit error with noise with the expected variation. The dipole fit error should be equal to the rms noise divided by the rms signal. It appears that there is a slight (few %) penalty for adaptively refining the track estimate. Note, however, that with the original, distorted track the dipole fit error is 20% in the noise-free case.

noise (mV)	$\beta_1$	$\beta_2$	$\beta_3$	depth (m)	fit error (%)
<b>ground truth</b>	2.0	0.50	0.50	0.250	--
0	1.91	0.48	0.47	0.249	1.7
2	1.96	0.53	0.47	0.252	10.6
4	1.81	0.51	0.34	0.245	20.8

**Table 6:** Target parameters from joint target/track estimation

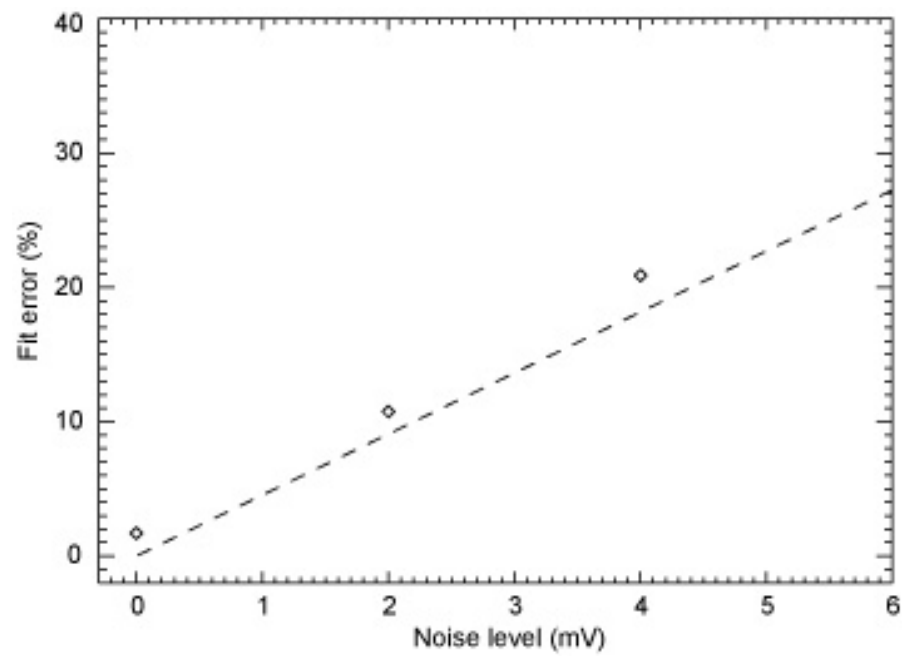


**Figure 82:** Fit error vs. noise level. Dashed line corresponds to perfect sensor track information.

## 9. Conclusions

The objective of this project was to develop an inexpensive, robust way to determine the precise position of a handheld UXO sensor as it is swept about a suspected buried UXO item, enabling the sensor to be used for reliable UXO/clutter discrimination. We were able to demonstrate that a compact (7 cm square), lightweight (<400 gm) Honeywell HG1900 IMU can provide sufficiently accurate positioning to support accurate estimation of target parameters with the EM61-HH sensor. The Honeywell unit costs about \$10K. We also tested a less expensive (~\$4K) unit, the Crossbow IMU400CC-100, but found that it did not provide sufficiently accurate positioning. The major problem with the Crossbow unit appears to be that its angle rate noise and stability are not good enough to accurately track attitude and keep gravitational acceleration from contaminating the horizontal acceleration channels. The angular rate random walk spec for the Crossbow unit is  $2.25 \text{ deg/hr}^{1/2}$ , while the corresponding spec for the Honeywell unit is  $0.1 \text{ deg/hr}^{1/2}$ .

During the course of the project, we found that the response characteristics of the EM61-HH can significantly affect the accuracy of target parameter estimates when the sensor is moving about over the target. This occurs because the sensor output is integrated with an analog filter that both shifts and distorts the sensor's response. We measured the filter response characteristics and included it in a dynamic forward model for the EM61-HH. In order to get discrimination-quality accuracy we have to use the dynamic model when inverting data collected as the sensor is swept about over a target.

In a few of the test cases with the Honeywell we had an uncorrected drift of several cm relative to ground truth provided by a laser (ArcSecond) positioning system. We are able to correct for this sort of drift using an adaptive processing approach which includes the EMI sensor data in the track estimation process. The trajectory errors arise because of errors in estimating the IMU biases. By including the bias parameters in our EM inversion procedure, we can simultaneously determine the best track estimate along with the target parameters (location and principal axis polarizabilities). Simulations using this procedure show that we can reduce 5 cm rms track errors to <5 mm rms.

## 10. References

- [1]. Barrow, B. and H. H. Nelson, "The Effect of Positioning Measurements on Inverting Electromagnetic Induction Data from Unexploded Ordnance," Symposium on the Application of Geophysics to Engineering and Environmental Problems, Denver, Colo., March 4-7, 2001.
- [2]. Barrow, B. and H. H. Nelson, "Effects of Positioning Error on Inverting EMI Data for UXO Discrimination using the MTADS Platform," UXO/Countermines Forum, New Orleans, La., April 9-12, 2001.
- [3]. Bell, T. H., "Handheld Sensor for UXO Discrimination," Partners in Environmental Technology Technical Symposium, Washington, DC, Dec. 3-5, 2002.
- [4]. Miller, J., T. Bell, D. Keiswetter and D. Wright, "Feature-Based Characterization of UXO-Like Targets Using Broadband Electromagnetic Induction", UXO/Countermines Forum, New Orleans, La., April 9-12, 2001.
- [5]. Farrell, J. A. and M. Barth, *The Global Positioning System and Inertial Navigation*. New York: McGraw-Hill, 1999.
- [6]. Bell, T.H., B.J. Barrow, and J.T. Miller, 2001, "Subsurface Discrimination Using Electromagnetic Induction Sensors." *IEEE Transactions on Geoscience and Remote Sensing*, 2001, Vol. 39, No. 6, p.1286.
- [7]. Bell, Thomas, Bruce Barrow, Jonathan Miller and Dean Keiswetter, 2001, "Time and Frequency Domain Electromagnetic Induction Signatures of Unexploded Ordnance." *Subsurface Sensing Technologies and Applications*, Vol. 2, No. 3, July 2001.
- [8]. Barrow, Bruce, Naji Khadr and Thomas Bell, 2006, "Evaluation of Laser Based Positioning for Characterization of EMI Signals from UXO," Symposium on the Application of Geophysics to Engineering and Environmental Problems, Seattle, Washington, April 2-6, 2006.
- [9]. Barrow, B., T. Bell and N. Khadr, 2007, "Inversion of EMI Data Mapped with an IMU Positioning System," UXO/Countermines/Range Forum 2007, Orlando, Florida, August 28-30, 2007.
- [10] William H. Press, Saul A. Teukolsky, William T. Vetterling and Brian P. Flannery, *Numerical Recipes in C*, Cambridge University Press, New York, 1992.

## Appendix A: The Yaw-Pitch-Roll Rotation Sequence

The rotation matrix  $\mathbf{R}_{b_0 \rightarrow b}(t)$  that transforms the initial body frame at time  $t = t_0$  to the body frame at time  $t$  is defined by an ordered sequence of three plane rotations involving the Euler angles  $\psi$ ,  $\theta$  and  $\phi$  (yaw, pitch and roll, respectively).

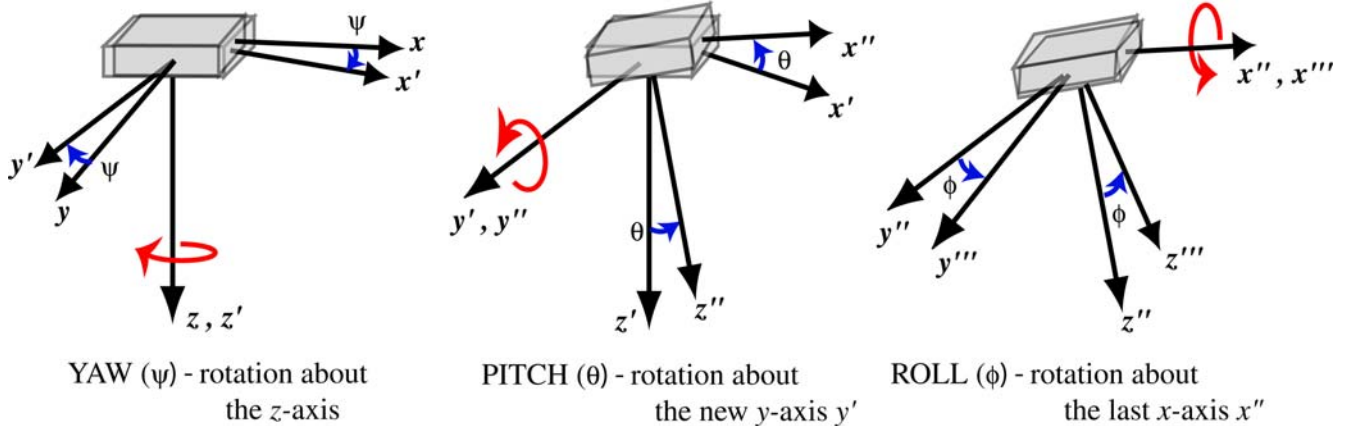


Figure A1: The yaw-pitch-roll rotation sequence.

The yaw rotation aligns the new  $x'$ -axis with the projection of the body  $x$ -axis at time  $t$  into the initial body frame.

$$(A1) \quad \begin{bmatrix} x' \\ y' \\ z' \end{bmatrix} = \begin{bmatrix} \cos \psi & \sin \psi & 0 \\ -\sin \psi & \cos \psi & 0 \\ 0 & 0 & 1 \end{bmatrix} \begin{bmatrix} x \\ y \\ z \end{bmatrix} = \mathbf{R}_\psi \begin{bmatrix} x \\ y \\ z \end{bmatrix}$$

The pitch rotation aligns the new  $x''$ -axis with the body  $x$ -axis at time  $t$ .

$$(A2) \quad \begin{bmatrix} x'' \\ y'' \\ z'' \end{bmatrix} = \begin{bmatrix} \cos \theta & 0 & -\sin \theta \\ 0 & 1 & 0 \\ \sin \theta & 0 & \cos \theta \end{bmatrix} \begin{bmatrix} x' \\ y' \\ z' \end{bmatrix} = \mathbf{R}_\theta \begin{bmatrix} x' \\ y' \\ z' \end{bmatrix}$$

The roll rotation aligns the new  $y'''$ -axis and  $z'''$ -axis with the body  $y$ -axis and  $z$ -axis, respectively, at time  $t$ .

$$(A3) \quad \begin{bmatrix} x''' \\ y''' \\ z''' \end{bmatrix} = \begin{bmatrix} 1 & 0 & 0 \\ 0 & \cos \phi & \sin \phi \\ 0 & -\sin \phi & \cos \phi \end{bmatrix} \begin{bmatrix} x'' \\ y'' \\ z'' \end{bmatrix} = \mathbf{R}_\phi \begin{bmatrix} x'' \\ y'' \\ z'' \end{bmatrix}$$

Thus, vectors represented in the initial body-frame at time  $t = t_0$  are transformed into the body-frame at time  $t$  by the sequence of three rotations:

$$(A4) \quad \mathbf{v}^b = \mathbf{R}_\phi \mathbf{R}_\theta \mathbf{R}_\psi \mathbf{v}^{b_0} = \mathbf{R}_{b_0 \rightarrow b} \mathbf{v}^{b_0}$$

where

$$\mathbf{R}_{b_0 \rightarrow b} \equiv \mathbf{R}_\phi \mathbf{R}_\theta \mathbf{R}_\psi = \begin{bmatrix} \cos \psi \cos \theta & \sin \psi \cos \theta & -\sin \theta \\ -\sin \psi \cos \phi + \cos \psi \sin \theta \sin \phi & \cos \psi \cos \phi + \sin \psi \sin \theta \sin \phi & \cos \theta \sin \phi \\ \sin \psi \sin \phi + \cos \psi \sin \theta \cos \phi & -\cos \psi \sin \phi + \sin \psi \sin \theta \cos \phi & \cos \theta \cos \phi \end{bmatrix}$$

.

The inverse transformation is (recalling the fact that  $\mathbf{R}_{b_0 \rightarrow b}^{-1} \equiv \mathbf{R}_{b_0 \rightarrow b}^T$ , because  $\mathbf{R}_{b_0 \rightarrow b}$  is orthonormal)

$$(A5) \quad \mathbf{v}^{b_0} = \mathbf{R}_{b \rightarrow b_0} \mathbf{v}^b = \mathbf{R}_{b_0 \rightarrow b}^T \mathbf{v}^b$$

i.e.

$$\mathbf{R}_{b \rightarrow b_0} = \begin{bmatrix} \cos \psi \cos \theta & -\sin \psi \cos \phi + \cos \psi \sin \theta \sin \phi & \sin \psi \sin \phi + \cos \psi \sin \theta \cos \phi \\ \sin \psi \cos \theta & \cos \psi \cos \phi + \sin \psi \sin \theta \sin \phi & -\cos \psi \sin \phi + \sin \psi \sin \theta \cos \phi \\ -\sin \theta & \cos \theta \sin \phi & \cos \theta \cos \phi \end{bmatrix}$$